

Electrokinetic conversion

Electrokinetic conversion

PROEFSCHRIFT

ter verkrijging van de graad van doctor
aan de Technische Universiteit Delft,
op gezag van de Rector Magnificus prof.ir. K.C.A.M. Luyben,
voorzitter van het College voor Promoties,
in het openbaar te verdedigen op maandag 14 maart 2011 om 15:00 uur

door Ferdinand Christiaan SCHOEMAKER

Ingenieur luchtvaart en ruimtevaart
geboren te Amsterdam.

Dit proefschrift is goedgekeurd door de promotor:

Prof.dr.ir. D.M.J. Smeulders

Copromotor:

Dr.ir. E.C. Slob

Samenstelling promotiecommissie:

Rector Magnificus,	voorzitter
Prof.dr.ir. D.M.J. Smeulders,	Technische Universiteit Eindhoven, promotor
Dr.ir. E.C. Slob,	Technische Universiteit Delft, copromotor
Prof.dr.ir. C.P.A. Wapenaar,	Technische Universiteit Delft
Prof.dr. J. Bruining,	Technische Universiteit Delft
Prof.ir. C.P.J.W. van Kruijsdijk,	Shell International Exploration & Production
Prof.Dr.-Ing. H. Steeb,	Ruhr-Universität Bochum
Dr. R. Sprik,	Universiteit van Amsterdam

Printed by:

Proefschriftmaken.nl | Printyourthesis.com

ISBN: 978-90-8891-239-9

© 2011 by F.C. Schoemaker

All rights reserved. No part of the material protected by this copyright notice may be reproduced or utilized in any form or by any means, electronic or mechanical, including photocopying, recording or by any information storage and retrieval system, without written consent of the publisher.

Printed in The Netherlands

Summary

Electrokinetic conversion

Electrokinetic coupling is investigated theoretically and experimentally. Electrokinetic coupling describes the conversion from seismic and/or acoustic energy to electromagnetic energy, or vice versa. The origin of this effect lies in a very thin nanolayer which is conventionally present at all solid-fluid interfaces where an excess charge density with respect to the bulk charge density in the pore fluid exists. Any hydraulic disturbances of this nanolayer cause electric currents that are opposed by ionic counterflows generating electric fields. These effects become manifest when acoustic waves impinge upon the interface between two adjacent porous layers having different electro-mechanical properties, for example. An additional electromagnetic wave is generated which propagates omnidirectionally with the speed of light in matter, and can be recorded by simple wire electrodes. Here the word "additional" is understood with respect to the original two compressional and single shear waves that exist in porous media saturated with non-conductive fluids. The theoretical basis for the coupling phenomena under investigation is conceptually imbedded in the framework of the combined Biot-Maxwell equations. It is found that also the original Biot waves are affected by the electrokinetic coupling effect, but usually only up to a small extend.

An important aspect of the theory is the so-called dynamic (i.e., frequency-dependent) electrokinetic coupling factor $\hat{L}(\omega)$. For simple geometries such as parallel-plate channels and cylindrical capillaries, $\hat{L}(\omega)$ can be computed in the framework of the linearized Poisson-Boltzmann equation (LPBE). The validity of the linearization process was checked for narrow parallel-plate channels, where the full PBE can be solved analytically. It is shown that for realistic porous media, where the pore size is considerably larger than the Debye length, the LPBE can be applied indeed.

Experiments to measure both the absolute and phase values of $\hat{L}(\omega)$ are carried out in a so-called Dynamic Darcy Cell (DDC). Here, a low-frequency

(5-200 Hz) oscillatory flow is induced in a porous sample by means of an electromechanical shaker. The sample is carefully saturated with a conductive fluid. Both the pressure gradient and the voltage gradient are measured independently. The ratio of the both determines the electrokinetic coupling $\hat{L}(\omega)$. Good agreement between experiment and theory is obtained for capillary samples saturated with fluids containing different ionic species and different concentrations. Repeatability was ensured. Only the experiments with KCl and NaI deviated from theory, probably due to the fact that the empirical relation for the zeta-potential does not accurately describe differences of ionic species.

We note that all input parameters for the theoretical model were determined in independent laboratory experiments and that no fit factors were applied. Two methods for measuring the voltage gradient were tested. The first uses porous electrode platens sandwiching the sample under consideration. The second uses two simple wire electrodes that are installed in the liner of the DDC, thus causing minimum flow disturbances. We found that generally the latter method performs better, because the porous electrode platens may act as electric capacitors and thus compromise the measurements. Also more realistic samples consisting of sintered glass particles were investigated. Agreement between experiment and theory was found here as well.

Samenvatting

Elektrokinetische omzetting

We hebben theoretisch en experimenteel onderzoek verricht naar elektrokinetische omzetting. Het beschrijft de omzetting van seismische en/of akoestische energie naar elektromagnetische en vice versa. De oorzaak van dit effect is gelegen in een zeer dunne grenslaag (nanolaag) die gemeenzaam aanwezig is op het grensvlak van de korrels en de vloeistof in een poreus materiaal. In de vloeistofgrenslaag bestaat een ladingsoverschot ten opzichte van de ongestoorde ladingsdichtheid buiten de grenslaag. Een drukverstoring in de nanolaag veroorzaakt een elektrische stroom die tegengegaan wordt door conductief ionentransport in de andere richting. Hierbij worden elektrische velden gegenereerd. Deze effecten manifesteren zich met name wanneer akoestische golven invallen op een grensvlak tussen bijvoorbeeld twee aangrenzende poreuze lagen die verschillende akoestische of elektromechanische eigenschappen hebben. Er zal dan een elektromagnetische golf worden gegenereerd die zich in alle richtingen voortplant met de snelheid van het licht (in materie), en die te detecteren valt met behulp van een eenvoudige elektrode. Deze elektromagnetische golf bestaat naast de twee compressiegolven en de schuifgolf die ook in een vloeistofverzadigd poreus materiaal voorkomen. De theoretische basis voor het onderzocht koppelingsverschijnsel is gelegen in de gecombineerde Biot-Maxwell vergelijkingen. Wij hebben geconstateerd dat ook de oorspronkelijke Biot golven beïnvloed worden door het elektrokinetische koppelingseffect. Dit heeft echter een relatief zwak effect op de golfsnelheden en demping.

Een belangrijk aspect van de theorie is de zogenaamde dynamische (frequentieafhankelijke) elektrokinetische koppelings factor $\hat{L}(\omega)$. Voor eenvoudige spleet- en buisvormige configuraties, is het mogelijk om $\hat{L}(\omega)$ te berekenen in het kader van de gelineariseerde Poisson-Boltzmann vergelijkingen. De geldigheid van de gelineariseerde processen is gecontroleerd voor nauwe spleetvormige kanaaltjes, waarbij de volledige Poisson-Boltzmann vergelijkingen

analytisch opgelost kunnen worden. We tonen aan dat voor realistische poreuze media, waar de poriegrootte aanzienlijk groter is dan de Debye lengte, de Poisson-Boltzmann vergelijking gelineariseerd kan worden zonder de uitkomst te beïnvloeden.

Experimenten om zowel de absolute waarde als de fase van $\hat{L}(\omega)$ te meten zijn uitgevoerd met behulp van de Dynamische Darcy Cel (DDC). Daarin is in het lage frequentiegebied (5-200 Hz) een oscillerende stroming geïnduceerd in het poreuze monster door middel van een elektromechanisch trillingsapparaat. Het monster is zorgvuldig verzadigd met een geleidende vloeistof. Zowel de drukgradiënt als het spanningsverschil zijn onafhankelijk van elkaar gemeten. De verhouding van beide geeft de elektrokinetische koppelingscoëfficiënt $\hat{L}(\omega)$. De experimenteel gemeten resultaten zijn in overeenstemming met de theorie voor monsters bestaande uit kleine capillairtjes verzadigd met verschillende zouten bij verschillende concentraties. Wij constateren ook dat de experimenten goed reproduceerbaar zijn. Als de experimenten worden uitgevoerd met KCl of NaI zoutoplossingen, vinden wij afwijkingen van de theoretisch voorspelde waarden. Dit wordt waarschijnlijk veroorzaakt doordat de empirische relatie die voor de zeta-potentiaal wordt gebruikt in deze gevallen niet geheel correct is.

Alle invoerparameters voor het theoretische model zijn bepaald in onafhankelijke laboratoriummetingen en er is geen gebruik gemaakt van correctiefactoren. Twee methodes zijn getest. Bij de eerste methode gebruiken we poreuze plaatjes als elektrodes. Deze worden boven en onder het poreuze monster aangebracht. Bij de tweede methode gebruiken we draadvormige elektroden, die geïntegreerd zijn in de kunststof binnenmantel van de DDC, en zo slechts een minimale stromingsverstoring veroorzaken. In het algemeen kunnen we constateren dat de laatste methode een beter resultaat oplevert, omdat de poreuze plaalectrodes als elektrische condensator kunnen functioneren en daarmee de meting kunnen verstoren. Ook meer realistische monsters van gesinterde glasdeeltjes zijn onderzocht. Ook hier komen de gemeten waarden overeen met de bestaande theorie.

Contents

1	Introduction	1
1.1	Background	1
1.2	Literature survey	5
2	Electrokinetic flow phenomena	7
2.1	Theory of electrokinetic flow	10
2.1.1	Debye-Hückel approximation	11
2.2	Electrokinetic flow in a narrow parallel-plate channel	13
2.2.1	Charge and potential distribution	13
2.2.2	Electro-osmotic flow in a narrow parallel-plate channel	16
2.2.3	Streaming Potential in a narrow parallel-plate channel	19
2.3	The electroviscous effect	22
2.4	Electrokinetic flow in a cylindrical capillary	23
3	Dynamic coupling coefficients	27
3.1	Newtonian viscous-flow equations	27
3.1.1	Dynamic permeability	27
3.1.2	Dynamic permeability	33
3.1.3	Multi-layered media	35
3.1.4	Multi-layered media EK coupling	38
3.1.5	Principles of electro-osmosis	40
3.2	Sensitivity analysis	43
3.3	Onsager relationships	46
4	Electrokinetic wave propagation	49
4.1	Electrokinetic relations	50
4.2	Wave motion	53
4.2.1	Longitudinal waves	54
4.2.2	Transversal waves	57
4.2.3	Numerical results	60

4.3	Electrokinetic coupling effect	65
5	Experimental results	69
5.1	Dynamic Darcy Cell	69
5.2	Sample preparation and treatment	71
5.3	Dynamic pressure measurements	72
5.4	Dynamic coupling coefficient measurements	77
5.4.1	Concentration effects	79
5.4.2	Other electrolytes	79
5.5	Electrode disks	81
5.6	Sintered glass beads	81
6	Conclusions	89
	Bibliography	92
A	Biot-Gassmann constants	101
A.1	Continuum mechanics	101
A.1.1	Stress-strain relationships in porous media	102
B	Parameter determination	109
B.1	Basic mechanical parameters	109
B.1.1	Porosity	109
B.1.2	Permeability	109
B.1.3	Tortuosity	111
B.2	Conductivity determination	111
B.2.1	Dynamic conductivity coefficient	118
C	Elliptic integral solution	121
C.1	Elliptic integral of the first kind	121
C.2	Elliptic integral of the second kind	122

Abbreviations and symbols

Symbols

a	Effective ion radius	[m]
b_f	Forchheimer's coefficient	[m ⁻¹]
b_l	Fluid mobility	[s kg ⁻¹]
c_q	Solute, molar concentration	[mol l ⁻¹]
d	Debye length	[m]
$d_{1,2}$	Capillary radius	[m]
e	Direct volumetric strain	[-]
e_{ij}	Strain tensor of the solid	[-]
e_0	Elementary charge	[C]
f_c	Critical frequency	[Hz]
\mathcal{F}	Faraday's constant	[C mol ⁻¹]
$\hat{k}(\omega)$	Dynamic permeability	[m ²]
k_0	Permeability	[m ²]
k_B	Boltzmann number	[J K ⁻¹]
\mathbf{k}	Wavenumber vector	[m ⁻¹]
m	Shape factor	[-]
p	Pressure	[Pa]
pH	pH value	[-]
r	Radius	[m]
\mathbf{r}	Elliptic modulus	[-]
s	Complex-valued slowness	[s m ⁻¹]
t	Time	[s]
\mathbf{u}_f	Average fluid displacement vector	[m]
\mathbf{u}_s	Average solid displacement vector	[m]
$v(\omega)$	Phase velocity	[m s ⁻¹]
v_0	Laminar flow velocity	[m s ⁻¹]
v_e	Electro-osmotic velocity	[m s ⁻¹]
v_{max}	Maximum velocity Poiseuille flow	[m s ⁻¹]

\mathbf{v}_f	Average fluid velocity vector	$[\text{m s}^{-1}]$
\mathbf{v}_s	Average solid velocity vector	$[\text{m s}^{-1}]$
\bar{v}_x	Mean velocity in x direction	$[\text{m s}^{-1}]$
\mathbf{w}	Relative displacement vector	$[\text{m}]$
\mathbf{x}	Position vector	$[\text{m}]$
z_l	Valence of l -type ion	$[-]$
A	Surface area	$[\text{m}^2]$
A	Biot-Gassmann parameter	$[\text{Pa}]$
B_i	Parabolic velocity function variables	$[-]$
BSC	Borosilicate core	
C_{em}	Excess conductance	$[\text{C}^2 \text{ s m}^{-2} \text{ kg}^{-1}]$
C_{os}	Conductance	$[\text{C}^2 \text{ s m}^{-2} \text{ kg}^{-1}]$
C_q	Burgreen Nakache parameter	$[-]$
D	Diffusion coefficient	$[\text{m}^2 \text{ s}^{-1}]$
D_h	Biot diffusion coefficient	$[\text{m}^2 \text{ s}^{-1}]$
E	Elliptic integral of the second kind	$[-]$
$\hat{\mathbf{E}}$	Electric field vector	$[\text{Vm}^{-1}]$
$\hat{F}(\omega)$	Viscous correction factor	$[-]$
F	Elliptic integral of the first kind	$[-]$
F_i	Force vector	$[\text{N}]$
G	Shear modulus	$[\text{Pa}]$
GC	Sintered glass core	
G_0	Dry weight	$[\text{N}]$
G_1	Fully saturated weight	$[\text{N}]$
G_q	Ratio of the mean potential	$[-]$
$\hat{\mathbf{H}}$	Magnetic field vector	$[\text{A m}^{-1}]$
H	Gassmann modulus	$[\text{Pa}]$
H	Half channel width	$[\text{m}]$
H_q	Reduced Burgreen parameter	$[-]$
H_{qr}	Compact Burgreen parameter	$[-]$
\tilde{H}	Reduced half channel width	$[-]$
I_0	Zero-order modified Bessel function	$[-]$
\hat{I}_{conv}	Convection current	$[\text{A}]$
I_x	Electric current in x direction	$[\text{A}]$
J_0	Bessel functions of the first kind, order zero	$[-]$
J_1	Bessel functions of the first kind, order one	$[-]$
J_c	Chemical diffusive flux	$[\text{mol m}^{-2} \text{ s}]$
\mathbf{J}	Electric current density vector	$[\text{Am}^{-2}]$
K_f	Fluid bulk modulus	$[\text{Pa}]$
K_{fr}	Frame bulk modulus	$[\text{Pa}]$

K_s	Bulk modulus solid	[Pa]
$\hat{L}(\omega)$	Dynamic electrokinetic coupling factor	[m ² s ⁻¹ V ⁻¹]
MC	Monel disks without sample	
M_q	Nakache parameter	[-]
MSC	Borosilicate core with Monel disks	
N_a	Number of Avogadro	[mol ⁻¹]
N_l	Ionic concentration of l -type ion	[m ⁻³]
N_l^∞	Ionic concentration in bulk solution	[m ⁻³]
P	Biot-Gassmann parameter	[Pa]
P_0	Dimensionless parameter	[-]
Q	Biot-Gassmann parameter	[Pa]
$Q^{-1}(\omega)$	Specific attenuation	[s ⁻¹]
QC	Quartz core	
Q_0	Average flow rate	[m ³ s ⁻¹]
Q_x	Volume flux	[m ³ s ⁻¹]
Q_T	Heat flux	[W m ⁻²]
R	Biot-Gassmann parameter	[Pa]
R_c	Radius capillary	[m]
\mathcal{R}	Universal gas constant	[JK ⁻¹ mol ⁻¹]
T	Temperature	[K]
V_B	Bulk volume	[m ³]
V_s	Volume contained by grains	[m ³]
V_{HS}	Helmholtz-Smoluchowski velocity	[m s ⁻¹]
$\hat{W}(\omega)$	Average flow velocity	[m s ⁻¹]

Greek symbols

α_∞	Tortuosity	[-]
$\alpha_Q(\omega)$	Attenuation coefficient	[m ⁻¹]
α_w	Womersley parameter	[-]
χ	Formation factor	[-]
δ_{ij}	Kronecker symbol	[-]
ϵ_{ij}	Strain tensor of the fluid	[-]
η	Viscosity	[Pa s]
η_a	Apparent viscosity	[Pa s]
γ	Area ratio within DDC	[-]
κ	Screening parameter	[m ⁻¹]
λ	Roots of Bessel function	[-]

μ	Magnetic permeability	[H m ⁻¹]
μ_0	Magnetic permeability in vacuum	[H m ⁻¹]
μ_c	chemical potential	[kg m ⁻⁴ s ⁻¹]
μ_r	Relative magnetic permeability	[—]
ν	Kinematic viscosity	[m ² s ⁻¹]
ω	Frequency	[rad s ⁻¹]
ω_c	Critical frequency	[rad s ⁻¹]
ω_{EM}	E-M critical frequency	[rad s ⁻¹]
ϕ	Porosity	[—]
ρ_{ij}	Density functions	[kg m ⁻³]
$\hat{\rho}^E(\omega)$	Effective electrokinetic density	[kg m ⁻³]
$\hat{\rho}_{ij}^E(\omega)$	Effective electroviscous density	[kg m ⁻³]
$\hat{\rho}_{ij}(\omega)$	Generalized effective density functions	[kg m ⁻³]
ρ	Total density of solid and fluid	[kg m ⁻³]
ρ_1	Density of solid in porous medium	[kg m ⁻³]
ρ_2	Density of fluid in porous medium	[kg m ⁻³]
ρ_c	Net charge density	[C m ⁻³]
ρ_E	Excess charge density	[C m ⁻³]
ρ_f	Density of fluid	[kg m ⁻³]
ρ_s	Density of solid	[kg m ⁻³]
ρ_t	Density parameter	[kg m ⁻³]
σ	Conductivity	[S m ⁻¹]
$\hat{\sigma}(\omega)$	Dynamic conductivity	[S m ⁻¹]
σ_0	Total fluid electric conductivity	[S m ⁻¹]
σ_f	Intrinsic fluid conductivity	[S m ⁻¹]
$\sigma_{f298.15}$	Intrinsic fluid conductivity at 298.15 K	[S m ⁻¹]
σ_{ij}	Intergranular stress tensor	[Pa]
σ_s	Conductivity of fluid-filled porous insulator	[S m ⁻¹]
ε	Permittivity of medium	[F m ⁻¹]
ε_0	Permittivity of vacuum	[F m ⁻¹]
ε_r	Relative permittivity	[—]
ε_{rf}	Permittivity of fluid	[—]
ε_{rs}	Permittivity of solid	[—]
$\hat{\varepsilon}(\omega)$	Effective permittivity	[F m ⁻¹]
ϖ	Complex viscous skin depth	[m]
\mathfrak{S}_E	Rotational vector potential, electric field	[V]
$\mathfrak{S}_{f,s}$	Rotational vector potential, fluid or solid	[m ²]
\wp_E	Longitudinal potential, electric field	[V]
$\wp_{f,s}$	Longitudinal potential, fluid or solid	[m ²]
τ_{ij}	Total stress tensor in bulk material	[Pa]

τ_w	wall shear stress	[Pa]
θ	Amplitude of elliptic integral	[–]
θ_s	Amplitude of the Jacobian function	[–]
ξ	Hydrostatic pressure	[Pa]
ζ	Zeta potential	[V]
Γ	Amplitude ratio	[–]
Λ	Weighted volume-to-pore surface ratio	[m]
Φ	Electric potential	[V]
Φ_B	Boltzmann potential	[V]
Φ_s	Wall potential	[V]
Φ_d	Stern potential	[V]

Common physical constants

Table 1: Elementary constants.

Name	Symbol	Value	Unit
Avogadro number	N_a	$6.022 \cdot 10^{23}$	mol^{-1}
Boltzmann constant	k_B	$1.381 \cdot 10^{-23}$	J K^{-1}
Elementary charge	e	$1.602 \cdot 10^{-19}$	C
Faraday constant	\mathcal{F}	$9.649 \cdot 10^4$	C mol^{-1}
Magnetic permeability (vacuum)	μ_0	$1.257 \cdot 10^{-6}$	H m^{-1}
Permittivity (vacuum)	ϵ_0	$8.854 \cdot 10^{-12}$	F m^{-1}
Speed of light (vacuum)	\bar{c}	$2.998 \cdot 10^8$	m s^{-1}
Universal gas constant	\mathcal{R}	8.314	$\text{J K}^{-1} \text{mol}^{-1}$

Table 2: Basic parameters (at room temperature $T = 25^\circ\text{C}$).

Name	Symbol	Value	Unit
Density of air	ρ_a	1.184	kg m^{-3}
Speed of sound in air	c_a	346	m s^{-1}
Viscosity of air	η_a	$1.81 \cdot 10^{-5}$	Pa s
Density of water	ρ_f	$0.997 \cdot 10^3$	kg m^{-3}
Speed of sound in water	c_f	1500	m s^{-1}
Viscosity of water	η	$0.891 \cdot 10^{-3}$	Pa s
Water bulk modulus	K_f	$2.2 \cdot 10^9$	Pa
Standard atmospheric pressure	p_0	$1.01325 \cdot 10^5$	Pa

Chapter 1

Introduction

1.1 Background

In their search for new exploration tools, geophysicists have studied the coupling between seismic and electromagnetic waves in the shallow subsurface of the earth since the 1930s. Electro seismic (ES) surveying and its reciprocal process, seismic-to-electromagnetic conversion (SE), are methods for remotely identifying the presence of hydrocarbons in the subsurface of the earth using the conversion of electromagnetic energy to seismic energy, or vice versa. A controlled waveform voltage is typically applied to electrodes at the earth's surface, causing large currents to flow in the subsurface (see Figure 1.1).

In the pores, where the saturating electrolyte fluid is in contact with the grains, a positively charged nano-layer at the solid-liquid interface usually exists. This is because the silane terminals SiOH , located at the grain surface become protonated in the presence of an aqueous solution (electrolyte). The corresponding (negative) grain surface potential is called the zeta potential, which is typically on the order of a few tens of millivolts. The counter ions in the fluid reorganize in a layer that is bound to the surface by electrostatic forces (Stern layer), and a diffuse layer that is free to flow. In the diffuse layer the competition between electrostatic forces and thermal diffusivity excites an exponentially decreasing voltage amplitude if one moves away from the interface towards the bulk of the pore. The corresponding length scale is called the Debye length, which is on the order of a few tens of nanometers, for typical reservoir rocks. The Stern layer and the diffuse layer together are usually called the electric double layer (EDL). The EDL nano-layer is thus considerably thinner than any viscous or thermal boundary layers that normally exist in pore fluid transport phenomena. Owing to the electric field

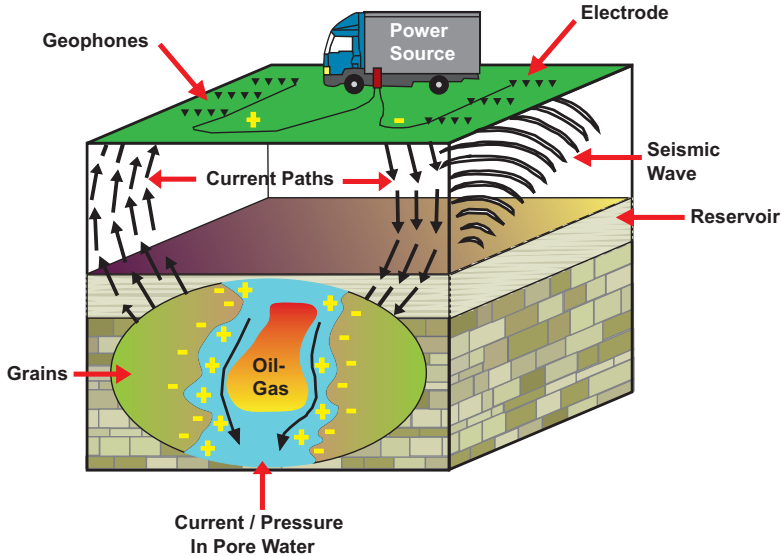


Figure 1.1: Schematic of electroseismic field experiment [Thompson et al. (2006, 2007)].

exerted at the EDL, the counter ions are set in motion, which is purely an electro-osmotic effect, with fluid viscosity and electrical permittivity as the medium parameters involved. When the thin boundary layer speeds up, it drags along the bulk of the fluid by means of viscous shear. As a result, a plug-like velocity profile is induced in the pores, for quasi-stationary behaviour. For higher frequencies, inertia terms have to be taken into account, resulting in more complex velocity distributions.

At certain discontinuities in rock or fluid properties, it is also possible that a portion of the electric current converts into seismic energy. This is called electrokinetic coupling. At a contrast in electrical properties, the vertical component of the electrical field is discontinuous. The resulting field gradient creates a local displacement of the EDL, local relative fluid flow with respect to the grains, and local pressure gradients in the rock, acting as a source for reflected seismic waves. Geophones record the resulting seismic wave at the surface or in boreholes (see Figure 1.1). The largest ES signals are expected when high resistance layers (hydrocarbon layers) create large discontinuities in the vertical component of the electric field with respect to conductive water bearing layers. The ES method could thus be an effective tool for OWC (Oil Water Contact) detection. This is confirmed by field tests of electroseismic hydrocarbon detection [Thompson et al. (2007)]. It was

found that large amplitude conversions between seismic and electromagnetic energies are favoured by (i) contrasts in acoustic impedances, (ii) permeable pore space, and (iii) high-resistivity pore fluids.

All field data, however, consist of simultaneous contributions from the electrokinetic coupling converting part of the electrical energy into seismic (kinetic) energy, and compressibility effects that define the seismic wave conveying its energy back to the geophones. If one wants to study the electrokinetic coupling by itself, it is probably a better idea to decouple electrokinetic conversion from the seismic conveying process by constructing a dedicated experimental setup in which the wavelength is much larger than the sample size so that the fluid can effectively be regarded incompressible. This is exactly what we did in our Dynamic Darcy Cell (DDC), which allowed us to independently measure electrokinetic coupling as a function of frequency, fluid salinity, and ionic species.

A theoretical framework for electrokinetic coupling phenomena is provided by the so-called Poisson-Boltzmann equation (PBE), relating the electric potential to the charge density. The charge density (ionic concentration) is defined by the Boltzmann distribution. The PBE is a non-linear second-order differential equation that can only be solved analytically for some special cases. For more general solutions, the PBE is usually linearized. This is treated in **Chapter 2**, where the linearization terms and conditions are discussed for stationary flow.

In **Chapter 3**, the theory is extended to oscillatory flow fields, where inertia terms have to be taken into account. Electrokinetic coupling and its complementary process, seismo-electric coupling should obey Onsager's principle of reciprocity. This is investigated as well.

In the motivation for this study we treated electromagnetic waves converting part of their energy into seismic waves. Vice versa, incident seismic waves impinging upon an interface with discontinuities in electro-acoustic properties, may generate electromagnetic waves that can propagate outside the support of the seismic wave. Also co-seismic electric fields generally exist, that propagate with the speed of the seismic wave. A schematic description of seismo-electric effects is shown in Figure 1.2. The panels (a)-(c) show a cross-section of the underground as time proceeds. The corresponding seismoelectrogram is shown in panel (d) (time traces versus offset). The underground consists of layers 1 and 2. An electrode is positioned at the surface. In panel (a) a local pressure source is initiated at $t = 0$. This could be an explosive charge for example. The local charge separation caused by the pressure source will have a strong dipole component and the associated electrical field is called the **Direct Field** [Kroeger (2007)]. This disturbance is measured almost

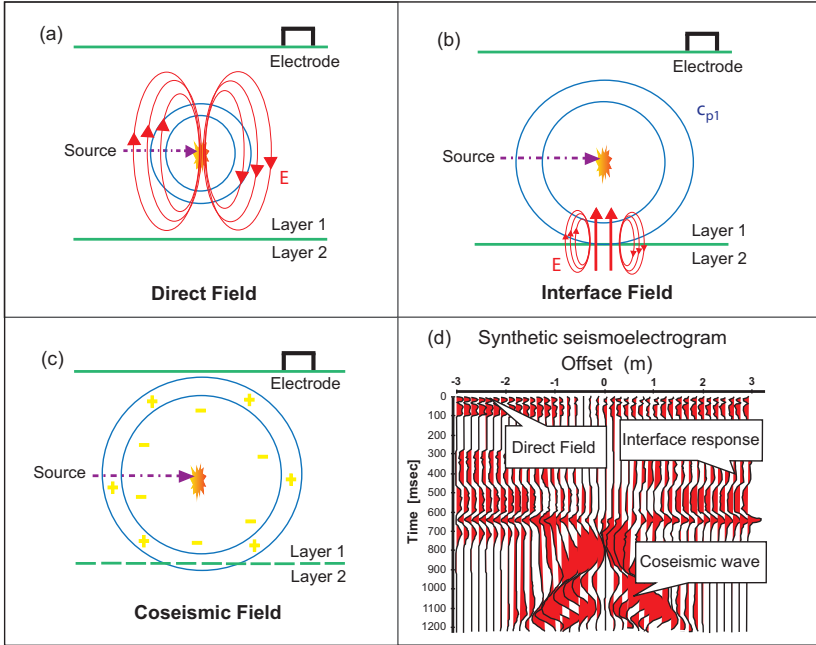


Figure 1.2: Schematic of a 'standard' geometry for a seismoelectric survey [Haines (2004), Kroeger (2007)].

immediately by the electrode, see Figure 1.2d.

The explosion also sends forth pressure waves that will encounter the interface between layers 1 and 2, resulting in a local asymmetry in the charge distribution. This will induce an oscillating electric dipole. The associated electro-magnetic field will travel almost immediately to the receiver, see Figure 1.2d. This seismoelectric effect is known as the **Interface Field**.

Finally, the seismic wave will reach at the upper surface. The seismic wave creates a fluid pressure gradient that induces pore fluid flow. Due to pore fluid movement within the electric double layer a small amount of electric charge relative to the fixed charge (on the pore wall) is transported. The net flow of charge relative to the grains is the so-called streaming electric current. The associated electric field is known as the **Coseismic Field** [Haines (2004)]. The coseismic field travels along with the seismic wave, giving it the typical parabolic shape (see Figure 1.2d).

As the electrokinetic waves eat away part of the acoustic energy, one may investigate the electrokinetic coupling effect on the phase speeds and attenuation coefficients of the conventional Biot-type waves. This is the subject of **Chapter 4**.

In **Chapter 5**, the Dynamic Darcy Cell is discussed in which the electrokinetic coupling effect is measured in the frequency range 1-100 Hz. It is designed to measure pressure gradients and voltage gradients over electrolyte-saturated test samples. The sample dimensions are chosen such that the wavelength is much larger than any sample size so that the saturating fluid is effectively incompressible. From the pressure measurements the dynamic permeability can be determined, and from the combined pressure and voltage measurements, the electrokinetic coupling coefficient is deduced.

1.2 Literature survey

The first observation of electrokinetics dates back to the beginning of the 19th century. In 1809, Reuss was the first to report an experiment where a direct current was applied to a clay-sand-water mixture. The experiment was performed with a U-tube, filled with quartz at the bottom. Application of an electric current caused the water to rise in the one leg containing the negative electrode. The water was pumped upwards against gravity, without any moving mechanical components [Sunderland (1987)].

Quincke (1859) observed electro-osmosis through glass capillaries. Their simple geometry allowed well-controlled experimental conditions. Linearity between the electro-osmotic volume or the created osmotic counter pressure and the applied electric field was confirmed. Reuss (1809) and Quincke (1859) also described electrophoretic mobility, where particles are mobilized with electrical fields. A mathematical description of electro-osmotic and electrophoretic mobility was derived by Helmholtz (1879). He did not consider the dielectric permittivity. Smoluchowski, M. von (1903) derived the Helmholtz-Smoluchowski equation where permittivity is induced. Smoluchowski also recognized reciprocity between electro-osmotic flow and streaming potential as was later detailed by Onsager [Lyklema (2003)]. In later years Gouy (1910) and Chapman (1913) derived a theory for the screening of surface charge by the diffuse layer of counter-ions, relating the thickness of the diffuse layer to the ionic strength of the solution [Masliyeh and Bhattacharjee (2006)]. Stern (1924) derived an even more detailed model of the EDL. Another analysis, which describes the force between charged surfaces interacting through a liquid medium was derived some years later by Derjaguin and Landau (1941), and Verwey and Overbeek (1948) in the so-called 'DLVO' theory.

In 1936, Thompson suggested that electrical techniques could be used for geophysical prospecting of seismic waves, making use of the coupling effect that was patented by Blau and Statham (1936). The Russian physicist Yacov Il'ich Frenkel (1944) developed a theory for wave propagation in saturated

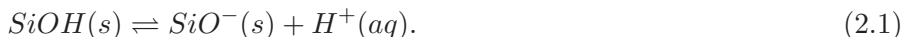
porous media, in which he predicted the slow compressional wave and the seismoelectric effect. In 1959, Martner and Sparks were the first to report that an electric potential difference generated in the subsurface by the passage of seismic waves, could be detected by electrode pairs. Somewhat later, an experimental programme was undertaken to evaluate the electroseismic effect as a possible means for detecting underground nuclear tests. The goal was to develop long range systems for detection of nuclear blasts, see e.g. Broding et al. (1963) and Long and Rivers (1975). Due to insensitive technical equipment, lack of computing power and the success of conventional seismic and electromagnetic methods, electrokinetics never gained much attention in geophysical exploration. Moreover, the majority of field tests up to the 1990s were concerned with the seismoelectric effect while the reciprocal electroseismic effect was underexposed. Extended field tests were only performed recently [Thompson et al. (2006)].

With respect to wave modeling, Neev and Yeats (1989) postulated a set of equations, which attempted to model the interaction between mechanical waves and electric fields due to electrokinetics. Their model did not include the Maxwell equations and frequency-dependence of the transport laws, which resulted in erroneous conclusions. A possible way to include all effects is by volume averaging the continuum equations for solid grains and electrolyte fluids. Using this approach Pride (1994) obtained the governing equations for coupled electromagnetics and acoustics of porous media. Although the individual constituents of Pride's model (i.e., Biot's theory and Maxwell's theory) have been validated experimentally, the coupling between the constituents has not yet been thoroughly validated experimentally. Parkard (1953) and, more recently, Reppert (2000) report experimental results but the influence of salt concentrations and ionic species was not investigated. Moreover, they performed single capillary experiments, whereas in our setup multiple capillaries are parallelized thus increasing the signal-to-noise ratio.

Chapter 2

Electrokinetic flow phenomena

When two phases are in contact with each other, they will generally develop a difference in electric potential. If one of the phases is a solid, which is in contact with an aqueous solution, the solid will develop an excess charge (co-ions), while the aqueous solution will develop a charge distribution of opposite sign (counter-ions). For a solid containing silanol ($SiOH$) groups, for example, a chemical reaction at the surface takes place



This is a so-called deprotonation of silanol groups [Maineult et al. (2004)]. The solid surface will become negatively charged and an excess opposite charge will occur in the fluid. In the fluid, the excess charge will redistribute into two distinct layers constituting the so-called *electric double layer* (EDL) [Chun et al. (2005), Hunter (1981), Tardu (2004)]. The first is the so-called Stern layer consisting of charge that is bound to the surface. The second consists of ions that are free to move. In this layer the ion distribution is governed by opposite forces. Molecular diffusion mitigates non-uniformities in charge distribution, whereas static electric forces favour charge separation. As a result, a diffuse layer will be formed in which the electric potential exponentially decreases if one moves away from the interface. In the bulk, electroneutrality is reached (see Figure 2.1). Far away from the solid surface the sum of all charges will be zero and Brownian motion will create a homogeneous spatial distribution of the ions.

Several EDL models exist in literature. The first model was proposed by Helmholtz, who introduced a bound layer of atomic dimensions, forming a molecular capacitor. Such a model however does not include thermal diffusivity and a linear potential decrease is predicted in the bound layer. The Gouy-Chapman model does include the effects working on ions due to ran-

dom thermal Brownian motion. The Gouy-Chapman model however, does not include a bound layer and assumes that the finite ionic diameter can be neglected. It also does not include the non-ideality of the solution and assumes the dielectric permittivity of the medium to be constant. By combining the Gouy-Chapman model with the Helmholtz model, the Stern model is obtained [Masliyah and Bhattacharjee (2006)]. It assumes that the bounded ions in the Stern layer can be distinguished into specifically adsorbed ions in the so-called inner Helmholtz layer and electro-statically bound ions in the so-called outer Helmholtz layer (see Figure 2.1). Specific adsorption refers to all interactions other than purely Coulombic, such as Van der Waals or hydrophobic binding, electron exchange and complex formation. The inner Helmholtz (IH) plane passes through the electric centers of specifically adsorbed ions.

The outer Helmholtz plane passes through the electric centers of non-

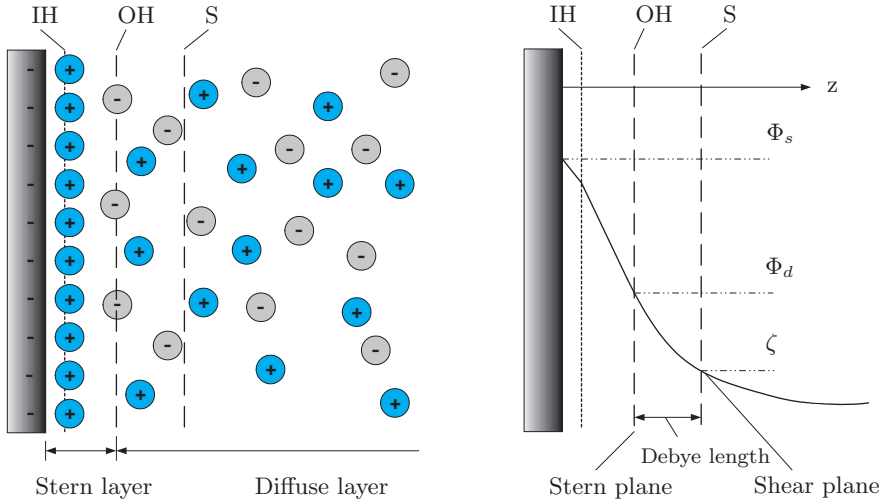


Figure 2.1: Electric double layer according to the Stern model. The inner and outer Helmholtz planes are indicated IH and OH, respectively. The slipping plane is denoted S and has potential ζ . The wall potential is Φ_s and the Stern potential is Φ_d . The z -axis is pointing away from the dielectric, and has its origin at the wall.

specifically adsorbed ions. The Stern plane is defined as the location of the outer Helmholtz plane. The corresponding potential is Φ_d . In the diffuse layer, a slipping (shear) plane S is usually defined where electrostatic forces and molecular diffusion are on the same order of magnitude. This slipping plane is defined by its potential ζ and Debye length d . The Debye length is the scale over which mobile charge carriers (e.g. electrons) screen out electric

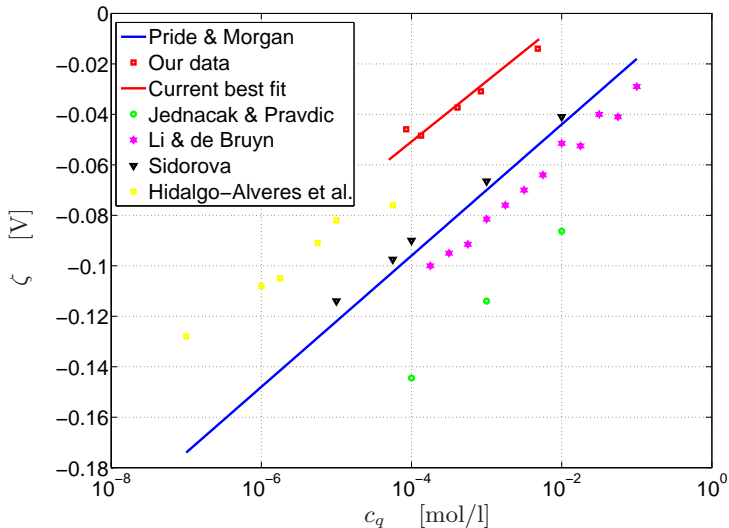


Figure 2.2: Zeta potentials for different concentrations at $\text{pH}=7$ and $T=25^\circ\text{C}$.

fields in electrolytes, colloids and plasmas. It is the distance over which significant charge separation can occur and is a measure of the electric double layer thickness (typically it is on the order of a few tens of nanometers) [Masliyah and Bhattacharjee (2006), Rice and Whitehead (1965)]. Beyond the diffuse layer, the liquid bulk is defined. Because this thesis deals with fluid motion and the Stern layer is in the range of atomic dimensions, we will use the Gouy-Chapman approach. We will identify ζ as the wall potential, which is obtained from experimental data or empirical relationships [Masliyah and Bhattacharjee (2006)]. A commonly used empirical relationship for the zeta potential as function of the solute, molar concentration c_q and pH value has the following form [Pride and Morgan (1991)]:

$$\zeta = (8 \cdot 10^{-3} + 3 \cdot 10^{-2} \log c_q) \frac{\text{pH} - 2}{5}, \quad (2.2)$$

but other relationships are also found [see e.g. Johnson (1998)]. From our data we obtain:

$$\zeta = (4 \cdot 10^{-2} + 2 \cdot 10^{-2} \log c_q) \frac{\text{pH} - 2}{5}. \quad (2.3)$$

Figure 2.2 shows the zeta potential versus concentration at $\text{pH}=7$ and $T=25^\circ\text{C}$. Our data for NaCl are obtained from the measurements as described in section 5.4.1.

2.1 Theory of electrokinetic flow

In a homogeneous medium of permittivity ε , the electric potential Φ is related to the charge density ρ_E by the Poisson equation

$$-\varepsilon \nabla^2 \Phi = \rho_E. \quad (2.4)$$

The charge density of an electrolyte containing L ion types can be written as

$$\rho_E = e_0 \sum_{l=1}^L \mathbf{z}_l N_l, \quad (2.5)$$

where N_l is the ionic concentration and \mathbf{z}_l the valence of the l -type ion and e_0 the elementary charge. Combination of (2.4) and (2.5) gives

$$\varepsilon \nabla^2 \Phi = -e_0 \sum_{l=1}^L \mathbf{z}_l N_l. \quad (2.6)$$

We now assume that the ionic concentration of the l -type ion is given by the Boltzmann distribution. Boltzmann's distribution is based on the hypothesis that the fraction of molecules within an electrolyte in a particular state, at thermal equilibrium, exponentially depends on the energy of that state

$$N_l = N_l^\infty e^{-\frac{e_0 \mathbf{z}_l \Phi}{k_B T}}, \quad (2.7)$$

where N_l^∞ is the ionic concentration of the type l -ions in the bulk where $\Phi = 0$, k_B the Boltzmann number and T the absolute temperature. Far away from the surface there will be electroneutrality

$$\sum_{l=1}^L \mathbf{z}_l N_l^\infty = 0. \quad (2.8)$$

Substituting (2.7) into (2.6), leads to the Poisson-Boltzmann equation (PBE)

$$\varepsilon \nabla^2 \Phi = -e_0 \sum_{l=1}^L \mathbf{z}_l N_l^\infty e^{-\frac{e_0 \mathbf{z}_l \Phi}{k_B T}}. \quad (2.9)$$

In case of a bi-ionic monovalent electrolyte, the PBE becomes

$$\varepsilon \nabla^2 \Phi = 2N^\infty e_0 \sinh\left(\frac{e_0 \Phi}{k_B T}\right), \quad (2.10)$$

where $N_1^\infty = N_2^\infty = N^\infty$. Such a bi-ionic monovalent symmetric electrolyte has the property that $\mathbf{z}_1 = -\mathbf{z}_2 = 1$. We now introduce the reduced potential $\tilde{\Phi} = \Phi/\Phi_B$, where the Boltzmann potential Φ_B is given by

$$\Phi_B = \frac{k_B T}{e_0}. \quad (2.11)$$

The Boltzmann potential value typically is 25.3 mV at 20°C. Using Faraday's constant $\mathcal{F} = e_0 N_a$ and the universal gas constant $\mathcal{R} = k_B N_a$, the Boltzmann potential is often expressed as $\mathcal{R}T/\mathcal{F}$ [Oddy (2005)]. From (2.10) we find that

$$\nabla^2 \tilde{\Phi} = \kappa^2 \sinh(\tilde{\Phi}), \quad (2.12)$$

with

$$\kappa = \sqrt{\left(\frac{2e_0 N^\infty}{\varepsilon_0 \varepsilon_{rf} \Phi_B} \right)}, \quad (2.13)$$

the screening parameter (inverse Debye length). Using $N^\infty = c_q N_a \cdot 10^3$ we find that [Pride (1994)]

$$d = \frac{3.04 \cdot 10^{-10}}{\sqrt{c_q}}, \quad (2.14)$$

where N_a is the Avogadro Number ($6.022 \cdot 10^{23} \text{ mol}^{-1}$), e_0 the elementary charge ($1.602 \cdot 10^{-19} \text{ C}$), and $\varepsilon = \varepsilon_0 \varepsilon_{rf}$, where we have used that $\varepsilon_0 = 8.85 \cdot 10^{-12} \text{ F/m}$ (the electric permittivity in vacuum) and $\varepsilon_{rf} = 80$ as the relative permittivity of the fluid (see abbreviations and symbols). For salinity values of $1 \cdot 10^{-4} \text{ mol/l}$ the Debye length is on the order of $3 \cdot 10^{-8} \text{ m}$, which is generally less than any characteristic length in porous media.

2.1.1 Debye-Hückel approximation

We will now consider the one-dimensional situation where a single dielectric is immersed in an electrolyte, see Figure 2.1. The z -axis points away from the surface. A surface charge ζ will be assumed to exist at the surface. In this case the PBE becomes

$$\frac{\partial^2 \tilde{\Phi}}{\partial z^2} = \kappa^2 \sinh(\tilde{\Phi}). \quad (2.15)$$

The boundary conditions are

$$\tilde{\Phi}(z = 0) = \frac{\zeta}{\Phi_B} = \tilde{\Phi}_s, \quad (2.16)$$

$$\tilde{\Phi}(z \rightarrow \infty) = 0. \quad (2.17)$$

The solution to (2.15) was discussed by Masliyah and Bhattacharjee (2006):

$$\tilde{\Phi} = 2 \ln \left(\frac{1 + e^{-\kappa z} \tanh \frac{\tilde{\Phi}_s}{4}}{1 - e^{-\kappa z} \tanh \frac{\tilde{\Phi}_s}{4}} \right). \quad (2.18)$$

For small values of $\tilde{\Phi}$, the PBE (2.15) may be linearized to become

$$\frac{d^2 \tilde{\Phi}}{dz^2} = \kappa^2 \tilde{\Phi}. \quad (2.19)$$

Application of the boundary conditions (2.16) and (2.17) now yields that

$$\tilde{\Phi} = \tilde{\Phi}_s e^{-\kappa z}. \quad (2.20)$$

This is the so-called Debye-Hückel result for a single dielectric.

Another way to derive the linearized PBE (2.19) is as follows. The electric current density J_z perpendicular to the surface is determined by the combined effect of charge diffusion, convection, and electric fields

$$J_z = -D \frac{\partial \rho_E}{\partial z} + \rho_E v_z + \sigma E_z, \quad (2.21)$$

where D is the diffusion coefficient, v_z the fluid velocity, σ the conductivity, and E_z is an electric field perpendicular to the surface. For an isolated surface without normal velocity components, we have that

$$0 = -D \frac{\partial \rho_E}{\partial z} + \sigma E_z, \quad (2.22)$$

Introducing the electric potential Φ through $E_z = -\partial\Phi/\partial z$ we also have that

$$0 = -D \frac{\partial \rho_E}{\partial z} - \sigma \frac{\partial \Phi}{\partial z}, \quad (2.23)$$

which becomes after integration

$$\rho_E = -\frac{\sigma}{D} \Phi, \quad (2.24)$$

where the integration constant is zero (without charge density, $\Phi = 0$). Substitution of (2.24) in the Poisson equation (2.4) yields that

$$\varepsilon \frac{\partial^2 \Phi}{\partial z^2} = \frac{\sigma}{D} \Phi. \quad (2.25)$$

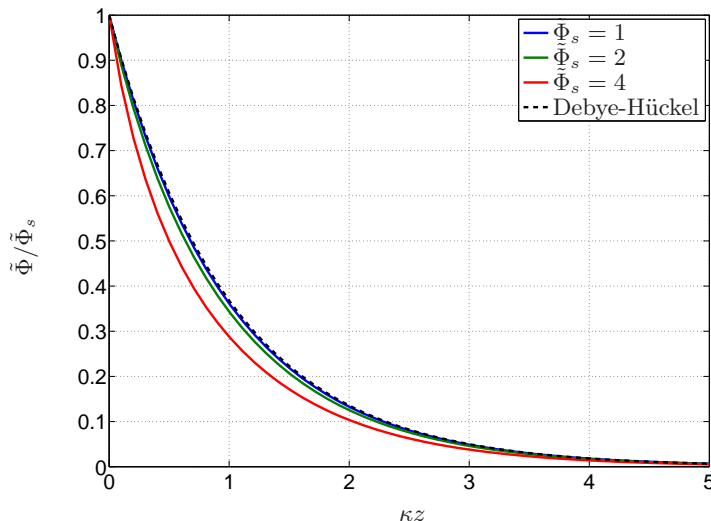


Figure 2.3: Potential distribution near a flat surface according to the Gouy-Chapman model for different values of the ζ potential. Also the Debye-Hückel approximation (dashed line) is plotted.

Identifying D as [Masliyah and Bhattacharjee (2006)]

$$D = \frac{\Phi_B \sigma}{(2N_l^\infty e_0)}, \quad (2.26)$$

and using $\kappa^2 = \sigma/(D\varepsilon)$ we find back (2.19).

In Figure 2.3 we investigate the difference between the linear solution (2.20) and the exact solution (2.18). We note that for higher values of the ζ potential, the exact Gouy-Chapman model is predicted less accurately by the Debye-Hückel approximation.

2.2 Electrokinetic flow in a narrow parallel-plate channel

2.2.1 Charge and potential distribution

We will now consider a narrow-parallel plate channel with channel width $2H$ (see Figure 2.4). Introducing the reduced distance $\tilde{z} = \kappa z$ from the center of the slit, the PBE (2.15) becomes

$$\frac{\partial^2 \tilde{\Phi}}{\partial \tilde{z}^2} = \sinh(\tilde{\Phi}). \quad (2.27)$$

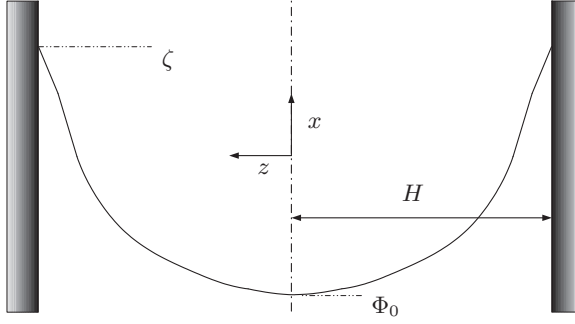


Figure 2.4: Electric potential distribution in a narrow parallel-plate channel with width $2H$. Note that $z = 0$ is now at the center of the channel.

To find the solution to (2.27) we proceed as follows. We seek for a function $f(\tilde{\Phi}) = d\tilde{\Phi}/d\tilde{z}$ satisfying (2.27). So we find that

$$\frac{df(\tilde{\Phi})}{d\tilde{z}} = \sinh(\tilde{\Phi}), \quad (2.28)$$

which can be rewritten as

$$f(\tilde{\Phi}) \frac{df(\tilde{\Phi})}{d\tilde{\Phi}} = \sinh(\tilde{\Phi}). \quad (2.29)$$

The boundary conditions are given by

$$f(\tilde{\Phi}(\tilde{z} = 0)) = 0, \quad (2.30)$$

$$\tilde{\Phi}(\tilde{z} = 0) = \tilde{\Phi}_0, \quad (2.31)$$

where we introduce $\tilde{\Phi}_0$ as the reduced potential in the center of the slit. Straightforward integration yields that

$$f = \frac{d\tilde{\Phi}}{d\tilde{z}} = \sqrt{2 \cosh(\tilde{\Phi}) - 2 \cosh(\tilde{\Phi}_0)}. \quad (2.32)$$

Choosing new variables \mathbf{r} and θ as

$$\mathbf{r} = e^{-\tilde{\Phi}_0}, \quad (2.33)$$

$$\sin \theta = \mathbf{r}^{-\frac{1}{2}} e^{-\frac{1}{2}\tilde{\Phi}} = e^{-\frac{1}{2}(\tilde{\Phi} - \tilde{\Phi}_0)}, \quad (2.34)$$

we show in the appendix C that the solution to (2.32) is given by

$$\tilde{z} = 2\sqrt{\mathbf{r}} \left(F\left(\frac{1}{2}\pi, \mathbf{r}\right) - F(\theta, \mathbf{r}) \right), \quad (2.35)$$

where $F(\theta, \mathbf{r})$ is the incomplete elliptic integral of the first kind, and $F(\frac{1}{2}\pi, \mathbf{r})$ is the corresponding complete integral. This solution was found by Langmuir (1938) and also discussed by Levine et al. (1974). It implies that for given mid potential $\tilde{\Phi}_0$, the potential distribution $\tilde{\Phi}(\tilde{z})$ can be calculated. Usually, however, the mid potential $\tilde{\Phi}_0$ is not a priori known and should be determined from the surface potential $\tilde{\Phi}_s$ and channel width $2H$. This is done as follows. The channel width is expressed in terms of Debye length from (2.35)

$$\tilde{H} = H\kappa = 2\sqrt{\mathbf{r}} \left(F\left(\frac{1}{2}\pi, \mathbf{r}\right) - F(\theta_s, \mathbf{r}) \right), \quad (2.36)$$

where

$$\sin(\theta_s) = e^{-\frac{1}{2}(\tilde{\Phi}_s - \tilde{\Phi}_0)}. \quad (2.37)$$

This implies that for given $\tilde{\Phi}_s$, the position of the wall \tilde{H} can be determined as a function of the mid potential $\tilde{\Phi}_0$. The result is plotted in Figure 2.5. The value $2\tilde{H}$ is called electrokinetic channel width. Note that we plotted $\tilde{\Phi}_0/\zeta = \tilde{\Phi}_0/\tilde{\Phi}_s$ on the ordinate. It becomes clear that for $\tilde{H} = 0$, the mid potential equals the wall surface potential ζ . For wider channels the mid potential has ample space to tend to zero. The linearized solution obeying the boundary conditions (2.30) and (2.31) is given by

$$\tilde{\Phi} = \tilde{\Phi}_0 \cosh \tilde{z}, \quad (2.38)$$

so that

$$\tilde{\Phi}_s = \tilde{\Phi}_0 \cosh \tilde{H}, \quad (2.39)$$

which means that $\tilde{\Phi}_0/\tilde{\Phi}_s = \Phi_0/\zeta = 1/\cosh(\tilde{H})$. This curve is also plotted in Figure 2.5. We notice that for higher zeta-potential deviations from linearized theory become more pronounced. Having now determined the mid potential $\tilde{\Phi}_0$ for a given channel width and zeta-potential, the full potential distribution $\tilde{\Phi}(\tilde{z})$ is computed from (2.35).

In Figure 2.6 we plot the potential distribution $\tilde{\Phi}/\tilde{\Phi}_s = \Phi/\zeta$ over the channel for different channel widths. For a relatively wide channel $\Phi_0 = 0.02\zeta$ implying $\tilde{H} = 4.5844$, the distribution closely follows the linearized solution $\tilde{\Phi}/\tilde{\Phi}_s = \cosh(\tilde{z})/\cosh(\tilde{H})$. For narrower channels $\Phi_0 = 0.25\zeta$ ($\tilde{H} = 2.0357$) and $\Phi_0 = 0.62\zeta$ ($\tilde{H} = 1.0169$), deviations from linearized solutions become more obvious.

In Figure 2.7, the same procedure is repeated for higher zeta-potential. We observe that deviations from linearized theory are much stronger now. Making it necessary to use the nonlinearized PBE equation for small channels.

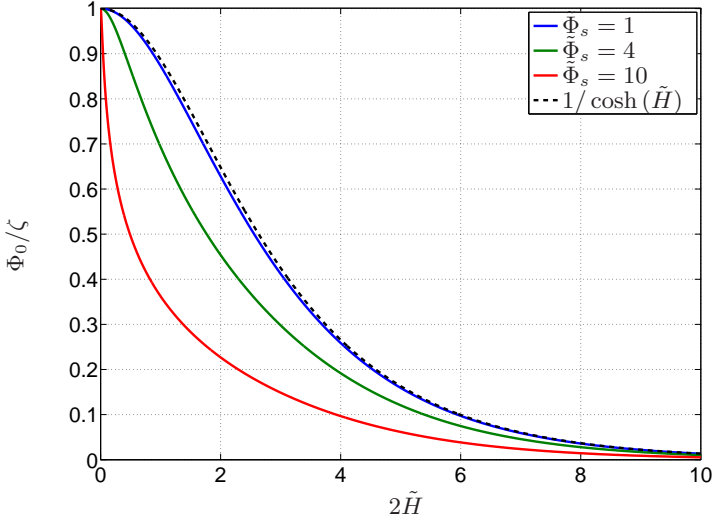


Figure 2.5: Variation of the mid potential with electrokinetic channel width.

2.2.2 Electro-osmotic flow in a narrow parallel-plate channel

Having obtained the potential and charge distributions in a narrow parallel-plate channel, we are now able to address flow phenomena. Considering the case of a laminar flow between parallel plates under steady conditions, the viscous forces are balanced by the pressure gradient and electric body forces generated by an axial electric field E_x

$$-\frac{\partial p}{\partial x} + \eta \frac{\partial^2 v_x}{\partial z^2} + \rho_E E_x = 0. \quad (2.40)$$

Substitution of the charge density (2.4) in (2.40) yields that

$$-\frac{\partial p}{\partial x} + \eta \frac{\partial^2 v_x}{\partial z^2} - \varepsilon \frac{d^2 \Phi}{dz^2} E_x = 0. \quad (2.41)$$

The axial velocity v_x is composed of two discrete parts. The first, v_0 is the laminar flow caused by the pressure gradient alone. The second is the electro-osmotic velocity v_e . If only pressure and viscous forces were present, the momentum balance would be

$$-\frac{\partial p}{\partial x} + \eta \frac{\partial^2 v_0}{\partial z^2} = 0. \quad (2.42)$$

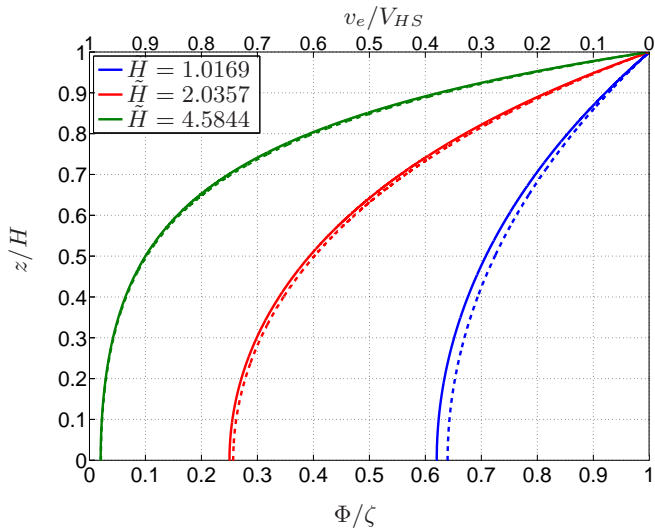


Figure 2.6: Potential and velocity distribution for $\zeta = \Phi_B$. Dashed lines indicate linearized theory.

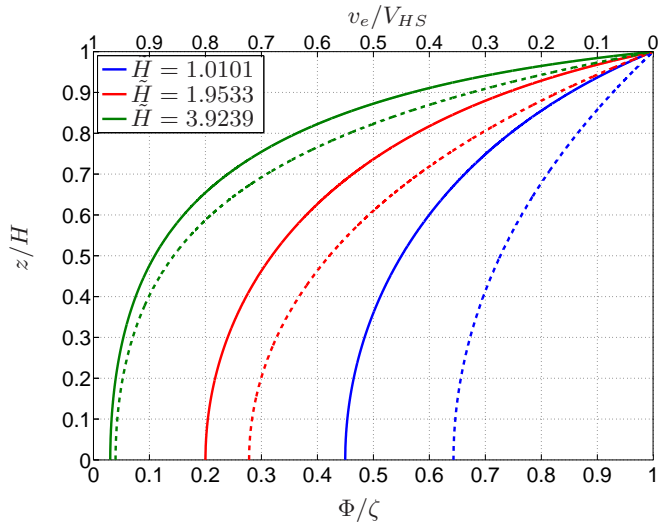


Figure 2.7: Potential and velocity distribution for $\zeta = 4\Phi_B$. Dashed lines indicate linearized theory.

If only electric body forces and viscous forces were acting, the momentum balance would give

$$\eta \frac{\partial^2 v_e}{\partial z^2} - \varepsilon \frac{d^2 \Phi}{dz^2} E_x = 0. \quad (2.43)$$

The addition of (2.42) and (2.43) yields (2.41), in which

$$v_x = v_0 + v_e. \quad (2.44)$$

The general solution of (2.43) is given by

$$v_e = \frac{\varepsilon E_x}{\eta} \Phi + Cz + D, \quad (2.45)$$

where C and D are arbitrary constants. The boundary conditions that apply are $v_e = 0$ and $\Phi = \zeta$ at the surface of the slit. We also have that $\partial v_e / \partial z = \partial \Phi / \partial z = 0$ at the center, which results in

$$v_e = -\frac{\varepsilon E_x \zeta}{\eta} \left(1 - \frac{\Phi}{\zeta}\right) = -V_{HS} \left(1 - \frac{\Phi}{\zeta}\right). \quad (2.46)$$

here

$$V_{HS} = \frac{\varepsilon \zeta}{\eta} E_x, \quad (2.47)$$

which is the so-called Helmholtz-Smoluchowski velocity [Masliyah and Bhattacharjee (2006), Pasquale et al. (1986)]. The Helmholtz-Smoluchowski equation describes electro-osmotic flow, where an electrical field creates fluid flow. This means that the velocity profiles from (2.46) can be plotted in Figures (2.6) and (2.7) as well, as we have done. Note that the actual Helmholtz-Smoluchowski velocity is not attained in the channel. To do so, the potential Φ should become zero, which is only the case for wider channels or far away from single wall channels as discussed in subsection 2.1.1.

The final solution of (2.40) will therefore be of the form

$$v_x = -\frac{1}{2\eta} \frac{\partial p}{\partial x} (H^2 - z^2) - V_{HS} \left(1 - \frac{\Phi}{\zeta}\right), \quad (2.48)$$

where we have adopted the Poiseuille flow profile for the pressure-driven flow. The mean velocity of flow in a slit is given by the expression

$$\bar{v}_x = -\frac{H^2}{3\eta} \frac{\partial p}{\partial x} - \frac{V_{HS}}{H} \int_0^H \left(1 - \frac{\Phi}{\zeta}\right) dz. \quad (2.49)$$

Introducing the function

$$G_q = \int_0^1 \frac{\Phi}{\zeta} d\frac{z}{H}, \quad (2.50)$$

we find that

$$\bar{v}_x = -\frac{H^2}{3\eta} \frac{\partial p}{\partial x} - V_{HS}(1 - G_q). \quad (2.51)$$

The function G_q is found by straightforward numerical integration. Results are plotted in Figure 2.8 for different ζ -potentials. We find that for wide channel configurations the average flow velocity is given by the superposition of the Poiseuille flow and the Helmholtz-Smoluchowski result ($G_q \rightarrow 0$).

2.2.3 Streaming Potential in a narrow parallel-plate channel

It is now also possible to study the streaming potential. The pressure-driven hydraulic flow induces a convection current which is opposed by an induction current. The resulting induced electric field represents the open-circuit streaming potential (no net current in the flow direction). In general, the electric current density is given by the combined effect of charge diffusion, convection and electric field

$$J_x = -D \frac{\partial \rho_E}{\partial x} + \rho_E v_x + \sigma E_x, \quad (2.52)$$

with D the diffusion coefficient. For fully developed flow the diffusion term drops. Integration over the channel width yields that

$$I_x = 2 \int_0^H \rho_E v_0 dz - 2 \frac{\varepsilon E_x \zeta}{\eta} \int_0^H \rho_E \left(1 - \frac{\Phi}{\zeta}\right) dz + 2\sigma E_x H, \quad (2.53)$$

where it is assumed that σ is constant over the channel width [Burgreen and Nakache (1964)]. As we do not allow a net current in the x -direction, we find that

$$E_x = \frac{-\int_0^H v_0 \rho_E dz / (\sigma H)}{1 - \frac{\varepsilon \zeta}{\eta \sigma H} \int_0^H \rho_E \left(1 - \frac{\Phi}{\zeta}\right) dz}, \quad (2.54)$$

which represents the streaming potential. After substitution of the charge distribution, the integral term in the numerator is rewritten as

$$-\frac{1}{\sigma H} \int_0^H v_0 \rho_E dz = \frac{\varepsilon}{\sigma H} \int_0^H v_0 \frac{d^2 \Phi}{dz^2} dz. \quad (2.55)$$

In Appendix C this term is shown to become

$$\frac{\varepsilon}{\sigma H} \int_0^H v_0 \frac{d^2 \Phi}{dz^2} dz = -\frac{\partial p}{\partial x} \frac{M_q}{\sigma} (1 - G_q), \quad (2.56)$$

where $M_q = \varepsilon \zeta / \eta$ and G_q is plotted in Figure 2.8, as we have seen.

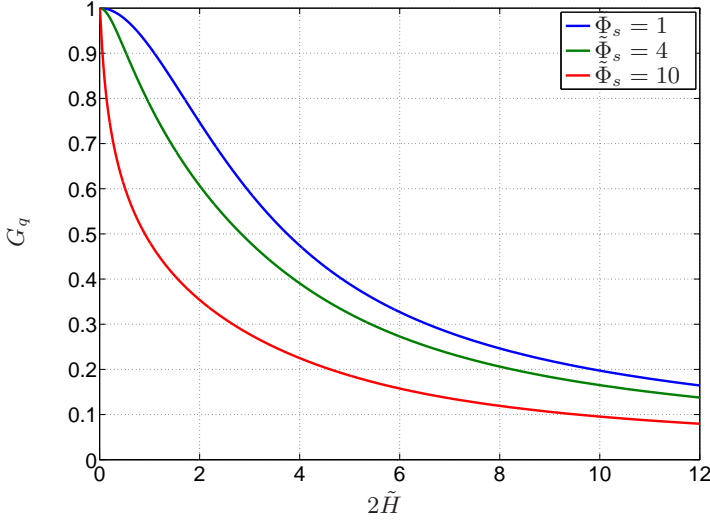


Figure 2.8: Variation of G_q with electrokinetic channel width.

The integral in the denominator of (2.54) can be evaluated analytically. We find that

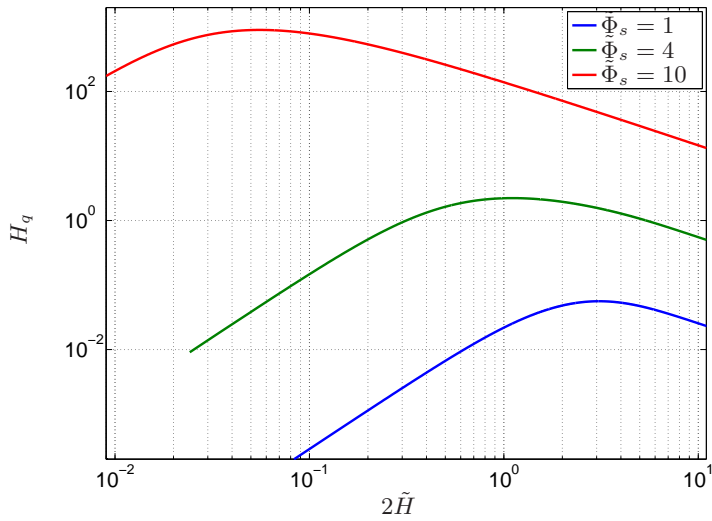
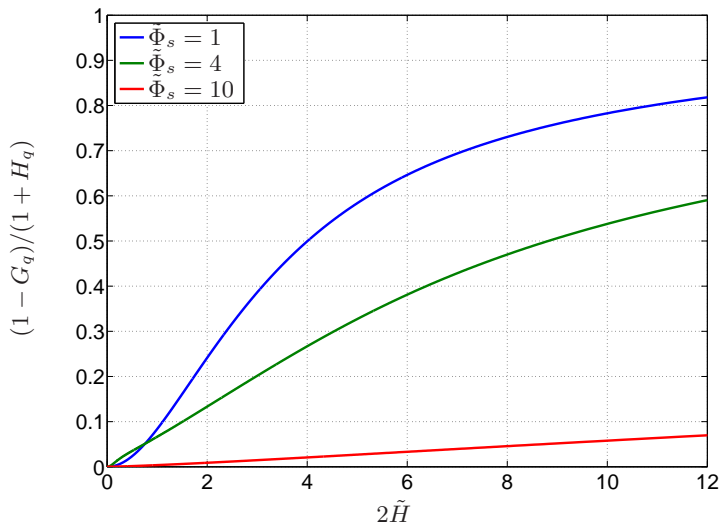
$$H_q = -\frac{M_q}{\sigma H} \int_0^H \rho_E \left(1 - \frac{\Phi}{\zeta}\right) dz = \frac{M_q \varepsilon \kappa^2 \Phi_B}{\sigma \tilde{H}} \int_0^{\tilde{H}} \frac{\partial^2 \tilde{\Phi}}{\partial \tilde{z}^2} \left(1 - \frac{\tilde{\Phi}}{\tilde{\Phi}_s}\right) d\tilde{z}. \quad (2.57)$$

We show in Appendix C that this integral can be evaluated in terms of elliptic integrals of the first and second kind

$$H_q = \frac{M_q \varepsilon \kappa^2 \Phi_B}{\sigma \tilde{H} \tilde{\Phi}_s} \frac{2}{\sqrt{\mathbf{r}}} H_{qr}, \quad (2.58)$$

where

$$H_{qr} = \Delta \theta_s \cot(\theta_s) + (\mathbf{r}^2 - 1) \left(F(\theta_s, \mathbf{r}) - F\left(\frac{\pi}{2}, \mathbf{r}\right) \right) + 2 \left(E(\theta_s, \mathbf{r}) - E\left(\frac{\pi}{2}, \mathbf{r}\right) \right), \quad (2.59)$$

Figure 2.9: Variation of H_q with electrokinetic channel width.Figure 2.10: Variation of $(1 - G_q)/(1 + H_q)$ with electrokinetic channel width.

with $F(\theta_s, \mathbf{r})$ and $E(\theta_s, \mathbf{r})$ the incomplete elliptic integral of the first and second kind respectively, $F(\frac{\pi}{2}, \mathbf{r})$ and $E(\frac{\pi}{2}, \mathbf{r})$ the corresponding complete integrals. Moreover

$$\Delta\theta_s = \sqrt{1 - \mathbf{r}^2 \sin^2(\theta_s)}, \quad (2.60)$$

is the so-called delta amplitude of the Jacobian elliptic functions. We now write

$$H_q = \frac{C_q H_{qr}}{\tilde{H} \sqrt{\mathbf{r}}}, \quad (2.61)$$

where $C_q = (2M_q \kappa^2 \varepsilon \Phi_B) / (\sigma \tilde{\Phi}_s) = (4N^\infty \varepsilon k_B T) / (\eta \sigma)$. In Figure 2.9, H_q is plotted as a function of channel width for different values of $\tilde{\Phi}_s$, choosing $C_q = 0.5$. Similar results were also obtained by Burgreen and Nakache (1964), but they used a different variable transformation. The foregoing considerations imply that the streaming potential can now be expressed from (2.54) as

$$E_x = -\frac{\partial p}{\partial x} \frac{M_q}{\sigma} \frac{(1 - G_q)}{(1 + H_q)}, \quad (2.62)$$

A plot of $(1 - G_q)/(1 + H_q)$ is given in Figure 2.10. We notice that for large channel widths, the value tends to zero, so that the value of the coupling coefficient, M_q/σ , can easily be determined from an experimental set-up where the induced electric field is measured as a function of the pressure drop, as we will see in (3.32).

2.3 The electroviscous effect

When a fluid flows through a narrow channel, it will encounter an additional opposing electrokinetic force that can be described by the introduction of an apparent viscosity η_a . Substitution of (2.62) in (2.51) yields that

$$\bar{v}_x = -\frac{H^2}{3\eta} \frac{\partial p}{\partial x} \left[1 - \frac{M_q^2}{\sigma} \frac{3\eta}{H^2} \frac{(1 - G_q)^2}{(1 + H_q)} \right]. \quad (2.63)$$

We define the apparent viscosity η_a as

$$\bar{v}_x = -\frac{H^2}{3\eta_a} \frac{\partial p}{\partial x}. \quad (2.64)$$

We thus easily find that

$$\frac{\eta_a}{\eta} = \left[1 - \frac{M_q^2}{\sigma} \frac{3\eta}{H^2} \frac{(1 - G_q)^2}{(1 + H_q)} \right]^{-1} = \left[1 - \frac{3}{2} C_m \frac{\tilde{\Phi}_s^2}{\tilde{H}^2} \frac{(1 - G_q)^2}{(1 + H_q)} \right]^{-1}. \quad (2.65)$$

In Figure 2.11 the apparent viscosity is shown as a function of the electrokinetic width $2\tilde{H}$. We notice that the apparent viscosity reaches a maximum value for small channel widths. For larger widths (larger than a few tens of nanometers), the effects become negligible so that we probably do not have to take these effects into account in steady permeability measurements.

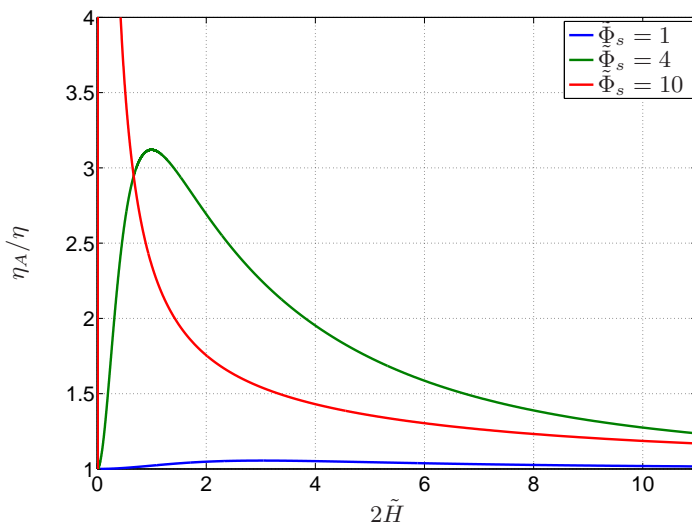


Figure 2.11: Artificial viscosity η_A/η as function of the electrokinetic width.

2.4 Electrokinetic flow in a cylindrical capillary

We now consider the case of a laminar flow within a cylindrical capillary under steady conditions. The viscous forces are balanced by the pressure gradient and electric body forces generated by an axial electric field E_x :

$$-\frac{\partial p}{\partial x} + \frac{\eta}{r} \frac{\partial}{\partial r} \left(r \frac{\partial v_x}{\partial r} \right) + \rho_E E_x = 0. \quad (2.66)$$

Substitution of the charge density (2.4) in (2.66) yields that

$$-\frac{\partial p}{\partial x} + \frac{\eta}{r} \frac{\partial}{\partial r} \left(r \frac{\partial v_x}{\partial r} \right) - \frac{\varepsilon E_x}{r} \frac{\partial}{\partial r} \left(r \frac{\partial \Phi}{\partial r} \right) = 0. \quad (2.67)$$

Again, the axial velocity v_x is composed of two discrete parts. The first, v_0 is the laminar flow caused by the pressure gradient alone. The second is the electro-osmotic velocity v_e . If only pressure and viscous forces were present, the momentum balance would be

$$-\frac{\partial p}{\partial x} + \frac{\eta}{r} \frac{\partial}{\partial r} \left(r \frac{\partial v_0}{\partial r} \right) = 0. \quad (2.68)$$

If only electric body forces and viscous forces were acting the momentum balance would give

$$\frac{\eta}{r} \frac{\partial}{\partial r} \left(r \frac{\partial v_e}{\partial r} \right) - \frac{\varepsilon E_x}{r} \frac{\partial}{\partial r} \left(r \frac{\partial \Phi}{\partial r} \right) = 0. \quad (2.69)$$

The addition of (2.68) and (2.69) yields (2.67), in which

$$v_x = v_0 + v_e. \quad (2.70)$$

The general solution of (2.69) is given by

$$v_e = \frac{\varepsilon E_x}{\eta} \Phi + C \ln(r) + D. \quad (2.71)$$

Using the same boundary conditions as for the channel (subsection 2.2.2), we find again that

$$v_e = -\frac{\varepsilon E_x \zeta}{\eta} \left(1 - \frac{\Phi}{\zeta} \right). \quad (2.72)$$

For a cylindrical capillary, the Poisson-Boltzmann equation (2.15) becomes

$$\frac{1}{r} \frac{\partial}{\partial r} \left(r \frac{\partial \tilde{\Phi}}{\partial r} \right) = \kappa^2 \sinh(\tilde{\Phi}). \quad (2.73)$$

Unfortunately, no exact solution exists for this inhomogeneous differential equation. Following Rice and Whitehead (1965), we thus linearize this equation to

$$\frac{1}{r} \frac{\partial}{\partial r} \left(r \frac{\partial \tilde{\Phi}}{\partial r} \right) = \kappa^2 \tilde{\Phi}, \quad (2.74)$$

whose solution satisfying the boundary condition $\tilde{\Phi} = \tilde{\Phi}_s$, at the wall, and remaining finite at $r = 0$ is given by

$$\frac{\tilde{\Phi}}{\tilde{\Phi}_s} = \frac{I_0(\kappa r)}{I_0(\kappa R_c)}, \quad (2.75)$$

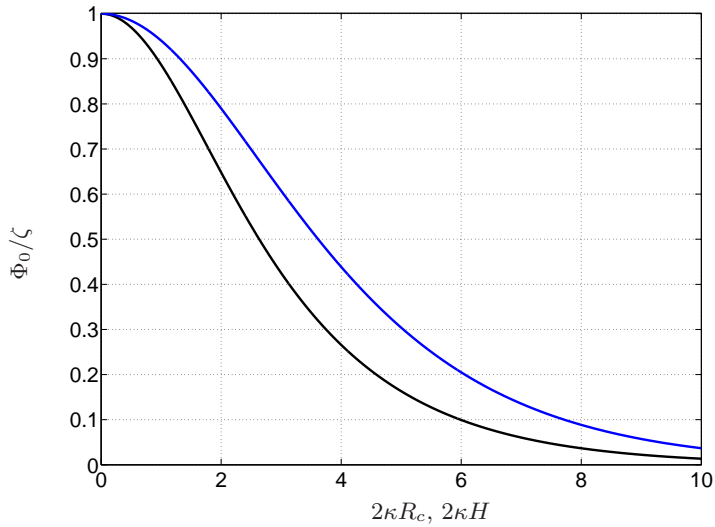


Figure 2.12: Variation of mid potential with electrokinetic width for both a cylindrical (blue) and a parallel-plate channel (black).

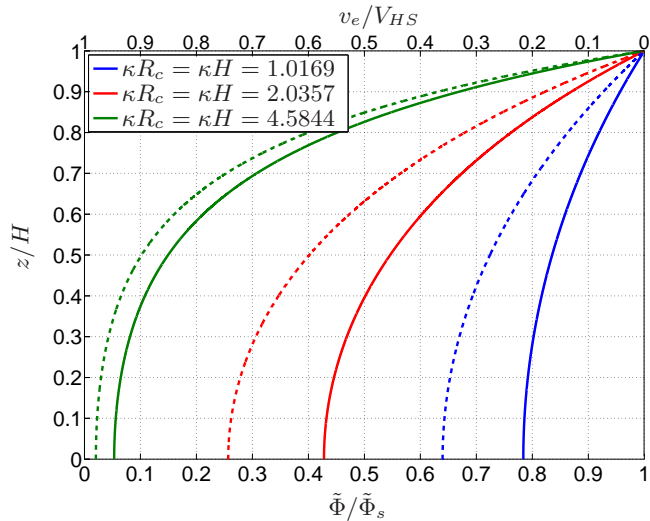


Figure 2.13: Linearized potential distribution for both a cylindrical, and a parallel-plate channel (dashed lines)

with R_c the radius of the capillary, and I_0 is the zero-order modified Bessel function of the first kind. For the mid-potential, we find that

$$\frac{\tilde{\Phi}_0}{\tilde{\Phi}_s} = \frac{1}{I_0(\kappa R_c)}, \quad (2.76)$$

In Figure 2.12, Φ_0/ζ versus electrokinetic diameter $2\kappa R_c$, is shown. It is compared with our earlier result for the parallel-plate channel (2.39). We notice that the behaviour is quite similar, although the cylinder mid-potential is higher, for all channel widths.

The potential distribution are given in Figure 2.7 where we compare the cylindrical and parallel-plate results, we see that the patterns are similar, but that large discrepancies occur for narrow channels. The net charge density is given by [Rice and Whitehead (1965)]

$$\rho_c = -\kappa^2 \varepsilon \zeta \frac{I_0(\kappa r)}{I_0(\kappa R_c)}. \quad (2.77)$$

For completeness, we now also derive the correction coefficients. The volume transport correction factor can be computed in analogy with (2.50):

$$G_q = \frac{1}{\pi R_c^2} \int_0^{R_c} \frac{I_0(\kappa r)}{I_0(\kappa R_c)} 2\pi r dr = \frac{2}{\kappa R_c} \frac{I_1(\kappa R_c)}{I_0(\kappa R_c)}. \quad (2.78)$$

For the correction factor to Ohm's law we write from (2.57)

$$\begin{aligned} H_q &= -\frac{M_q}{\sigma A} \int_0^{R_c} \rho_c \left(1 - \frac{\Phi}{\Phi_s}\right) dA = \\ &= \frac{2\pi M_q \varepsilon \kappa^2 \zeta}{\sigma \pi R_c^2} \left[\int_0^{\tilde{R}_c} \frac{I_0(\kappa r)}{I_0(\kappa R_c)} r dr - \int_0^{R_c} \frac{I_0^2(\kappa r)}{I_0^2(\kappa R_c)} r dr \right]. \end{aligned} \quad (2.79)$$

Noticing that the second integral is of the Lommel type, we find that

$$H_q = -\frac{M_q \kappa^2 \varepsilon \zeta}{\sigma} \left[1 - \frac{2}{\kappa R_c} \frac{I_1(\kappa R_c)}{I_0(\kappa R_c)} - \frac{I_1^2(\kappa R_c)}{I_0^2(\kappa R_c)} \right]. \quad (2.80)$$

which is in agreement with Rice and Whitehead (1965).

Chapter 3

Dynamic coupling coefficients

In this chapter oscillatory gradients are applied to analyze the frequency dependency of the transport coefficients over a wide frequency range. The results are compared with theoretical results by Johnson et al. (1987) and Pride (1994). A sensitivity analysis is performed.

3.1 Newtonian viscous-flow equations

In many areas of geoscience, it is important to know how fluid flows within porous media. The motion of a fluid in a porous medium is controlled by the pore geometry and the fluid's properties. The phenomenological coefficients are essential to describe macroscopic flow through porous media (using the Biot equations as described in Chapter 4). For two simple geometries, it is possible to describe the fluid behaviour and also the electrokinetic properties (at microscale). This information will be used for the transport coefficients.

3.1.1 Dynamic permeability

We consider Navier-Stokes' equation for a cylindrical capillary with radius R_c during incompressible laminar flow where no electric gradient is applied:

$$\rho_f \frac{\partial v_x}{\partial t} = -\frac{dp}{dx} + \frac{\eta}{r} \frac{\partial}{\partial r} \left(r \frac{\partial v_x}{\partial r} \right), \quad (3.1)$$

with v_x the fluid velocity along the cylindrical capillary. Initial and boundary conditions for axial symmetric flow are given by

$$\begin{aligned} v_x(r, 0) &= 0, \\ v_x(R_c, t) &= 0, \end{aligned} \quad (3.2)$$

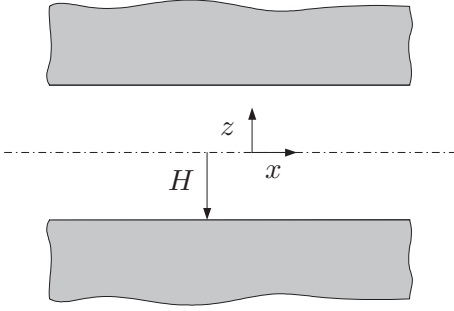


Figure 3.1: Fluid flow through 2-D parallel-plate channel.

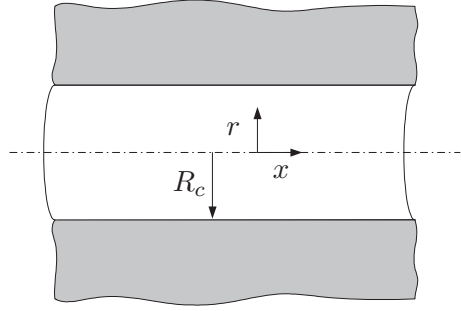


Figure 3.2: Fluid flow through capillary.

and the velocity at $r = 0$ has to remain finite at all times. A constant pressure gradient is imposed at $t = 0$. The solution was given by El-Sahed and Salem (2004)

$$\frac{v_x(r, t)}{v_{max}} = (1 - \tilde{r}^2) - \sum_{n=1}^{\infty} \frac{8J_0(\lambda_n \tilde{r})}{\lambda_n^3 J_1(\lambda_n)} e^{-\lambda_n^2 \tau}, \quad (3.3)$$

where $\tau = \eta t / (\rho_f R_c^2)$ is the dimensionless time, $\tilde{r} = r / R_c$ the dimensionless radius position, $v_{max} = (-\partial p / \partial x)(R_c^2 / (4\eta))$ is the maximum velocity during fully developed flow, and λ_n are the roots of the Bessel function J_0 [El-Sahed and Salem (2004), White (2005)]. Steady Poiseuille flow has the form

$$v_x(r, t) = v_{max}(1 - \tilde{r}^2). \quad (3.4)$$

The fluid profile for different times is plotted in Figure 3.3 for a water-filled capillary with $R_c = 5 \cdot 10^{-4}$ m. We note that eventually the fully developed Poiseuille flow profile is reached indeed.

Next we consider harmonic motion. Using the temporal Fourier transform

$$\hat{f}(\mathbf{x}, \omega) = \int_{-\infty}^{\infty} f(\mathbf{x}, t) e^{-i\omega t} dt, \quad (3.5)$$

we obtain from (3.1)

$$\frac{\partial^2 \hat{v}_x}{\partial r^2} + \frac{1}{r} \frac{\partial \hat{v}_x}{\partial r} - \rho_f \frac{i\omega}{\eta} \hat{v}_x = \frac{1}{\eta} \frac{\partial \hat{p}}{\partial x}. \quad (3.6)$$

The solution will have the form

$$\hat{v}_x(r, \omega) = A J_0(\varpi r) + \frac{1}{\eta \varpi^2} \frac{\partial \hat{p}}{\partial x}, \quad (3.7)$$

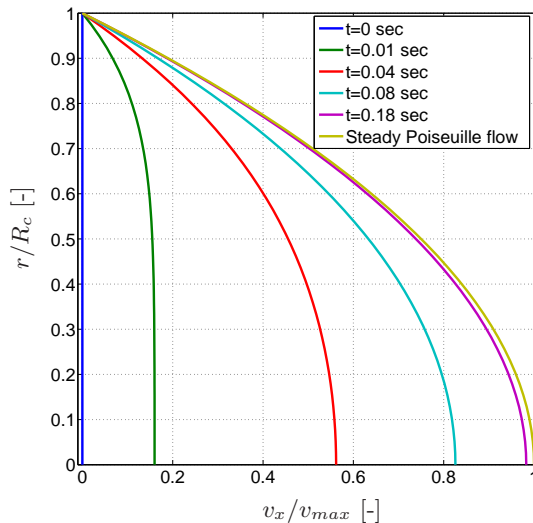


Figure 3.3: Fluid velocity profile in capillary due to pressure gradient.

where

$$\varpi^2 = -\rho_f \frac{i\omega}{\eta}, \quad \text{Real}(\varpi) \geq 0, \quad (3.8)$$

and A is an arbitrary constant. Application of the no-slip boundary condition at the wall results in the following velocity profile within the cylindrical capillary

$$\hat{v}_x(r, \omega) = \frac{1}{\eta\varpi^2} \frac{\partial \hat{p}}{\partial x} \left(1 - \frac{J_0(\varpi r)}{J_0(\varpi R_c)} \right), \quad (3.9)$$

with J_0 the Bessel function of order zero. The average velocity over the entire cross-section of the tube is

$$\hat{v}_x(\omega) = \frac{1}{\pi R_c^2} \int_0^{R_c} \hat{v}_x(r, \omega) 2\pi r dr = \frac{1}{\eta\varpi^2} \frac{\partial \hat{p}}{\partial x} \left(1 - \frac{2}{\varpi R_c} \frac{J_1(\varpi R_c)}{J_0(\varpi R_c)} \right). \quad (3.10)$$

with J_1 the Bessel functions of order one. The friction (wall shear stress) at the wall of the cylindrical capillary is given by

$$\tau_w = -\eta \left(\frac{\partial \hat{v}_x}{\partial r} \right)_{r=R_c}. \quad (3.11)$$

The total friction force excited by the fluid on the wall, per unit average

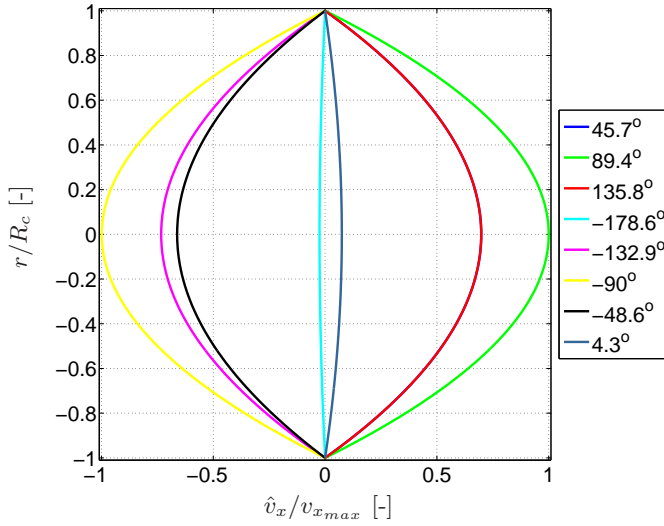


Figure 3.4: Womersley profiles for different $\hat{\alpha}_w$ numbers, $\alpha_w = 0.1$.

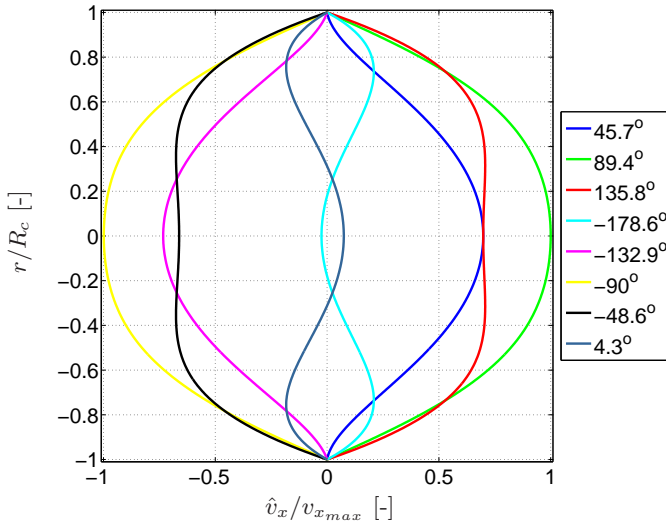


Figure 3.5: Womersley profiles for different $\hat{\alpha}_w$ numbers, $\alpha_w = 4$.

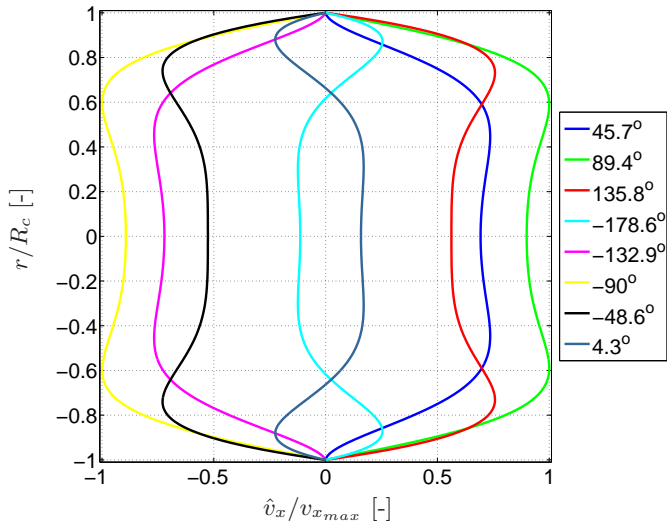


Figure 3.6: Womersley profiles for different $\hat{\alpha}_w$ numbers, $\alpha_w = 8$.

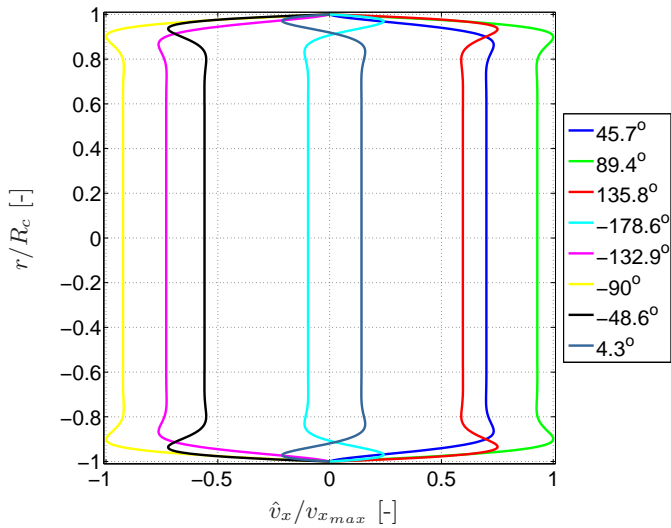


Figure 3.7: Womersley profiles for different $\hat{\alpha}_w$ numbers, $\alpha_w = 32$.

fluid velocity, can be computed by considering the ratio

$$\frac{2\pi R_c \tau_w}{\hat{v}_x} = \frac{-2\pi\eta(\varpi R_c)^2 J_1(\varpi R_c)}{(\varpi R_c)J_0(\varpi R_c) - 2J_1(\varpi R_c)}. \quad (3.12)$$

For the case that the frequency is zero, the total friction force equals that of the Poiseuille flow:

$$\lim_{\omega \rightarrow 0} \frac{2\pi R_c \tau_w}{\hat{v}_x} = 8\pi\eta. \quad (3.13)$$

We now define the so-called Womersley parameter α_w so that

$$\alpha_w = R_c \sqrt{\frac{\rho_f \omega}{\eta}}. \quad (3.14)$$

The solution (3.9) for a harmonic pressure gradient in a capillary tube can now be expressed as

$$\hat{v}_x(r, \omega) = \frac{i}{\rho_f \omega} \frac{\partial \hat{p}}{\partial x} \left(1 - \frac{J_0(\alpha_w \frac{r}{R_c} \sqrt{-i})}{J_0(\alpha_w \sqrt{-i})} \right), \quad \text{Real}(\alpha_w \sqrt{-i}) \geq 0, \quad (3.15)$$

In Figures 3.4 and 3.7 we plot several velocity profiles for different phases. The fluid profiles have been normalized using $\hat{v}_x(r, \omega)$ at the maximum phase angle $v_{x_{max}}$. It can be seen that there is a significant difference between small Womersley numbers $\alpha_w < 3$ and large Womersley numbers $\alpha_w > 10$. For low values of the Womersley number, viscous effects dominate and the profile becomes parabolic. For medium range Womersley numbers $3 < \alpha_w < 10$ a phase-shift occurs between the flow in the boundary layer and the flow in the central core of the tube. In the boundary layer viscous forces dominate over inertia forces and the flow profile will become flattened. For high Womersley numbers, the inertia forces are dominant in the central core and flattened profiles shifted in phase can be found [Womersley (2002)]. The experimental measurements, as described in Chapter 5 range up to 600 Hz, with relative small capillaries. Therefore the corresponding Womersley number will be in the low and intermediate range as we will see.

For a parallel-plate channel, the velocity distribution is given by Biot (1956b)

$$\hat{v}_x = \frac{1}{\eta \mathbf{w}^2} \left(1 - \frac{\cosh(\mathbf{w}z)}{\cosh(\mathbf{w}H)} \right) \frac{\partial \hat{p}}{\partial x}, \quad (3.16)$$

where $\mathbf{w} = \sqrt{\rho_f i \omega / \eta}$ for $\text{Real}(\mathbf{w}) \geq 0$. The average velocity of the entire cross-section of the tube is

$$\hat{v}_x = \frac{1}{H} \int_0^H \hat{v}_x dz = \frac{1}{\eta \mathbf{w}^2} \left(1 - \frac{\tanh(\mathbf{w}H)}{\mathbf{w}H} \right) \frac{\partial \hat{p}}{\partial x}. \quad (3.17)$$

3.1.2 Dynamic permeability

The dynamic permeability $\hat{k}(\omega)$ is an important property for macroscopic flow through porous media subjected to an oscillatory pressure gradient. It describes the transition from low-frequency viscosity dominated flow towards high-frequency inertia-dominated flow. This means that the conventional Darcy relation has to be generalized in order to incorporate both effects

$$\hat{W}(\omega) = -\frac{\hat{k}(\omega)}{\eta} \nabla p, \quad (3.18)$$

with $\hat{W} = \phi(\hat{\mathbf{v}}_f - \hat{\mathbf{v}}_s)$ the average flow velocity [Sheng and Zhou (1988)]. For a porous medium consisting of an ensemble of parallel tubes, the dynamic (frequency-dependent or AC) permeability can be computed from (3.10) and the definition of the static permeability $k_0 = (1/8)R_c^2$:

$$\hat{k}(\omega) = k_0 \left[\frac{-8}{(\varpi R_c)^2} \left(1 - \frac{2}{\varpi R_c} \frac{J_1(\varpi R_c)}{J_0(\varpi R_c)} \right) \right]. \quad (3.19)$$

The dynamic permeability for a parallel-plate configuration can be computed in a similar way from (3.17) and using the definition of static permeability $k_0 = (1/3)H^2$

$$k(\omega) = k_0 \left[\frac{3}{(\mathfrak{w}H)^2} \left(1 - \frac{1}{\mathfrak{w}H} \tanh(\mathfrak{w}H) \right) \right]. \quad (3.20)$$

The dynamic permeability for a porous medium of arbitrary shape was later described by Johnson et al. (1987)

$$\hat{k}(\omega) = k_0 \left[\left(1 + i \frac{m}{2} \frac{\omega}{\omega_c} \right)^{\frac{1}{2}} + i \frac{\omega}{\omega_c} \right]^{-1}, \quad (3.21)$$

where $\omega_c = (\eta\phi)/(\rho_f k_0 \alpha_\infty)$ is the rollover (or critical) frequency describing the transition from low-frequency viscosity dominated flow towards high-frequency inertia dominated flow. The shape factor m (usually taken 1) is a measure for the ruggedness of the pore morphology, at the microscopic scale. The general dynamic permeability equation not only describes the high and low frequencies but also the transition region [Johnson et al. (1987), Sheng and Zhou (1988), Pride et al. (1993)]. The absolute and phase values of the dynamic permeability of a cylindrical results are compared with the expression by Johnson et al. (1987) in Figures 3.8 and 3.9. Also the electric coupling factor is plotted, but this will be treated in the forthcoming. We

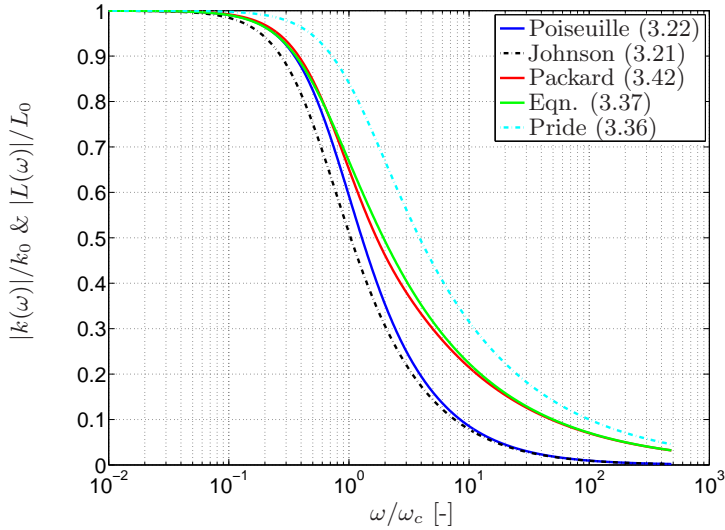


Figure 3.8: Magnitude of dynamic permeability and dynamic coupling coefficient. Both transport coefficients are normalized. Capillary radius $R_c = 3.5 \cdot 10^{-5}$ m.

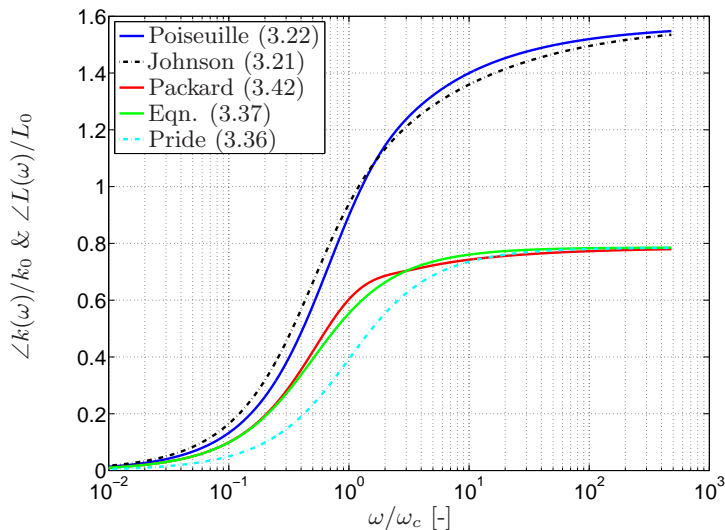


Figure 3.9: Phase of dynamic permeability and dynamic coupling coefficient. Both transport coefficients are normalized. Capillary radius $R_c = 3.5 \cdot 10^{-5}$ m and the shape factor $m = 1$.

Table 3.1: Dimensions of two randomly chosen capillary tubes.

Parameter	Unit	Value	Dimension
Radius capillary 1	R_1	$2.5 \cdot 10^{-4}$	[m]
Radius capillary 2	R_2	$3.5 \cdot 10^{-5}$	[m]
Porosity 1	ϕ_1	$1.8 \cdot 10^{-4}$	[-]
Porosity 2	ϕ_2	$3.6 \cdot 10^{-6}$	[-]
Length capillary 1	L_1	$6.4 \cdot 10^{-2}$	[m]
Length capillary 2	L_2	$1.64 \cdot 10^{-1}$	[m]

really see that the dynamic permeability tends to its steady-state value k_0 for low-frequencies. In this frequency regime, there is no phase lag between applied pressure gradient and resulting fluid flux. For high-frequencies, the fluid is no longer able to respond to the pressure oscillation resulting in a decreasing absolute value of the dynamic permeability and an increasing phase lag approaching 90° as its limiting value. We notice that, overall, the Johnson model accurately predicts the tube flow behaviour.

3.1.3 Multi-layered media

For multi-layered media, the dynamic permeability can be expressed in terms of weighted averaging:

$$\frac{1}{\hat{k}_P(\omega)} = \sum_{i=1}^N \frac{L_i}{L_{tot}} \frac{1}{\hat{k}_i(\omega)}. \quad (3.22)$$

where N is the number of layers, and L_i and $\hat{k}_i(\omega)$ are the length and permeability of the i -th layer, respectively. L_{tot} is the total sample length. We now consider a bimodal sample consisting of capillary tubes only. Layer 1 has tube radius R_1 , length L_1 , and porosity ϕ_1 , and layer 2 has tube radius R_2 , length L_2 , and porosity ϕ_2 . We assume that the sample is filled with water using (3.19), the dynamic permeability of each layer can be computed, and consequently also the total permeability, using (3.22). The input parameters are summarized in table 3.1 The results are given in Figures 3.10 and 3.11. We notice that also in this case the Johnson model gives a very accurate description of the sample permeability.

Dynamic coupling coefficient in a capillary

For an electrolyte flowing within a capillary, the transport of charge of the electrolyte per unit time along the tube is given by the convection current [Packard (1953)]

$$\hat{I}_{conv} = \int_0^{R_c} 2\pi r \cdot \hat{v}_x \rho_E dr, \quad (3.23)$$

Evaluating (3.23) using the electric charge density (2.4) and the fluid velocity profile (3.7) yields that

$$\hat{I}_{conv} = -\frac{2\pi\varepsilon}{\eta\varpi^2} \frac{\partial \hat{p}}{\partial x} \int_0^{R_c} \left[1 - \frac{J_0(\varpi r)}{J_0(\varpi R_c)} \right] d \left(r \frac{d\Phi}{dr} \right). \quad (3.24)$$

Integration by parts yields that

$$\hat{I}_{conv} = \frac{2\pi\varepsilon}{\eta\varpi^2} \frac{\partial \hat{p}}{\partial x} \int_{\Phi_0}^{\zeta} \varpi r \frac{J_1(\varpi r)}{J_0(\varpi R_c)} d\Phi. \quad (3.25)$$

Upon integration by parts again, we find that

$$\hat{I}_{conv} = \frac{2\pi\varepsilon_0\varepsilon_{rf}}{\eta\varpi^2} \frac{\partial \hat{p}}{\partial x} \varpi R_c \frac{J_1(\varpi R_c)}{J_0(\varpi R_c)}, \quad (3.26)$$

where the remaining integral after this second integration by parts has been neglected, because the diameter of the capillary is large compared to the thickness of the double layer. This corresponds to the steady flow situation described in the previous chapter, for $G_q = 0$. As we have seen, this only holds for wide enough capillaries. Streaming potential now applies if no net electric current is allowed. Ion transport sets up the electric convective current I_{conv} that has to be balanced by a conductive current. This conduction current induces an electric field that is associated with the streaming potential, The expression for the electric current now becomes

$$\hat{I}_{conv} + \sigma \hat{E}_x A = 0, \quad (3.27)$$

where \hat{E}_x is the induced electric field. This corresponds to the steady flow situation with $H_q = 0$ for wide capillaries. From (3.27) we thus find that

$$\hat{E}_x = - \left(\frac{\varepsilon\zeta}{\sigma\eta} \right) \left[\frac{2}{\varpi R_c} \frac{J_1(\varpi R_c)}{J_0(\varpi R_c)} \right] \frac{\partial \hat{p}}{\partial x}. \quad (3.28)$$

This is called the Packard approach [Packard (1953)]. We will see later that the ratio $\hat{E}_x/(\partial \hat{p}/\partial x)$ equals the coupling coefficient $\hat{L}(\omega)/\sigma$ in porous media. Introducing $L_0 = -\varepsilon\zeta/\eta$ we obtain

$$\frac{L(\omega)}{L_0} = -\frac{\hat{E}_x}{\partial \hat{p}/\partial x} \frac{\sigma\eta}{\varepsilon\zeta} = \frac{2}{\varpi R_c} \frac{J_1(\varpi R_c)}{J_0(\varpi R_c)}. \quad (3.29)$$

Dynamic coupling coefficient in a parallel-plate channel

Performing a similar integration as before, we obtain for the parallel-plate channel

$$\hat{I}_{conv} = -\frac{2\varepsilon}{\eta\mathfrak{w}^2} \frac{\partial p}{\partial x} \left[\left(1 - \frac{\cosh(\mathfrak{w}z)}{\cosh(\mathfrak{w}H)} \right) \frac{\partial \Phi}{\partial z} \Big|_0^H + \int_0^H \frac{\partial \Phi}{\partial z} d \left(1 - \frac{\cosh(\mathfrak{w}z)}{\cosh(\mathfrak{w}H)} \right) \right]. \quad (3.30)$$

The first part between the square brackets is zero, so that we have that

$$I_{conv} = -\frac{2\zeta\varepsilon}{\eta\mathfrak{w}} \frac{\partial \hat{p}}{\partial x} \tanh(\mathfrak{w}H). \quad (3.31)$$

The induced electric field is then given by

$$\hat{E}_x = \left(\frac{\varepsilon\zeta}{\sigma\eta} \right) \left[\frac{1}{\mathfrak{w}H} \tanh(\mathfrak{w}H) \right] \frac{\partial \hat{p}}{\partial x}, \quad (3.32)$$

so that we have

$$\frac{L(\omega)}{L_0} = -\frac{1}{\mathfrak{w}H} \tanh(\mathfrak{w}H), \quad (3.33)$$

In 1994, Pride introduced a generalized coupling function

$$\frac{L(\omega)}{L_0} = \left[1 + i \frac{\omega}{\omega_c} \frac{2}{m} \left(1 - 2 \frac{d}{\Lambda} \right)^2 \left(1 + d \sqrt{\frac{i\omega\rho_f}{\eta}} \right)^2 \right]^{-\frac{1}{2}}, \quad (3.34)$$

where Λ is a characteristic pore size parameter. The Debye length is denoted d and L_0 is the static electrokinetic coupling coefficient for a porous medium [Pride (1994)]

$$L_0 = -\frac{\phi}{\alpha_\infty} \frac{\varepsilon\zeta}{\eta} \left(1 - 2 \frac{d}{\Lambda} \right). \quad (3.35)$$

We notice that Pride (1994) uses an additional relaxation mechanism when the complex viscous skin depth becomes smaller than the Debye length. In most natural porous materials, relaxation never takes place, for commonly encountered frequencies and salinities. Therefore Pride and Garambois (2005) proposed a simplified version of (3.34)

$$\frac{\hat{L}(\omega)}{L_0} = \left[1 + i \frac{\omega}{\omega_c} \right]^{-\frac{1}{2}}. \quad (3.36)$$

which has the limitation that the shape factor should be equal to 2. However m usually is taken 1, see Figures 3.8 and 3.9, in that case we should use

$$\hat{L}(\omega) = L_0 \left[1 + i \frac{\omega}{\omega_c} \frac{2}{m} \right]^{-\frac{1}{2}}. \quad (3.37)$$

In Figures 3.8 and 3.9 absolute and phase values of the electric coupling coefficients are plotted. It becomes evident that Pride's simplified model predicts the same trends as computed for the capillary tubes, but the response is shifted in frequency.

For the phase values it is conspicuous that the high-frequency limiting phase lag is 45° , which is quite different from the 90° phase lag for the dynamic permeability. This is simply because $L(\omega)/L_0$ displays $(i\omega/\omega_c)^{-\frac{1}{2}}$ behaviour at high frequencies, whereas $k(\omega)/k_0$ scales as $(i\omega/\omega_c)^{-1}$ for high frequencies.

3.1.4 Multi-layered media EK coupling

In a similar manner to the derivation of the dynamic permeability for multi-layered media (subsection 3.1.3), it is possible to obtain the dynamic coupling coefficient for a series of tubes.

Considering Ohm's law, (4.20) for the case where the electric current density equals zero.

$$\hat{L}(\omega) = -\hat{\sigma}(\omega) \frac{\nabla \Phi}{\nabla p}. \quad (3.38)$$

Summing the pressure difference and potential difference together

$$\hat{\sigma}(\omega) \sum_i^N \Delta \Phi_i = - \sum_{i=1}^N \Delta p_i \hat{L}_i(\omega). \quad (3.39)$$

Combining the potential difference with Darcy's law

$$\hat{\sigma}(\omega) \Delta \Phi = - \sum_{i=1}^N \hat{L}_i(\omega) \frac{\eta \phi_i}{\hat{k}_i(\omega)} v_{xi} L_i, \quad (3.40)$$

rewritten

$$\hat{\sigma}(\omega) \Delta \Phi = -\eta \phi v_x L_{tot} \left[\sum_{i=1}^N \frac{L_i}{L_{tot}} \frac{\hat{L}_i(\omega)}{\hat{k}_i(\omega)} \right]. \quad (3.41)$$

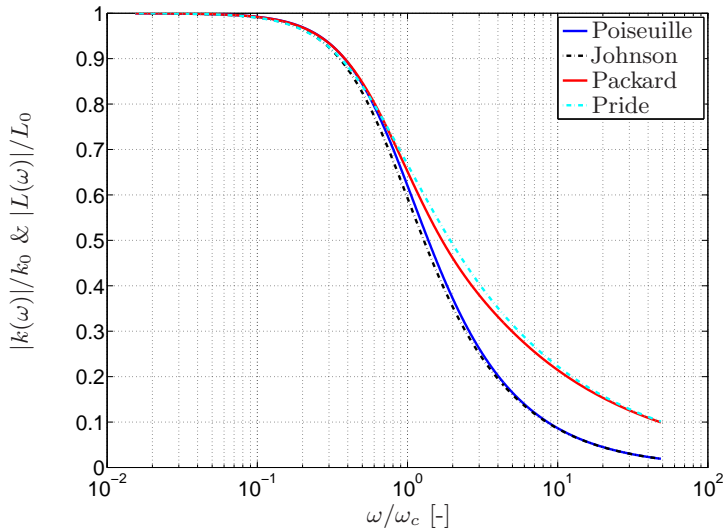


Figure 3.10: Real value of dynamic permeability and dynamic coupling coefficient for analytical solution and approximate solution.

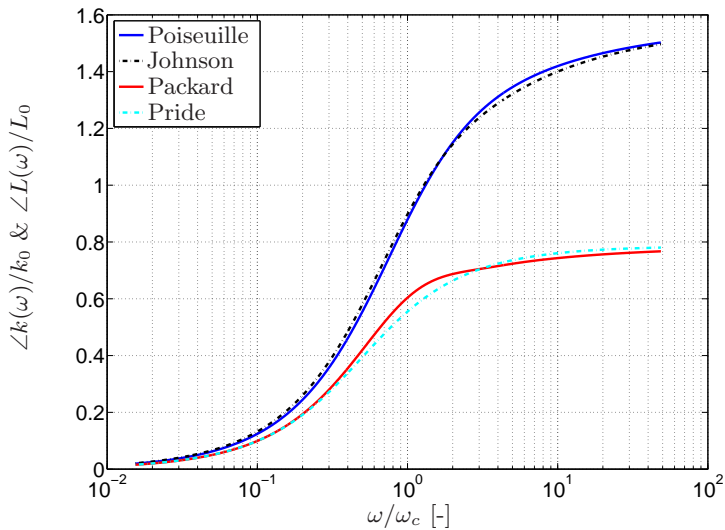


Figure 3.11: Imaginary value of dynamic permeability and dynamic coupling coefficient for analytical solution and approximate solution.

Dividing (3.41) by the total pressure difference results in the dynamic coupling coefficient

$$\hat{L}_P(\omega) = \hat{k}_P(\omega) \left[\sum_{i=1}^N \frac{L_i}{L_{tot}} \frac{\hat{L}_i(\omega)}{\hat{k}_i(\omega)} \right]. \quad (3.42)$$

In Figures 3.10 and 3.11 good agreement of the analytical solution for a capillary tube (Poiseuille and Packard) (3.42) versus the coefficient for a general arbitrary geometry (Johnson and Pride) (3.34) are shown.

3.1.5 Principles of electro-osmosis

In Chapter 2, we have seen that the fluid velocity in a capillary tube is given by

$$v_x = \frac{\varepsilon E_x}{\eta} (\Phi - \zeta). \quad (3.43)$$

As the counter-ions in the fluid collect near the wall, the electric field potential Φ rapidly decays as one moves away from the surface [Masliyah and Bhattacharjee (2006)]. This means that in the bulk of the capillary we find that

$$v_x = -\frac{\varepsilon \zeta}{\eta} E_x, \quad (3.44)$$

which is the Helmholtz-Smoluchowski plug flow velocity.

Essentially this means that the electric forces do not play a role in the bulk of the fluid, as the counter ions collect in the screening layer near the surface. Momentum balance for the bulk yields that

$$\rho_f i \omega v_x = \frac{\eta}{r} \frac{\partial}{\partial r} \left(r \frac{\partial v_x}{\partial r} \right), \quad (3.45)$$

or

$$0 = \left(\varpi^2 + \frac{\partial^2}{\partial r^2} + \frac{1}{r} \frac{\partial}{\partial r} \right) v_x. \quad (3.46)$$

The general solution to (3.46) is given by

$$v_x = A J_0(\varpi r), \quad (3.47)$$

with A some arbitrary constant.

Substitution of the imposed wall velocity as the boundary condition at $r = R_c$ yields that

$$A = -\frac{\varepsilon\zeta}{\eta} \frac{\hat{E}_x}{J_0(\varpi R_c)}, \quad (3.48)$$

so that

$$v_x = -\frac{\varepsilon\zeta}{\eta} \frac{J_0(\varpi r)}{J_0(\varpi R_c)} \hat{E}_x. \quad (3.49)$$

The volume flux Q_x is given by

$$Q_x = \int_0^{R_c} v_x 2\pi r dr = -\frac{2\pi\varepsilon\zeta \hat{E}_x}{\eta} \int_0^{R_c} \frac{J_0(\varpi r)}{J_0(\varpi R_c)} r dr. \quad (3.50)$$

Integrating (3.50) yields that

$$Q_x = -\frac{2\pi\varepsilon\zeta \hat{E}_x}{\eta\varpi} \frac{R_c J_1(\varpi R_c)}{J_0(\varpi R_c)}. \quad (3.51)$$

As we have that $\hat{I}_x = \sigma \hat{E}_x \pi R_c^2$, we can derive that

$$\frac{Q_x}{\hat{I}_x} = -\frac{\varepsilon\zeta}{\sigma\eta} \frac{2}{\varpi R_c} \frac{J_1(\varpi R_c)}{J_0(\varpi R_c)}. \quad (3.52)$$

Comparison of (3.52) with (3.28) shows that

$$\frac{Q_x}{\hat{I}_x} = \frac{\hat{E}_x}{\partial\hat{p}/\partial x}, \quad (3.53)$$

because it must be in accordance with the Onsager principle of reciprocity. For a parallel-plate channel configuration a similar approach can be used. Now 2.43 becomes

$$\frac{\partial^2 v_x}{\partial z^2} = \frac{\varepsilon E_x}{\eta} \frac{\partial^2 \Phi}{\partial z^2}, \quad (3.54)$$

which results in the same velocity profile as given in (3.43). Momentum balance for the bulk yields that

$$\rho_f i\omega v_x = \eta \frac{\partial^2 v_x}{\partial z^2}, \quad (3.55)$$

or

$$0 = \frac{\partial^2 v_x}{\partial z^2} - \mathfrak{w}^2 v_x. \quad (3.56)$$

The solution to (3.56), can be obtained if use is made of the imposed wall velocity as the boundary condition at $z = H$

$$v_x = A \cosh(\mathfrak{w}z), \quad (3.57)$$

where A is given by

$$A = \frac{\varepsilon\zeta}{\eta} \frac{\hat{E}_x}{\cosh(\mathfrak{w}H)}, \quad (3.58)$$

so that

$$v_x = \frac{\varepsilon\zeta}{\eta} \frac{\cosh(\mathfrak{w}z)}{\cosh(\mathfrak{w}H)} \hat{E}_x, \quad (3.59)$$

The volume flux Q_x is given by

$$Q_x = 2 \int_0^H v_x dz = \frac{2\varepsilon\zeta \hat{E}_x}{\eta} \int_0^H \frac{\cosh(\mathfrak{w}z)}{\cosh(\mathfrak{w}H)} dz. \quad (3.60)$$

Integrating (3.60) yields that the volume flux for a parallel-plate channel configuration becomes

$$Q_x = \frac{2\varepsilon\zeta \hat{E}_x}{\eta\mathfrak{w}} \tanh(\mathfrak{w}H). \quad (3.61)$$

Here we find that

$$\frac{Q_x}{\hat{I}_x} = \frac{\varepsilon\zeta}{\eta\sigma} \frac{1}{\mathfrak{w}H} \tanh(\mathfrak{w}H), \quad (3.62)$$

so that also in this case

$$\frac{Q_x}{\hat{I}_x} = \frac{\hat{E}_x}{\partial \hat{p} / \partial x}, \quad (3.63)$$

(see (3.32)) in accordance with the principle of reciprocity.

Table 3.2: Medium properties used for as input for analytical derivations. Use is made from KCl, as given by Haartsen and Pride (1996).

Property	Unit	Value	Dimension
Porosity	ϕ	0.15	[-]
DC permeability	k_0	$1.0 \cdot 10^{-12}$	[m ²]
Bulk modulus solid	K_s	36.0	[GPa]
Bulk modulus fluid	K_f	2.2	[GPa]
Frame bulk modulus	K_{fr}	9.0	[GPa]
Shear modulus	G	7.0	[GPa]
Fluid viscosity	η	$1.0 \cdot 10^{-3}$	[Pa/s]
Solid density	ρ_s	$2.7 \cdot 10^3$	[kg/m ³]
Fluid density	ρ_f	$1.0 \cdot 10^3$	[kg/m ³]
Salinity	c_q	$1 \cdot 10^{-3}$	[mol/l]
Temperature	T	298	[K]
Relative permittivity of fluid	ε_{rf}	80	[-]
Relative permittivity of solid	ε_{rs}	4	[-]
Relative magnetic permeability	μ_r	1	[H/m]
Tortuosity	α_∞	3	[-]

3.2 Sensitivity analysis

In Figures 3.12 to 3.16 we investigate the sensitivity of the dynamic permeability and the dynamic coupling coefficient on ρ_f , η , and the concentration c_q . Obviously, the latter is only investigated for electric coupling $\hat{C}(\omega)$, as it will have no effect on dynamic permeability. Only absolute values of the coupling coefficients are plotted. The input parameters are given in table 3.2. We notice that the dynamic permeability is not very sensitive as function of the density and viscosity; there is only clear change in rollover frequency ω/ω_c . For the dynamic coupling the same effects appear. The dependence on concentration is plotted in Figure 3.16. As expected, the salt concentration decisively affects the magnitude of the electrokinetic coupling coefficient and not the frequency part. For high concentrations, the coupling effect practically disappears.

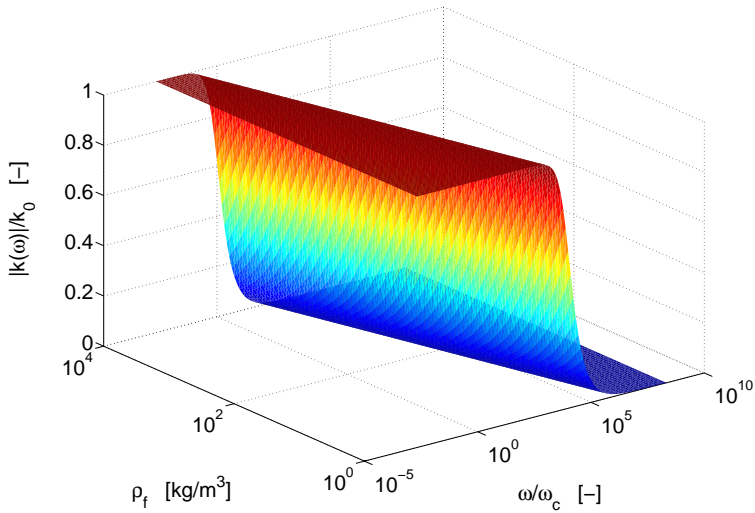


Figure 3.12: Dynamic permeability sensitivity for changes in ρ_f . Bulk properties used by Haartsen and Pride (1996), Table 3.2.

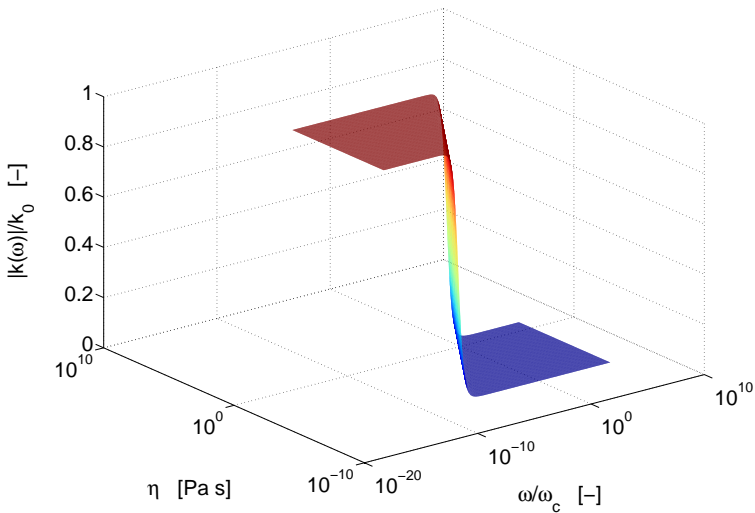


Figure 3.13: Dynamic permeability sensitivity for changes in η . Bulk properties used by Haartsen and Pride (1996), Table 3.2.

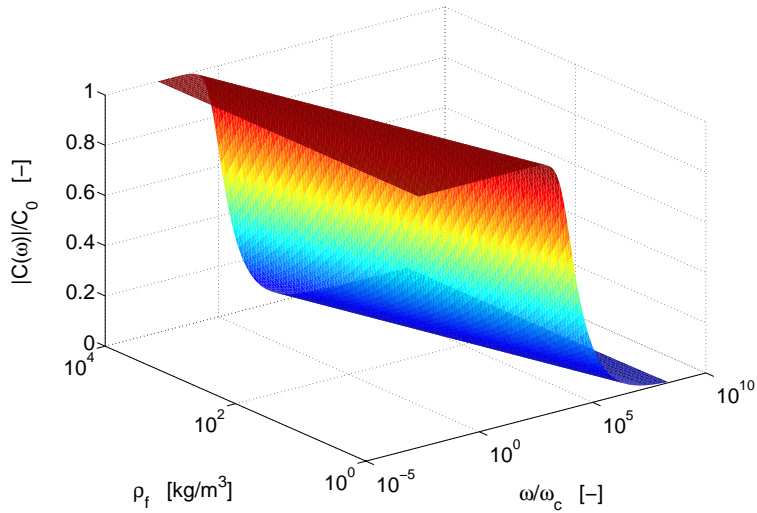


Figure 3.14: Dynamic EK coupling coefficient sensitivity for changes in ρ_f . Bulk properties used by Haartsen and Pride (1996), Table 3.2.

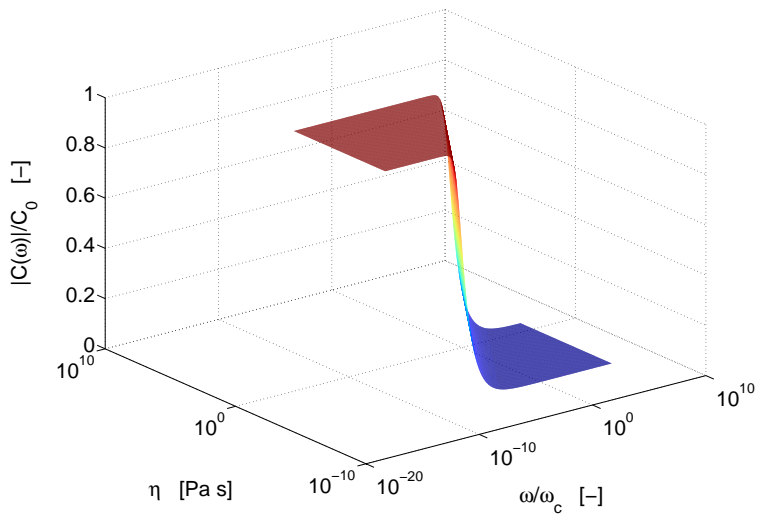


Figure 3.15: Dynamic EK coupling coefficient sensitivity for changes in η . Bulk properties used by Haartsen and Pride (1996), Table 3.2.

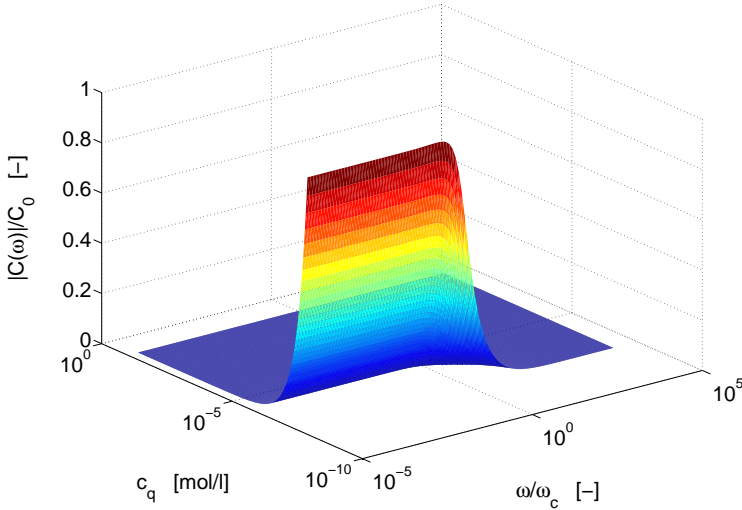


Figure 3.16: Dynamic EK coupling coefficient sensitivity for changes in c_q . Bulk properties used by Haartsen and Pride (1996), Table 3.2.

3.3 Onsager relationships

In this section the coupling coefficients will be described in a broader context. When a saturated porous material is subjected to hydraulic, potential, chemical or thermal gradients, equilibrium is disturbed. Denoting J_i as the material flow, and X_j as the actuating phenomenon, we write [Prigogine (1961)]

$$J_i = - \sum_j L_{ij} \nabla X_j, \quad (3.64)$$

with L_{ij} the phenomenological (also known as Onsager or transport) coefficients. The term phenomenological coefficients signifies that these coefficients are usually determined from experiments [Bader (2005); Masliyah and Bhattacharjee (2006)]. Onsager found out that there is an underlying symmetry for the phenomenological coefficients, also known as the Onsager reciprocal relation [Onsager (1931a,b)]:

$$L_{ij} = L_{ji}. \quad (3.65)$$

Several physical phenomena in natural and engineered systems are governed by transport processes. The derived equations (3.64) and (3.65) are known

as constitutive laws. Considering hydraulic, electric, chemical and thermal flow within we write that

$$\mathbf{v}_f = -L_{11}\nabla p - L_{12}\nabla\Phi - L_{13}\nabla\mu_c - L_{14}\nabla T, \quad (3.66)$$

$$\mathbf{J} = -L_{21}\nabla p - L_{22}\nabla\Phi - L_{23}\nabla\mu_c - L_{24}\nabla T, \quad (3.67)$$

$$\mathbf{J}_c = -L_{31}\nabla p - L_{32}\nabla\Phi - L_{33}\nabla\mu_c - L_{34}\nabla T, \quad (3.68)$$

$$\mathbf{Q}_T = -L_{41}\nabla p - L_{42}\nabla\Phi - L_{43}\nabla\mu_c - L_{44}\nabla T. \quad (3.69)$$

where μ_c is the chemical potential, \mathbf{J}_c the chemical diffusive flux, and \mathbf{Q}_T the heat flux. In the current research only a small part is investigated. Consider a fluid-saturated porous medium, without temperature and electrolyte concentration gradients. The transport equations can be expressed as

$$\mathbf{v}_f = -L_{11}\nabla p - L_{12}\nabla\Phi, \quad (3.70)$$

$$\mathbf{J} = -L_{12}\nabla p - L_{22}\nabla\Phi. \quad (3.71)$$

According to Saxen's law [Bader (2005), Molina et al. (1999)], if $J = 0$ the electric current density is zero we have

$$\frac{\nabla\Phi}{\nabla\hat{p}} = -\frac{L_{12}}{L_{22}}. \quad (3.72)$$

Applying Onsager's reciprocal relationship between cross-coupling coefficients we have that

$$\left(\frac{\mathbf{v}_f}{\mathbf{J}}\right)_{\nabla p=0} = -\left(\frac{\nabla\Phi}{\nabla\hat{p}}\right)_{\mathbf{J}=0}. \quad (3.73)$$

This was already experimentally shown in 1892 by Saxen. Expressing the fluid velocity in terms of the pressure gradient for the case $J = 0$ we find that

$$\frac{\mathbf{v}_f}{\nabla p} = \left(\frac{L_{12}^2 - L_{11}L_{22}}{L_{22}}\right). \quad (3.74)$$

It is also noticed that

$$\left(\frac{\mathbf{v}_f}{\nabla\Phi}\right)_{\mathbf{J}=0} = \left(\frac{\mathbf{J}}{\nabla p}\right)_{\mathbf{v}_f=0}. \quad (3.75)$$

This is a different way of formulating Saxen's law [Brunet and Ajdari (2006)], which is based on the Onsager relations. Any differences between the reciprocal phenomenological coefficients can usually be attributed to experimental

Table 3.3: Direct and coupled flow phenomena.

$J_i \backslash \nabla X_j$	Hydraulic	Electric	Chemical	Thermal
Fluid	Darcy's law	Electro osmosis	Chemical osmosis	Thermo osmosis
Charge	Streaming potential	Ohm's law	Dorn potential	Seebeck effect
Solute	Ultra filtration	Electrophoresis	Fick's law	Soret effect
Heat	Isothermal heat	Peltier effect	Dufour effect	Fourier's law

shortcomings [Bader (2005), Reppert and Morgan (2002)].

The types of coupled flow that can occur in a porous medium are listed in Table 3.3 [Bader (2005), Barragán et al. (2006), Heister (2005), Mitchell (1991), Moreno and Trevisan (1999)] known as Onsager's matrix. On the main diagonal, direct flow phenomena are given and coupled flow phenomena are found off-diagonally. All the fluxes on the main diagonal are induced by its conjugated driving force, while the off-diagonal terms are driven by forces of other types.

Chapter 4

Electrokinetic wave propagation

In this chapter the macroscopic governing equations are discussed, which describe the coupling between seismics and electromagnetics in fluid-saturated porous media. Use is made of the linearized equations as formulated by Pride (1994). The porous material is saturated with an electrolyte. The governing electrokinetic equations are the combined Biot (1956a,b) equations describing acoustics within porous media and the Maxwell equations for electromagnetic fields [Sommerfeld (1964)]. Biot describes wave propagation in porous materials within a system of two interpenetrating phases: the solid phase and the fluid phase. Both phases are described by the averaged motion of the solid and fluid parts using conservation of mass and momentum. Material properties are included through stress-strain relations. To obtain the electrokinetic governing equations the following assumptions are made:

- The entire fluid-solid system is considered to be isothermal.
- The deformation is completely reversible and linear elastic.
- Each volume element is described by the averaged displacement of the fluid \mathbf{u}_f and of the solid parts \mathbf{u}_s .
- The fluid-filled elastic skeleton has a statistical distribution of interconnected pores.
- The fluid is considered a Newtonian fluid.
- The fluid does not transmit nor react to a shear force in the solid.
- The wavelength is much larger than the grain or pore size.

We start with a general description of a poro-elastic material, which is fully fluid-saturated, for which the governing electrokinetic relationships are derived.

4.1 Electrokinetic relations

If we consider an elementary cube of porous material (porosity ϕ), the forces per unit bulk area applied to the solid portion of the cube faces are denoted $\boldsymbol{\tau}$

$$\boldsymbol{\tau} = -\boldsymbol{\sigma} - (1 - \phi)p\mathbf{I}, \quad (4.1)$$

with $\boldsymbol{\sigma}$ the intergranular stress and p the fluid pressure. The Kronecker delta δ_{ij} is required, because the pore fluid cannot sustain any shear forces. The normal force exerted on the fluid portion of the elementary bulk area is defined as

$$\xi = -\phi p. \quad (4.2)$$

The stress-strain relations for isotropic materials may be written as [Biot (1956a,b), Biot and Willis (1957), Gassmann (1951)]

$$\boldsymbol{\tau} = G(\mathbf{u}_s \nabla^T + \nabla) + [A \nabla \cdot \mathbf{u}_s + Q \nabla \cdot \mathbf{u}_f] \mathbf{I}, \quad (4.3)$$

$$\xi = Q \nabla \cdot \mathbf{u}_s + R \nabla \cdot \mathbf{u}_f, \quad (4.4)$$

where \mathbf{u}_s and \mathbf{u}_f are the solid and fluid displacement vectors, respectively. The coefficients A , Q and R can be expressed as a function of the porosity ϕ , the bulk modulus of the solid K_s , the bulk modulus of the fluid K_f , the bulk modulus of the porous drained matrix K_{fr} and the shear modulus G

$$A = \phi \frac{K_{fr}}{\phi_{eff}} - (1 - \phi) \frac{K_f}{\phi_{eff}} \left(1 - \phi - \frac{K_{fr}}{K_s} \right) - \frac{2}{3}G, \quad (4.5)$$

$$Q = \phi \frac{K_f}{\phi_{eff}} \left(1 - \phi - \frac{K_{fr}}{K_s} \right), \quad (4.6)$$

$$R = \phi^2 \frac{K_f}{\phi_{eff}}, \quad (4.7)$$

where $\phi_{eff} = \phi + \frac{K_f}{K_s} \left(1 - \phi - \frac{K_{fr}}{K_s} \right)$ is the effective porosity.

We will first consider the equations of motion without the electrokinetic effect. The equations of motion result from conservation of momentum for the fluid and the solid and are specified in their linearized form

$$\phi \rho_f \frac{\partial^2 \mathbf{u}_f}{\partial t^2} = \nabla \xi - \frac{\eta \phi}{k_0} F(t) * \frac{\partial \mathbf{w}}{\partial t} - (\alpha_\infty - 1) \rho_f \frac{\partial^2 \mathbf{w}}{\partial t^2}, \quad (4.8)$$

$$(1 - \phi) \rho_s \frac{\partial^2 \mathbf{u}_s}{\partial t^2} = \nabla \cdot \boldsymbol{\tau} + \frac{\eta \phi}{k_0} F(t) * \frac{\partial \mathbf{w}}{\partial t} + (\alpha_\infty - 1) \rho_f \frac{\partial^2 \mathbf{w}}{\partial t^2}, \quad (4.9)$$

where ρ_f is the fluid density, ρ_s the solid density, α_∞ is the tortuosity, η the fluid viscosity, k_0 the (static) permeability and $\mathbf{w} = \phi(\mathbf{u}_f - \mathbf{u}_s)$ the relative displacement. The $*$ symbol denotes convolution. The left-hand sides of both (4.8) and (4.9) contain the inertial terms. On the right-hand sides we recognize the surface forces (intergranular stress and pressure), the Darcy term, and added mass effects. Adopting an $e^{i\omega t}$ time dependence, the viscous correction factor is defined by Johnson et al. (1987) as

$$\hat{F}(\omega) = \sqrt{1 + m \frac{i\omega}{2\omega_c}}, \quad (4.10)$$

with $m = 8\alpha_\infty k_0 / (\phi \Lambda^2)$ the shape factor (usually taken 1), Λ the weighted pore volume-to-pore surface ratio [Johnson et al. (1987)], $\omega_c = (\eta\phi) / (\alpha_\infty \rho_f k_0)$ the characteristic (or rollover) frequency describing the transition from low-frequency viscosity dominated flow towards high-frequency inertia dominated flow.

Combining (4.8) and (4.9) with the stress-strain equations (4.3) and (4.4) yields that

$$G\nabla^2 \hat{\mathbf{u}}_s + (A + G)\nabla(\nabla \cdot \hat{\mathbf{u}}_s) + Q\nabla(\nabla \cdot \hat{\mathbf{u}}_f) = -\omega^2(\hat{\rho}_{11}\hat{\mathbf{u}}_s + \hat{\rho}_{12}\hat{\mathbf{u}}_f), \quad (4.11)$$

$$Q\nabla(\nabla \cdot \hat{\mathbf{u}}_s) + R\nabla(\nabla \cdot \hat{\mathbf{u}}_f) = -\omega^2(\hat{\rho}_{12}\hat{\mathbf{u}}_s + \hat{\rho}_{22}\hat{\mathbf{u}}_f), \quad (4.12)$$

where $\hat{\rho}_{11}(\omega)$, $\hat{\rho}_{12}(\omega)$, and $\hat{\rho}_{22}(\omega)$ are the so-called generalized effective density functions

$$\hat{\rho}_{11}(\omega) = (1 - \phi)\rho_s - \hat{\rho}_{12}(\omega), \quad (4.13)$$

$$\hat{\rho}_{12}(\omega) = \phi\rho_f \left[1 + i \frac{\eta\phi}{\omega\rho_f \hat{k}(\omega)} \right], \quad (4.14)$$

$$\hat{\rho}_{22}(\omega) = \phi\rho_f - \hat{\rho}_{12}(\omega). \quad (4.15)$$

The dynamic permeability is closely related to the viscous correction factor (see subsection 3.1.2)

$$\frac{\hat{k}(\omega)}{k_0} = \left(\hat{F}(\omega) + \frac{i\omega}{\omega_c} \right)^{-1}. \quad (4.16)$$

Following Schakel and Smeulders (2010) the electrokinetic effect can be included in (4.11) and (4.12). An electric field $\hat{\mathbf{E}}$ is imposed on a fluid-saturated porous material. As discussed in the previous chapter, the electric field exerts

an additional body force on the fluid electrolyte so that

$$\begin{aligned} G\nabla^2\hat{\mathbf{u}}_s + (A + G)\nabla(\nabla \cdot \hat{\mathbf{u}}_s) + Q\nabla(\nabla \cdot \hat{\mathbf{u}}_f) = \\ = -\omega^2(\hat{\rho}_{11}(\omega)\hat{\mathbf{u}}_s + \hat{\rho}_{12}(\omega)\hat{\mathbf{u}}_f) + \frac{\eta\phi\hat{L}(\omega)}{\hat{k}(\omega)}\hat{\mathbf{E}}, \end{aligned} \quad (4.17)$$

$$\begin{aligned} Q\nabla(\nabla \cdot \hat{\mathbf{u}}_s) + R\nabla(\nabla \cdot \hat{\mathbf{u}}_f) = \\ = -\omega^2(\hat{\rho}_{12}(\omega)\hat{\mathbf{u}}_s + \hat{\rho}_{22}(\omega)\hat{\mathbf{u}}_f) - \frac{\eta\phi\hat{L}(\omega)}{\hat{k}(\omega)}\hat{\mathbf{E}}, \end{aligned} \quad (4.18)$$

where $\hat{L}(\omega)$ is the dynamic electrokinetic coupling factor. Considering the definitions for $\hat{\rho}_{12}(\omega)$ and $\hat{\rho}_{22}(\omega)$, equation (4.18) can be written as

$$i\omega\hat{\mathbf{w}} = \frac{\hat{k}(\omega)}{\eta}(-\nabla\hat{p} + \omega^2\rho_f\hat{\mathbf{u}}_s) + \hat{L}(\omega)\hat{\mathbf{E}}. \quad (4.19)$$

Pride expanded Ohm's law in the sense that hydrodynamic flow also induces electric currents

$$\hat{\mathbf{J}} = \hat{L}(\omega)(-\nabla\hat{p} + \omega^2\rho_f\hat{\mathbf{u}}_s) + \hat{\sigma}(\omega)\hat{\mathbf{E}}, \quad (4.20)$$

where $\hat{\mathbf{J}}$ is the electric current density and $\hat{\sigma}(\omega)$ the dynamic conductivity (see Appendix B). We recognize that the electroseismic coupling is present both in the mechanical as well as in the electromagnetic equations (4.19) and (4.20) [Li et al. (1995)]. Eliminating $(-\nabla\hat{p} + \omega^2\rho_f\hat{\mathbf{u}}_s)$ from (4.19) and (4.20), we obtain

$$i\omega\hat{\mathbf{w}} = \hat{L}(\omega)\hat{\mathbf{E}} + \frac{\hat{k}(\omega)}{\eta\hat{L}(\omega)}(\hat{\mathbf{J}} - \hat{\sigma}(\omega)\hat{\mathbf{E}}). \quad (4.21)$$

The Maxwell relation for the magnetic field is given by Ampère's Circuit Law

$$\hat{\mathbf{J}} = \nabla \times \hat{\mathbf{H}} - \varepsilon i\omega\hat{\mathbf{E}}, \quad (4.22)$$

with $\hat{\mathbf{H}}$ the magnetic field and ε the electric permittivity. The electric permittivity for a fluid-saturated porous medium consists of a solid and fluid part

$$\varepsilon = \varepsilon_r\varepsilon_0 = \left[\frac{\phi}{\alpha_\infty}(\varepsilon_{rf} - \varepsilon_{rs}) + \varepsilon_{rs} \right] \varepsilon_0. \quad (4.23)$$

with ε_0 the electric permittivity in vacuum, ε_r the relative electric permittivity, ε_{rf} and ε_{rs} the fluid and solid dielectric constants respectively. Faraday's induction law states that

$$\mu i\omega\hat{\mathbf{H}} = -\nabla \times \hat{\mathbf{E}}, \quad (4.24)$$

with μ the magnetic permeability. Substitution of (4.22) in (4.21) results in

$$i\omega\hat{\mathbf{w}} = \hat{L}(\omega)\hat{\mathbf{E}} + \frac{\hat{k}(\omega)}{\eta\hat{L}(\omega)}(\nabla \times \mathbf{H} - [i\omega\varepsilon + \hat{\sigma}(\omega)]\hat{\mathbf{E}}). \quad (4.25)$$

Taking the cross product of Faraday's law (4.24), we obtain

$$\nabla \times \nabla \times \hat{\mathbf{E}} = -i\omega\mu\nabla \times \hat{\mathbf{H}}, \quad (4.26)$$

or

$$\nabla(\nabla \cdot \hat{\mathbf{E}}) - \nabla^2\hat{\mathbf{E}} = -i\omega\mu\nabla \times \hat{\mathbf{H}}. \quad (4.27)$$

Substitution of (4.27) in (4.21) yields that

$$\mu\hat{\varepsilon}(\omega)\omega^2\hat{\mathbf{E}} + \omega^2\frac{\eta\mu}{\hat{k}(\omega)}\hat{L}(\omega)\hat{\mathbf{w}} = \nabla(\nabla \cdot \hat{\mathbf{E}}) - \nabla^2\hat{\mathbf{E}}, \quad (4.28)$$

where $\hat{\varepsilon}(\omega)$ is the effective electric permittivity of the porous continuum

$$\hat{\varepsilon}(\omega) = \varepsilon - i\frac{\hat{\sigma}(\omega)}{\omega} + i\frac{\eta\hat{L}^2(\omega)}{\omega\hat{k}(\omega)}, \quad (4.29)$$

Equations (4.17), (4.18) and (4.28) form a closed set of equations for the fields $\hat{\mathbf{u}}_s$, $\hat{\mathbf{u}}_f$ and $\hat{\mathbf{E}}$.

4.2 Wave motion

In this section the governing electrokinetic equations in fluid saturated porous media are solved for a homogeneous isotropic whole space [Pride (1994), Pride and Haartsen (1996)]. Part of the analysis is performed in the frequency wavenumber domain. We use the $e^{-i\mathbf{k}\cdot\mathbf{x}}$ space-dependence, where \mathbf{x} is the three-dimensional position vector and \mathbf{k} is the three-dimensional wavenumber vector.

Helmholtz decomposition [Deresiewicz (1960)] allows us to write the displacement and electric vector fields as a superposition of longitudinal and transversal fields by introducing the potentials \wp and $\boldsymbol{\varsigma}$:

$$\mathbf{u}_s = \nabla\wp_s + \nabla \times \boldsymbol{\varsigma}_s, \quad (4.30)$$

$$\mathbf{u}_f = \nabla\wp_f + \nabla \times \boldsymbol{\varsigma}_f, \quad (4.31)$$

$$\mathbf{E} = \nabla\wp_E + \nabla \times \boldsymbol{\varsigma}_E. \quad (4.32)$$

Substituting (4.30) - (4.32) in the governing electrokinetic equations (4.17), (4.18) and (4.28), results in

$$\begin{aligned} & \nabla \left[(A + 2G)\nabla^2 \hat{\phi}_s + Q\nabla^2 \hat{\phi}_f + \hat{\rho}_{11}(\omega)\omega^2 \hat{\phi}_s + \hat{\rho}_{12}(\omega)\omega^2 \hat{\phi}_f - \frac{\eta\phi \hat{L}(\omega)}{\hat{k}(\omega)} \hat{\phi}_E \right] \\ & + \nabla \times \left[G\nabla^2 \hat{\zeta}_s + \hat{\rho}_{11}(\omega)\omega^2 \hat{\zeta}_s + \hat{\rho}_{12}(\omega)\omega^2 \hat{\zeta}_f - \frac{\eta\phi \hat{L}(\omega)}{\hat{k}(\omega)} \hat{\zeta}_E \right] = \mathbf{0}, \end{aligned} \quad (4.33)$$

$$\begin{aligned} & \nabla \left[Q\nabla^2 \hat{\phi}_s + R\nabla^2 \hat{\phi}_f + \hat{\rho}_{12}(\omega)\omega^2 \hat{\phi}_s + \hat{\rho}_{22}(\omega)\omega^2 \hat{\phi}_f + \frac{\eta\phi \hat{L}(\omega)}{\hat{k}(\omega)} \hat{\phi}_E \right] \\ & + \nabla \times \left[\hat{\rho}_{12}(\omega)\omega^2 \hat{\zeta}_s + \hat{\rho}_{22}(\omega)\omega^2 \hat{\zeta}_f + \frac{\eta\phi \hat{L}(\omega)}{\hat{k}(\omega)} \hat{\zeta}_E \right] = \mathbf{0}, \end{aligned} \quad (4.34)$$

and

$$\begin{aligned} & \nabla \left[-\omega^2 \frac{\eta\mu\phi}{\hat{k}(\omega)} \hat{L}(\omega) \hat{\phi}_s + \omega^2 \frac{\eta\mu\phi}{\hat{k}(\omega)} \hat{L}(\omega) \hat{\phi}_f + \mu\hat{\varepsilon}(\omega)\omega^2 \hat{\phi}_E \right] \\ & + \nabla \times \left[-\omega^2 \hat{L}(\omega) \left(\frac{\eta\mu\phi}{\hat{k}(\omega)} \hat{\zeta}_s - \frac{\eta\mu\phi}{\hat{k}(\omega)} \hat{\zeta}_f \right) + \mu\hat{\varepsilon}(\omega)\omega^2 \hat{\zeta}_E + \nabla^2 \hat{\zeta}_E \right] = \mathbf{0}. \end{aligned} \quad (4.35)$$

These equations are satisfied if the terms between the square brackets are equal to zero [Wisse (1999)].

4.2.1 Longitudinal waves

For the temporal Fourier transform of the potentials $\hat{\phi}$, which correspond to the compressional fields, we can now write

$$\begin{bmatrix} P & Q & 0 \\ Q & R & 0 \\ 0 & 0 & 0 \end{bmatrix} \begin{bmatrix} \nabla^2 \hat{\phi}_s \\ \nabla^2 \hat{\phi}_f \\ \nabla^2 \hat{\phi}_E \end{bmatrix} = \begin{bmatrix} -\hat{\rho}_{11} & -\hat{\rho}_{12} & \frac{\eta\phi}{\omega^2 \hat{k}} \hat{L} \\ -\hat{\rho}_{12} & -\hat{\rho}_{22} & -\frac{\eta\phi}{\omega^2 \hat{k}} \hat{L} \\ \frac{\eta\phi}{\omega^2 \hat{k}} \hat{L} & -\frac{\eta\phi}{\omega^2 \hat{k}} \hat{L} & -\frac{\hat{\varepsilon}}{\omega^2} \end{bmatrix} \omega^2 \begin{bmatrix} \hat{\phi}_s \\ \hat{\phi}_f \\ \hat{\phi}_E \end{bmatrix},$$

where $P = A + 2G$. Using the spatial Fourier transform we obtain

$$\begin{bmatrix} \hat{\rho}_{11}(\omega) - Ps^2 & \hat{\rho}_{12}(\omega) - Qs^2 & -\frac{\eta\phi}{\omega^2 \hat{k}(\omega)} \hat{L}(\omega) \\ \hat{\rho}_{12}(\omega) - Qs^2 & \hat{\rho}_{22}(\omega) - Rs^2 & \frac{\eta\phi}{\omega^2 \hat{k}(\omega)} \hat{L}(\omega) \\ -\frac{\eta\phi}{\omega^2 \hat{k}(\omega)} \hat{L}(\omega) & \frac{\eta\phi}{\omega^2 \hat{k}(\omega)} \hat{L}(\omega) & \frac{\hat{\varepsilon}(\omega)}{\omega^2} \end{bmatrix} \begin{bmatrix} \hat{\phi}_s \\ \hat{\phi}_f \\ \hat{\phi}_E \end{bmatrix} = \mathbf{0}, \quad (4.36)$$

with $s^2 = (\mathbf{k} \cdot \mathbf{k})/\omega^2$ the complex-valued squared slowness. It is possible to eliminate $\hat{\phi}_E$ from the first two equations so that

$$\begin{bmatrix} \hat{\rho}_{11}^E(\omega) - Ps^2 & \hat{\rho}_{12}^E(\omega) - Qs^2 & 0 \\ \hat{\rho}_{12}^E(\omega) - Qs^2 & \hat{\rho}_{22}^E(\omega) - Rs^2 & 0 \\ -\frac{\eta\phi}{\omega^2\hat{k}(\omega)}L(\omega) & \frac{\eta\phi}{\omega^2\hat{k}(\omega)}L(\omega) & \frac{\hat{\varepsilon}(\omega)}{\omega^2} \end{bmatrix} \begin{bmatrix} \hat{\phi}_s \\ \hat{\phi}_f \\ \hat{\phi}_E \end{bmatrix} = \mathbf{0}, \quad (4.37)$$

where $\hat{\rho}_{11}^E(\omega)$, $\hat{\rho}_{12}^E(\omega)$ and $\hat{\rho}_{22}^E(\omega)$ are the newly introduced effective electroviscous densities

$$\hat{\rho}_{11}^E(\omega) = \hat{\rho}_{11}(\omega) - \hat{\rho}^E(\omega), \quad (4.38)$$

$$\hat{\rho}_{12}^E(\omega) = \hat{\rho}_{12}(\omega) + \hat{\rho}^E(\omega), \quad (4.39)$$

$$\hat{\rho}_{22}^E(\omega) = \hat{\rho}_{22}(\omega) - \hat{\rho}^E(\omega), \quad (4.40)$$

$$\hat{\rho}^E(\omega) = \frac{\eta^2\phi^2\hat{L}^2(\omega)}{\hat{k}^2(\omega)\hat{\varepsilon}(\omega)\omega^2}. \quad (4.41)$$

We note that both viscous and electrokinetic coupling effects are now elegantly comprised in electroviscous densities. The first two equations (4.37) can be solved

$$\begin{bmatrix} \hat{\rho}_{11}^E(\omega) - Ps^2 & \hat{\rho}_{12}^E(\omega) - Qs^2 \\ \hat{\rho}_{12}^E(\omega) - Qs^2 & \hat{\rho}_{22}^E(\omega) - Rs^2 \end{bmatrix} \begin{bmatrix} \hat{\phi}_s \\ \hat{\phi}_f \end{bmatrix} = \mathbf{0}, \quad (4.42)$$

in the conventional way

$$s_{p1, p2}^2 = \frac{-\Delta \mp \sqrt{\Delta^2 - 4(PR - Q^2)(\hat{\rho}_{11}^E(\omega)\hat{\rho}_{22}^E(\omega) - (\hat{\rho}_{12}^E(\omega))^2)}}{2(PR - Q^2)}. \quad (4.43)$$

with

$$\Delta = -(P\hat{\rho}_{22}^E(\omega) + R\hat{\rho}_{11}^E(\omega) - 2Q\hat{\rho}_{12}^E(\omega)). \quad (4.44)$$

This approach was discussed earlier [Smeulders (2005)]. Here we only replace the original effective densities with the new electroviscous ones. The dispersion relations (4.37) not only predict the phase velocities and attenuations [see (4.43)], but also yield the fluid-solid amplitude ratios Γ and the strength of the electric field with respect to the solid's motion $\bar{\Gamma}$

$$\Gamma_{p1, p2} = \frac{\hat{\phi}_{f, p1, p2}}{\hat{\phi}_{s, p1, p2}} = \frac{\hat{\rho}_{11}^E(\omega) - Ps_{p1, p2}^2}{Qs_{p1, p2}^2 - \hat{\rho}_{12}^E(\omega)}, \quad (4.45)$$

$$\bar{\Gamma}_{p1, p2} = \frac{\hat{\phi}_{E, p1, p2}}{\hat{\phi}_{s, p1, p2}} = \frac{\eta\phi\hat{L}(\omega)}{\hat{k}(\omega)\hat{\varepsilon}(\omega)}(1 - \Gamma_{p1, p2}). \quad (4.46)$$

Low-frequency limit

For $\omega \ll \omega_c$, the square root in (4.43) can be replaced by the first order term of the Taylor series expansion, and hence we obtain

$$\lim_{\omega \ll \omega_c} s_{p_1, p_2}^2 = \frac{-\Delta \mp \Delta \left[1 - \frac{2(PR - Q^2)(\hat{\rho}_{22}^E(\omega)\hat{\rho}_{11}^E(\omega) - (\hat{\rho}_{22}^E(\omega))^2)}{\Delta^2} \right]}{2(PR - Q^2)}. \quad (4.47)$$

For the slow compressional wave we find that

$$\lim_{\omega \ll \omega_c} \frac{1}{s_{p_2}^2} = \lim_{\omega \ll \omega_c} \frac{PR - Q^2}{P\rho_2 + R\rho_1 - H\hat{\rho}_{12}^E(\omega)}, \quad (4.48)$$

where $H = P + R + 2Q$ is the Gassmann modulus, $\rho_1 = (1 - \phi)\rho_s$, and $\rho_2 = \phi\rho_f$. Evaluating $\hat{\rho}_{12}^E(\omega)$, we have that

$$\lim_{\omega \ll \omega_c} \frac{1}{s_{p_2}^2} = \frac{i\omega(PR - Q^2)}{b_0 H \left(1 - \frac{\eta L_0^2}{(\eta L_0^2 - \sigma_0 k_0)} \right)}, \quad (4.49)$$

with $\sigma_0 = \phi\sigma_f/\alpha_\infty$ the adjusted fluid conductivity. This solution shows that the slow wave is described by a diffusion equation rather than a wave equation, in the low-frequency limit, because the solution (4.49) satisfies the diffusion equation

$$D_h \nabla^2 \Upsilon = i\omega \Upsilon, \quad (4.50)$$

where Υ can be any relevant variable (u , p , etc) and

$$D_h = \frac{PR - Q^2}{b_0 H \left(1 - \frac{\eta L_0^2}{(\eta L_0^2 - \sigma_0 k_0)} \right)}. \quad (4.51)$$

We note that this expression for D_h is similar to the one originally derived by Biot (1956a) apart from the correction term $1 - \eta L_0^2/(\eta L_0^2 - \sigma_0 k_0)$ associated with the electrokinetic coupling effect.

For the fast wave we can write

$$\lim_{\omega \ll \omega_c} \frac{1}{s_{p_1}^2} = \frac{P\rho_2 + R\rho_1 - H\hat{\rho}_{12}^E(\omega)}{\rho_1\rho_2 - \rho\hat{\rho}_{12}^E(\omega)} = \frac{H}{\rho}, \quad (4.52)$$

where $\rho = \hat{\rho}_{11}^E(\omega) + \hat{\rho}_{22}^E(\omega) + 2\hat{\rho}_{12}^E(\omega)$. The effective modulus H was originally derived by Gassmann (1951) in an article that predates the Biot theory, and

therefore this limit is often called the Biot-Gassmann result.

It can be seen that the electrokinetic coupling does not influence this limit with respect to the purely acoustic wave. This is due to the fact that in the low-frequency limit of the fast wave the relative motion of the fluid with respect to that of the solid is negligible so that no electrokinetic effect is generated.

High-frequency limit

In the high-frequency limit the dynamic effective densities $\hat{\rho}_{11}^E(\omega)$, $\hat{\rho}_{22}^E(\omega)$ and $\hat{\rho}_{12}^E(\omega)$ tend to

$$\rho_{11} = (1 - \phi)\rho_s - \rho_{12}, \quad (4.53)$$

$$\rho_{12} = -(\alpha_\infty - 1)\phi\rho_f, \quad (4.54)$$

$$\rho_{22} = \phi\rho_f - \rho_{12}, \quad (4.55)$$

respectively, so that the dispersion equation will become real-valued. Consequently both compressional waves become propagatory and no electrokinetic effects are left. But this of course is outside of the theoretical limits.

4.2.2 Transversal waves

In a similar way the transversal fields can be studied. From (4.33) - (4.35) the following matrix form is obtained for the transversal field potentials

$$\begin{bmatrix} G & 0 & 0 \\ 0 & 0 & 0 \\ 0 & 0 & 1 \end{bmatrix} \begin{bmatrix} \nabla^2 \hat{\xi}_s \\ \nabla^2 \hat{\xi}_f \\ \nabla^2 \hat{\xi}_E \end{bmatrix} = \begin{bmatrix} -\hat{\rho}_{11} & -\hat{\rho}_{12} & \frac{\eta\phi\hat{L}}{\omega^2\hat{k}} \\ -\hat{\rho}_{12} & -\hat{\rho}_{22} & -\frac{\eta\phi\hat{L}}{\omega^2\hat{k}} \\ \frac{\eta\mu\phi}{\hat{k}}\hat{L} & -\frac{\eta\mu\phi}{\hat{k}}\hat{L} & -\mu\hat{\varepsilon} \end{bmatrix} \omega^2 \begin{bmatrix} \hat{\xi}_s \\ \hat{\xi}_f \\ \hat{\xi}_E \end{bmatrix}.$$

Application of the spatial Fourier transform results in

$$\begin{bmatrix} \hat{\rho}_{11}(\omega) - Gs^2 & \hat{\rho}_{12}(\omega) & -\frac{\eta\phi\hat{L}(\omega)}{\omega^2\hat{k}(\omega)} \\ \hat{\rho}_{12}(\omega) & \hat{\rho}_{22}(\omega) & \frac{\eta\phi\hat{L}(\omega)}{\omega^2\hat{k}(\omega)} \\ -\frac{\eta\mu\phi}{\hat{k}(\omega)}\hat{L}(\omega) & \frac{\eta\mu\phi}{\hat{k}(\omega)}\hat{L}(\omega) & \mu\hat{\varepsilon} - s^2 \end{bmatrix} \begin{bmatrix} \hat{\xi}_s \\ \hat{\xi}_f \\ \hat{\xi}_E \end{bmatrix} = \mathbf{0}. \quad (4.56)$$

By adding the first two equations $\hat{\zeta}_f$ is simply eliminated from the first equation

$$\begin{bmatrix} \rho_1 - Gs^2 & \rho_2 & 0 \\ \hat{\rho}_{12}(\omega) & \hat{\rho}_{22}(\omega) & \frac{\eta\phi\hat{L}(\omega)}{\omega^2\hat{k}(\omega)} \\ -\frac{\eta\mu\phi}{\hat{k}(\omega)}\hat{L}(\omega) & \frac{\eta\mu\phi}{\hat{k}(\omega)}\hat{L}(\omega) & \mu\hat{\varepsilon} - s^2 \end{bmatrix} \begin{bmatrix} \hat{\zeta}_s \\ \hat{\zeta}_f \\ \hat{\zeta}_E \end{bmatrix} = \mathbf{0}. \quad (4.57)$$

From the first equation we simply derive that $\hat{\zeta}_f = \hat{\zeta}_s(Gs^2 - \rho_1)/\rho_2$. Substitution in the second and third equations yields that

$$\begin{bmatrix} \hat{\rho}_{12}(\omega) + \hat{\rho}_{22}(\omega)\frac{Gs^2 - \rho_1}{\rho_2} & -\frac{\eta\phi\hat{L}(\omega)}{\omega^2\hat{k}(\omega)} \\ \frac{\eta\phi\hat{L}(\omega)}{\omega^2\hat{k}(\omega)}\frac{Gs^2 - \rho_1}{\rho_2} & \mu\hat{\varepsilon} - s^2 \end{bmatrix} \begin{bmatrix} \hat{\zeta}_s \\ \hat{\zeta}_E \end{bmatrix} = \mathbf{0}. \quad (4.58)$$

Setting the determinant of this set equal to zero, we obtain the following dispersion relation

$$B_1s^4 + B_2s^2 + B_3 = 0, \quad (4.59)$$

where

$$B_1 = G\hat{\rho}_{22}(\omega), \quad (4.60)$$

$$B_2 = -G\mu\hat{\varepsilon}(\omega)\hat{\rho}_{22}^E(\omega) - (\hat{\rho}_{11}(\omega)\hat{\rho}_{22}(\omega) - (\hat{\rho}_{12}(\omega))^2), \quad (4.61)$$

$$B_3 = \mu\hat{\varepsilon}(\omega)[\hat{\rho}_{11}^E(\omega)\hat{\rho}_{22}^E(\omega) - (\hat{\rho}_{12}^E(\omega))^2]. \quad (4.62)$$

These relations were also given by Schakel and Smeulders (2010). Dividing all equations by $\hat{\rho}_{22}(\omega)$, we obtain alternatively

$$B_1 = G, \quad (4.63)$$

$$B_2 = -\left[\rho_t + G\mu\hat{\varepsilon}(\omega)\left(1 + \frac{\hat{L}^2(\omega)\hat{\rho}_{22}(\omega)}{\hat{\varepsilon}(\omega)\phi^2}\right)\right], \quad (4.64)$$

$$B_3 = \mu\hat{\varepsilon}(\omega)\left[\rho_t + \frac{\hat{L}^2(\omega)\hat{\rho}_{22}(\omega)}{\hat{\varepsilon}(\omega)\phi^2}\rho\right], \quad (4.65)$$

which are the expressions by Pride and Haartsen (1996) we remark that

$$\rho_t = \frac{\hat{\rho}_{11}(\omega)\hat{\rho}_{22}(\omega) - (\hat{\rho}_{12}(\omega))^2}{\hat{\rho}_{22}(\omega)}. \quad (4.66)$$

The dispersion relation (4.59) can be solved in a straight forward way. We find that there are two attenuated transversal fields, the conventional shear field and an E-M field, respectively. An example will be discussed in the next section.

Setting the electrokinetic coupling coefficient \hat{L} to zero will result in a shear wave and an uncoupled E-M wave as derived by Pride and Haartsen (1996)

$$s_{sh}^2 = \frac{\hat{\rho}_{11}(\omega)\hat{\rho}_{22}(\omega) - (\hat{\rho}_{12}(\omega))^2}{G\hat{\rho}_{22}(\omega)}, \quad (4.67)$$

$$s_{EM}^2 = \mu\hat{\epsilon}(\omega). \quad (4.68)$$

The dispersion relation (4.59) also yields the fluid-solid amplitude ratios and the strength of the electric field

$$\Gamma_{sh, EM} = \frac{\hat{\mathbf{S}}_{f, sh, EM}}{\hat{\mathbf{S}}_{s, sh, EM}} = \frac{Gs_{sh, EM}^2 - (1 - \phi)\rho_s}{\phi\rho_f}, \quad (4.69)$$

$$\bar{\Gamma}_{sh, EM} = \frac{\hat{\mathbf{S}}_{E, sh, EM}}{\hat{\mathbf{S}}_{f, sh, EM}} = \frac{\mu\eta\phi\hat{L}(\omega)}{\hat{k}(\omega) [\mu\hat{\epsilon}(\omega) - s_{sh, EM}^2]} (1 - \Gamma_{sh, EM}). \quad (4.70)$$

Low-frequency limit

For $\omega \ll \omega_c$ we note that

$$\lim_{\omega \ll \omega_c} \frac{\hat{L}^2(\omega)\hat{\rho}_{22}(\omega)}{\hat{\epsilon}(\omega)\phi^2} = \frac{\eta L_0^2}{\sigma_0 k_0 - \eta L_0^2}, \quad (4.71)$$

$$\lim_{\omega \ll \omega_c} \rho_t = \rho. \quad (4.72)$$

We thus find that

$$\lim_{\omega \ll \omega_c} \frac{1}{s_{sh}^2} = -\frac{B_2}{B_3} = \left[\frac{G\mu\epsilon_0 \left(1 + \frac{\eta L_0^2}{\sigma_0 k_0 - \eta L_0^2} \right)}{\rho\mu\epsilon_0 \left(1 + \frac{\eta L_0^2}{\sigma_0 k_0 - \eta L_0^2} \right)} \right] = \frac{G}{\rho}, \quad (4.73)$$

which is fully identical to the original Biot solution. For the EM wave, we find that

$$\lim_{\omega \ll \omega_c} \frac{1}{s_{EM}^2} = -\frac{B_1}{B_2} = \frac{G}{G\mu\epsilon_0 \left(1 + \frac{\eta L_0^2}{\sigma_0 k_0 - \eta L_0^2} \right)} = \frac{i\omega}{\mu\sigma_0}, \quad (4.74)$$

This shows that the EM wave is described by a diffusion equation rather than a wave equation, in the low-frequency limit, because the solution (4.74) satisfies the diffusion equation

$$D_h \nabla^2 \Upsilon = i\omega \Upsilon, \quad (4.75)$$

with

$$D_h = \frac{1}{\mu\sigma_0}. \quad (4.76)$$

High-frequency limit

For $\omega \rightarrow \infty$, the dynamic effective densities $\hat{\rho}_{11}(\omega)$, $\hat{\rho}_{22}(\omega)$ and $\hat{\rho}_{12}(\omega)$ tend to ρ_{11} , ρ_{22} and ρ_{12} . The parameters B_i now become

$$\lim_{\omega \rightarrow \infty} B_1 = G\rho_{22}, \quad (4.77)$$

$$\lim_{\omega \rightarrow \infty} B_2 = -[\rho_{11}\rho_{22} - \rho_{12}^2] - [G\mu\varepsilon\rho_{22}], \quad (4.78)$$

$$\lim_{\omega \rightarrow \infty} B_3 = \mu\varepsilon[\rho_{11}\rho_{22} - \rho_{12}^2]. \quad (4.79)$$

Both transversal waves become propagatory.

4.2.3 Numerical results

In this section numerical results are shown. Use is made of a data set given by Haartsen and Pride (1996). The input parameters are listed in Table 3.2. The phase velocity $\hat{v}(\omega)$, the attenuation coefficient $\alpha_Q(\omega)$ and the specific attenuation Q^{-1} are determined from the complex slownesses

$$\hat{v}(\omega) = \frac{1}{\text{Re}(s_a)}, \quad (4.80)$$

$$\alpha_Q(\omega) = \omega \text{Im}(s_a), \quad (4.81)$$

$$Q^{-1}(\omega) = 2 \left| \frac{\text{Im}(s_a)}{\text{Re}(s_a)} \right|, \quad (4.82)$$

with $a = p_1, p_2, s, EM$.

The results are plotted in Figures 4.1 to 4.3. We note that apart from the original three Biot waves (fast and slow compressional, and shear wave) a fourth field is predicted. This is an EM field, which is diffusive at low frequencies, and propagatory at high frequencies (this is however well above the maximum frequency under which the Biot part of the theory is valid). In

this respect, it resembles the slow compressional wave as we can see in Figure 4.1.

The fast compressional wave and the shear wave are almost frequency independent. In the slow compressional wave a crossover can be seen between viscosity-dominated flow and inertia-dominated flow [Charlaix et al. (1988)]. In Figures 4.4, 4.5, 4.6 and 4.7 the fluid-solid amplitude ratios, as given in (4.45), (4.46), (4.69) and (4.70), are shown. There is hardly any difference between presence and absence of the electrokinetic effect.

It is interesting that such crossover can also be distinguished for the EM wave, but at significantly higher frequency (higher than ω_c). This crossover frequency is defined as the ratio of the total fluid's electric conductivity versus the electric permittivity

$$\omega_{EM} = \frac{\sigma_0}{\varepsilon}. \quad (4.83)$$

Both crossover frequencies are indicated in Figures 4.1 to 4.3.

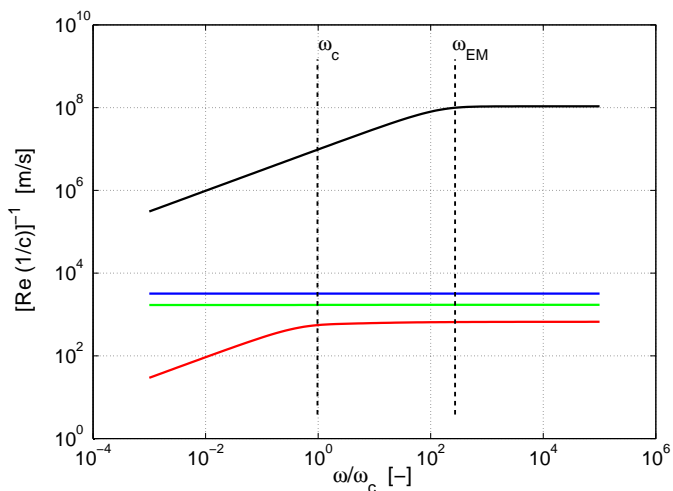


Figure 4.1: Phase speed for the E-M wave, fast wave, shear wave and slow wave for the data set in Table 3.2. The solid curves indicate the characteristic waves without coupling between acoustic and E-M phenomena, and the dashed curves indicate the coupling between them. — the slow compressional wave, — the shear wave, — the fast compressional wave, — the EM wave.

We also computed the wave characteristics for $L = 0$, i.e. without electrokinetic coupling. On the scale of the Figures, no difference can be distinguished. In the attenuation plots, we observe the characteristic diffusion behaviour

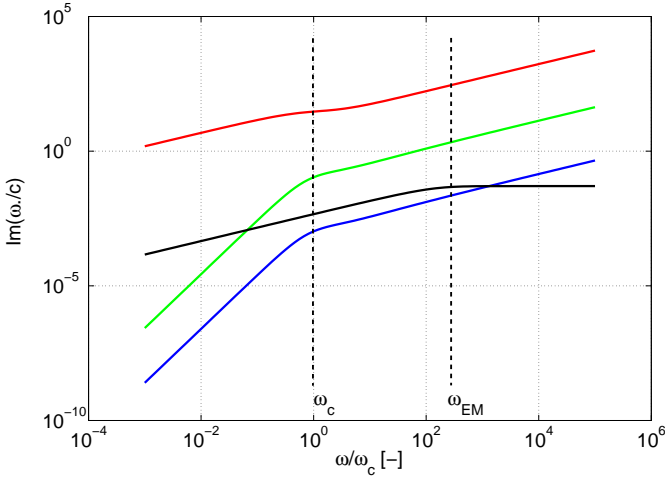


Figure 4.2: The attenuation of the slow wave, shear wave, fast wave and E-M wave for the data set in Table 3.2. The solid curves indicate the characteristic waves without coupling between acoustic and E-M phenomena, and the dashed curves indicate the coupling between them. — the slow compressional wave, — the shear wave, — the fast compressional wave, — the EM wave.

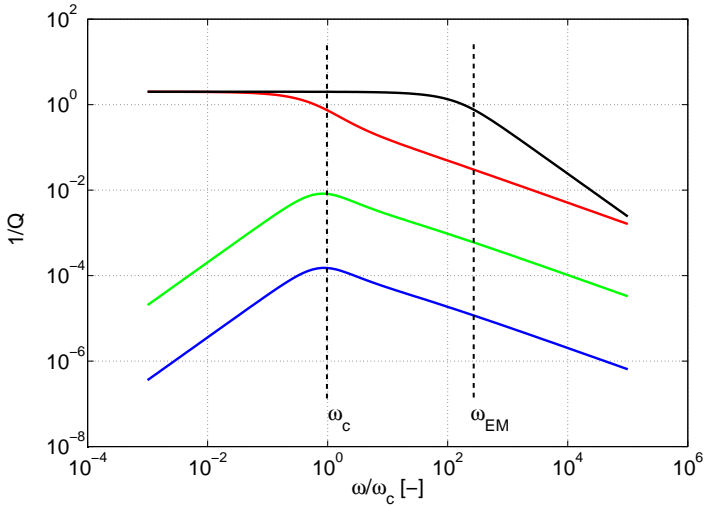


Figure 4.3: The specific attenuation for the slow wave, shear wave, fast wave and E-M wave for data set given in Table 3.2. The solid curves indicate the characteristic waves without coupling between acoustic and E-M phenomena, and the dashed curves indicate the coupling between them. — the slow compressional wave, — the shear wave, — the fast compressional wave, — the EM wave.

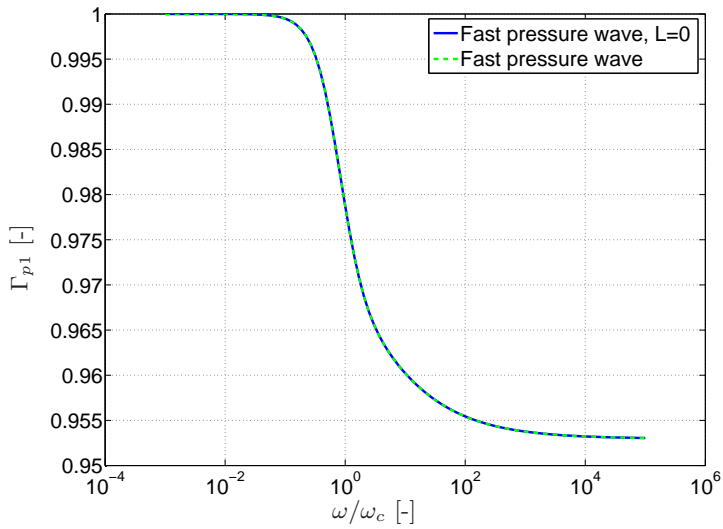


Figure 4.4: Compressional wave fluid-to-solid amplitude ratios presence and absence of the electrokinetic coupling.

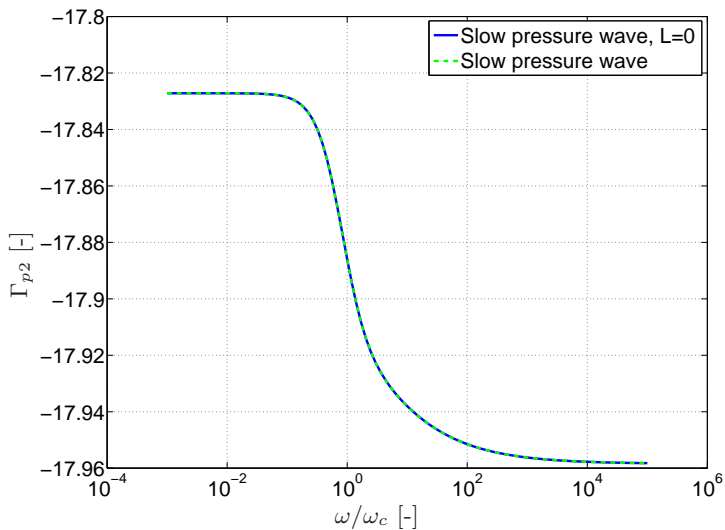


Figure 4.5: Compressional wave fluid-to-solid amplitude ratios presence and absence of the electrokinetic coupling.

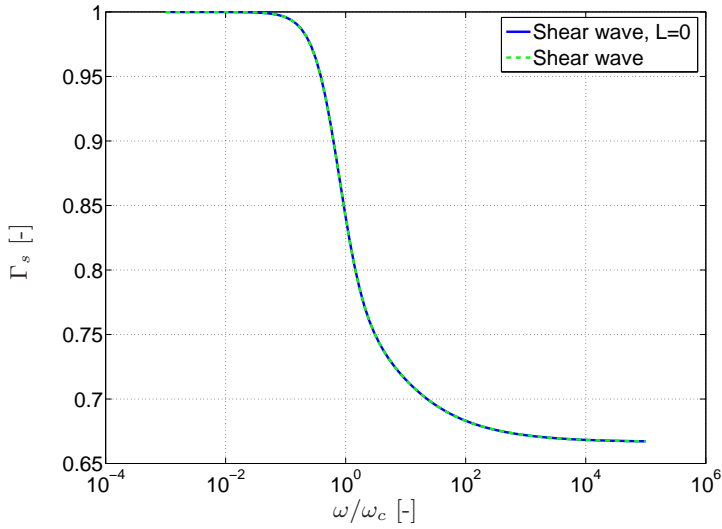


Figure 4.6: Shear and E-M wave fluid-to-solid amplitude ratios without and with electrokinetic coupling.

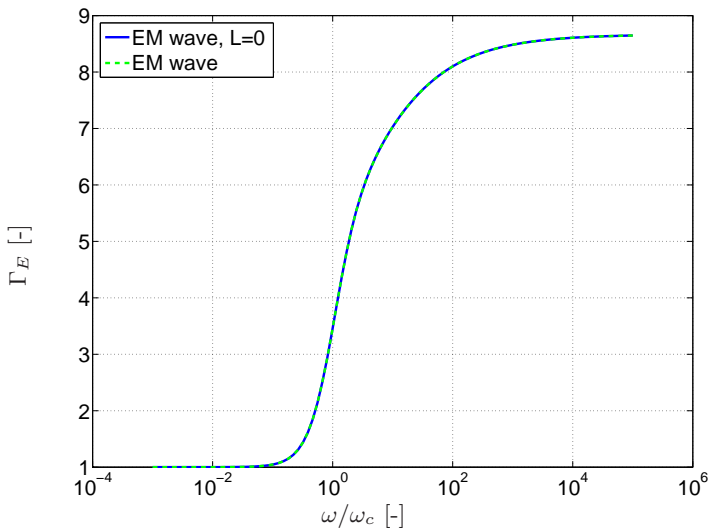


Figure 4.7: Shear and E-M wave fluid-to-solid amplitude ratios without and with electrokinetic coupling.

proportional to $\sqrt{\omega}$ for the slow compressional-wave and the EM wave, at low frequencies. The attenuation of the fast compressional-wave and the shear wave is described by a ω^2 dependency, at low frequencies, and by an $\sqrt{\omega}$ dependency, at high frequencies. Interestingly, the EM wave has limiting attenuation, at high frequencies. The specific attenuation is a measure for the attenuation over one wave length. It is inversely proportional to the quality factor Q . The higher the attenuation, the poorer the quality factor. As both the slow compressional and E-M waves have identical frequency-dependent behaviour for phase velocity and damping factor, at low frequencies, their specific attenuation becomes frequency independent in the low frequency domain.

4.3 Electrokinetic coupling effect

We have seen that at first glance, the effect of the electrokinetic coupling is not overwhelmingly large. To analyze this in more detail, we plot the relative attenuation of the fast and slow wave as function of the salinity for a fixed frequency. We notice that the attenuation of the fast compressional wave is decreased by EK effects, and that the attenuation of the slow compressional wave is decreased. Moreover there is a distinct concentration where these effects are largest. These effects can be explained as follows. For the fast compressional wave, the fluid and skeleton motions are in-phase. The excess counter-ions in the diffuse-double layer move tangentially to the solid surface in the electric double layer. The displacement of counter-ions generates a convection current. In the low fluid pressure regions the counter-ions accumulate while in the high fluid pressure area they are depleted. This creates an electric field. This electric field drives a conduction current, which balances the convection current. The electric field opposes the pressure gradient, thus reducing the amount of relative flow. So the fast compressional wave is slightly influenced by electrokinetic effects, creating a lower attenuation [Pride and Haartsen (1996), Reppert et al. (2001)]. For the slow compressional wave, fluid and solid motion are out-of-phase. Enhanced fluid pressures are generated by a frame contraction while regions of decreased fluid pressure are generated by frame expansion. High fluid pressure regions have an accumulation of counter charge and the low fluid pressure regions have a depletion of charge. The fluid pressure gradients creates fluid flow which reduces the charge separations. So for the slow compressional wave the electric field enhances the fluid flow resulting in a larger contribution of the viscous effect. Therefore the slow compressional wave as seen in Fi-

Table 4.1: Optimal compressional attenuation values for computed frequencies and salt concentrations.

Parameter	Unit	Value	Dimension
Slow wave max. attenuation	$\alpha_Q(L)/\alpha_Q(L=0)$	1.06	[-]
Fast wave min. attenuation	$\alpha_Q(L)/\alpha_Q(L=0)$	0.92	[-]
Slow wave frequency	ω_{p2}/ω_c	$3 \cdot 10^{-2}$	[-]
Fast wave frequency	ω_{p1}/ω_c	$3 \cdot 10^{-3}$	[-]
Slow wave salinity	c_{qp2}	$3 \cdot 10^{-8}$	[mol/l]
Fast wave salinity	c_{qp1}	$3 \cdot 10^{-8}$	[mol/l]

figure 4.8 has a stronger attenuation [Pride and Haartsen (1996)]. In Figure 4.9, we focus on the frequency-dependence for the concentration that causes maximum effects ($c_q \cong 3 \cdot 10^{-8}$ mol/l). The dependence on salinity is explained as follows. The width as well as the excess charge content of the diffuse double layer increase when the salinity decreases (also the conductivity will decrease). The amount of charge separation will increase as the salinity decreases, which will result in an increased attenuation for the slow compressional wave and a decreased attenuation for the fast compressional wave. At a certain decrease in salinity, the surface conduction will become important and the magnitude of the charge separation decreases.

For high frequencies, where inertial effects become dominant over viscous effects the above effects disappear completely. For low frequencies, the effect is maximized, for the fast compressional wave. Note that there is an additional damping of the fast wave ($\alpha > 1$) in a small frequency band. This is probably due to the flow distribution in the pores. At some frequencies, complicated flow and counterflow regions exist, so that the net effect increases the amount of relative flow, thus enhancing the viscous attenuation. For the slow compressional wave maximum attenuation is attained at $\omega/\omega_c \cong 0.03$. For even lower frequencies, the effect is mitigated somewhat. The difference between the slow and fast compressional wave attenuation maxima (see figure 4.8) is caused by the tortuosity. Setting the tortuosity equal to one ($\alpha_\infty = 1$), will result in an equal salinity for the maximum of the slow compressional and the fast compressional waves.

The minimum and maximum of the attenuation ratio $\alpha_Q(L)/\alpha_Q(L=0)$ are shown in Table 4.1. All effects are comprised in Figure 4.10.

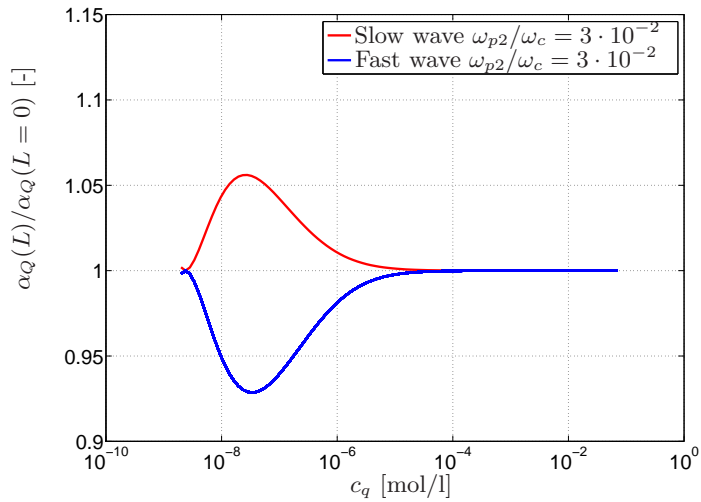


Figure 4.8: The effect of the electrokinetic coupling coefficient \hat{L} on the compressional wave attenuation coefficients as a function of the salinity of the saturated electrolyte. The upper curve is the slow compressional wave and the lower the fast compressional wave.

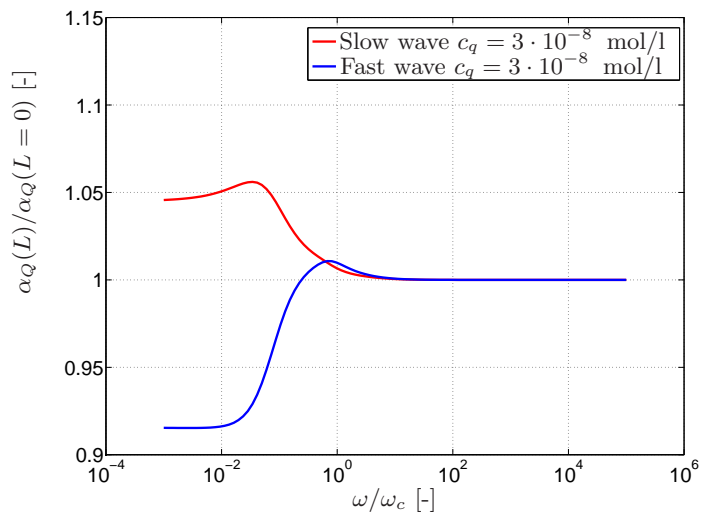


Figure 4.9: The effect of the electrokinetic coupling coefficient \hat{L} on the compressional wave attenuation coefficients as a function of the frequency of the saturated electrolyte. The upper curve is the slow compressional wave and the lower the fast compressional wave.

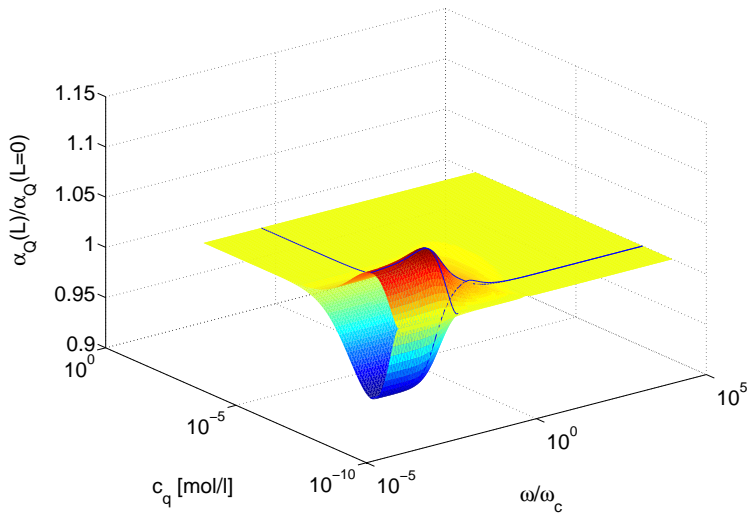


Figure 4.10: The effect of the electrokinetic coupling coefficient \hat{L} on the compressional wave attenuation coefficients as a function of the frequency and the salinity of the saturated electrolyte. The upper curve is the slow compressional wave and the lower the fast compressional wave. Parameters obtained from the data set given in Table 3.2. The surface lines, at constant frequency ($\omega_{p2}/\omega_c = 3 \cdot 10^{-2}$) and for constant molarity ($c_q = 3 \cdot 10^{-8}$ mol/l), are considered as cross-section.

Chapter 5

Experimental results

In this chapter the experimental set-up and the measured transport coefficients is discussed. For the experiments, use has been made of artificially constructed porous materials. The set-up is capable of measuring dynamic permeability and electrokinetic coupling coefficients.

5.1 Dynamic Darcy Cell

In order to measure the dynamic transport coefficients, use is made of the experimental setup described by Smeulders (1992) and Kelder (1998). It is called the Dynamic Darcy Cell (**DDC**) and is shown in Figures 5.1 and 5.2. It consists of a stainless steel cylinder where an oscillating pressure is applied at the bottom. The outer diameter of the cylinder is $d_{DDC} = 18.9$ cm and the height is $L_{DDC} = 36.3$ cm. It is an ideal platform to obtain amplitude and phase shift values (1-D datasets) for specific frequency values. A vibration exciter (**GW V20**), controlled by a power amplifier, drives a rubber membrane, which induces an oscillating pressure in a frequency range between 5 Hz to 600 Hz. As the wavelength is much larger than any characteristic length scale of the sample, the flow may be considered as incompressible. Two identical piezo-electric transducers (**Druck PCB 116A**) are used to measure the pressure drop across the sample. The lower pressure sensor is mounted in the steel cylinder wall, just below the sample. The other sensor is installed in a probe that is mounted just above the sample. Above and below the porous medium, electrodes are installed to measure the streaming potential gradient. Two sorts of electrodes are used alternatively. One option is to mount highly porous disks (Monel Ni-Cu **GKN Sinter Metals, SIKA-R 200**, 7 mm thick) at the top and bottom of the sample to record the voltages. We also used simple wire Ag/AgCl electrodes (**A-M systems**)

that were installed in the side wall above and below the sample. Only the tip of the electrode was in contact with the fluid (see Figure 5.1).

The signals from the two piezoelectric transducers are modified by means of amplifiers (**Kistler 5011**). Four samples are used, which can be seen in Table 5.1. For the connections with peripheral equipment, use has been made of screened-wires [Long and Rivers (1975)]. Effective noise reduction

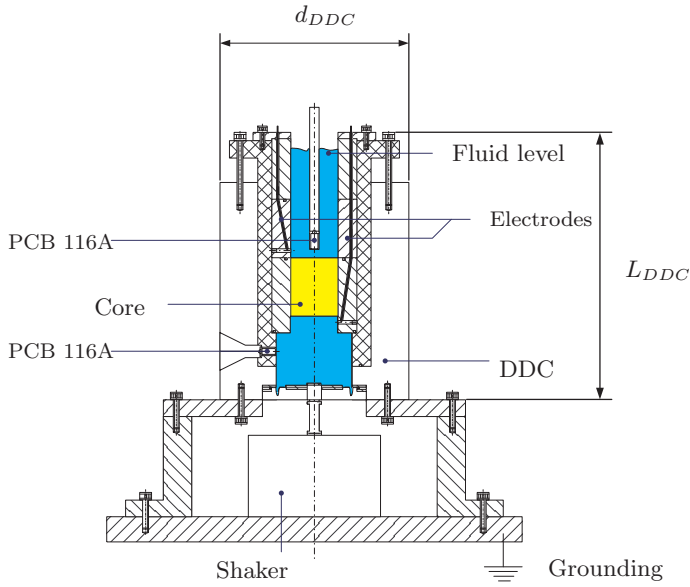


Figure 5.1: Schematic of the Dynamic Darcy Cell with quartz core sample and Ag/AgCl electrodes.

in the recorded signal is obtained by signal averaging. To avoid cross-over, every measurement is repeated twice at each frequency, to measure either the pressure gradient or the potential gradient. The electrodes are directly connected to the oscilloscope. The wall of the DDC consists of different coaxial sections (see Figure 5.1). The inner section is made out of perspex, so that electric shortcut is impaired. The entire set-up is grounded by means of earth wiring [Long and Rivers (1975)]. Use is made of a **DL9140 Yokogawa** digital oscilloscope. It is capable of measuring frequencies from 10 Hz up to 1 GHz with an accuracy of $\pm 0.01\%$. A National Instruments **NI PCI-GPIB IEEE 488.2** interface is used to connect the **HP 33120A** Function/Arbitrary waveform generator to the data logging PC. The function generator can modulate a sine-function with a range from 100 μHz up to 15 MHz. Within National Instruments **Labview Version 7.1** the measured

data from the oscilloscope as well as the reference signal from the function generator are accumulated.

The fluid conductivity and temperature are measured using a **WTW LF 340** apparatus. The pH values are measured using a **Metrohm 744 pH meter**.

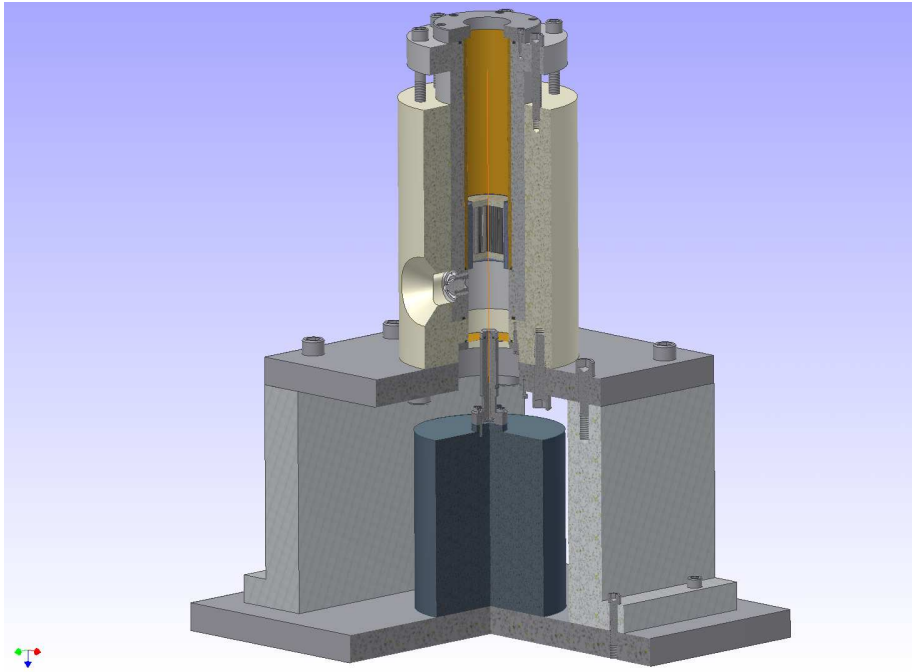


Figure 5.2: 3D view of Dynamic Darcy Cell. The shaker is visible in the lower part of the set-up (dark blue cylinder) as well as the sample in the middle of the gray cylindrical section in the upper part of the set-up.

5.2 Sample preparation and treatment

Four samples are used, two sintered glass cores (made of borosilicate) and two capillary cores, of which one is made of quartz and the other one of borosilicate with Monel disks (see Figures 5.3a and 5.4a). The cylinders are glued together using an epoxy resin. Sample QC consists of 127 cylinders made of quartz. Sample MSC is similar to sample QC, but it is equipped with permeable Monel disks (see Figure 5.3b and 5.4b) on top and bottom of the cylinders. Within the MSC sample, borosilicate cylinders are used (BSC sample). The Monel plates were also analyzed separately (sample MC

consisting of two Monel disks 5.05 cm apart).

Sample GC1 is made from two identical disk shaped porous glass filter plates

Table 5.1: Parameter values of the samples: QC=Quartz Core 2, MC=Monel disks without sample Core, BSC=Borosilicate Core, MSC=Borosilicate Core sandwiched between Monel disks, GC1=Glass Core 1, GC2=Glass Core 2. d_1 =outer cylinder radius, d_2 =capillary radius, n_1 =number of cylinders, n_2 =number of capillaries per cylinder, ϕ = porosity, k_0 =permeability, α_∞ =tortuosity (* determined using measurements), f_c =critical frequency.

Parameters	QC	MC	BSC	MSC	GC1	GC2
d_1 [mm]	3.2 ± 0.06	–	6.34 ± 0.03	6.34 ± 0.03	–	–
d_2 [mm]	0.5 ± 0.05	–	0.97 ± 0.04	0.97 ± 0.04	–	–
n_1 [–]	127	–	37	37	–	–
n_2 [–]	4	–	4	4	–	–
ϕ [%]	6.7 ± 0.5	50 ± 4	6.8 ± 0.6	9.3 ± 0.6	30 ± 4	24 ± 3
k_0 [Darcy]	522 ± 40	89 ± 12	2001 ± 110	205 ± 10	40 ± 6	77 ± 7
α_∞ [–]	1	$2 \pm 0.2^*$	1	$1.8 \pm 0.2^*$	2.6 ± 0.1	2.3 ± 0.1
f_c [Hz]	18.3	399.5	4.8	35.8	410.3	192.8

on top of each other (see Figure 5.5a) glued in a plastic holder. Sample GC2 also consists of two different identical disk shaped porous glass filter plates, but the holder is slightly different in the sense that an additional rubber sleeve is used (see Figure 5.5b) between the sample and the holder.

An overview of the samples is given in Table 5.1. The sample saturation proceeds as follows. Special attention is paid to avoid the presence of air bubbles during this operation. From degassed demineralized water, different salt solutions are prepared. The sample is carefully evacuated and saturated with such a salt solution. The set-up is left for 1 day, until a relative chemical equilibrium is reached, i.e. until the pH and the conductivity remain relatively constant, over time (laboratory environment will pollute sample over time).

Next, the dynamic pressure and voltage are measured over a wide frequency range. After the experiment, the set-up is cleaned, disassembled and dried. Also the sample is cleaned, dried, and inspected for integrity. Next the assembly is reinstalled, filled with a new salt solution and new dynamic measurements are performed.

5.3 Dynamic pressure measurements

The aim is to come up with an expression for the dynamic permeability using the two recorded pressures above and below the sample. In Figure 5.6, a schematic of the set-up is given [Smeulders (1992), Kelder (1998), Cortis

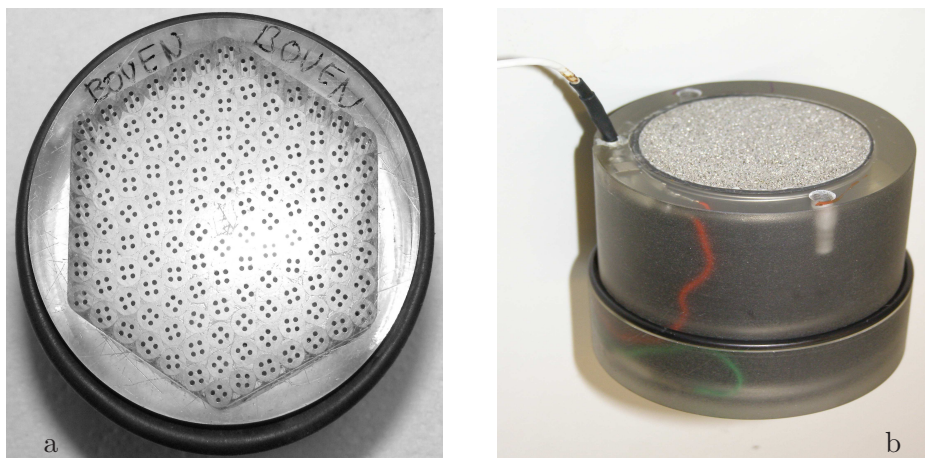


Figure 5.3: Photographs of QC (a) and MSC (b). The MSC internal core also consists of capillaries. Note the green and red wires inside the sample wall which are connected to the Monel disks above and below the core.

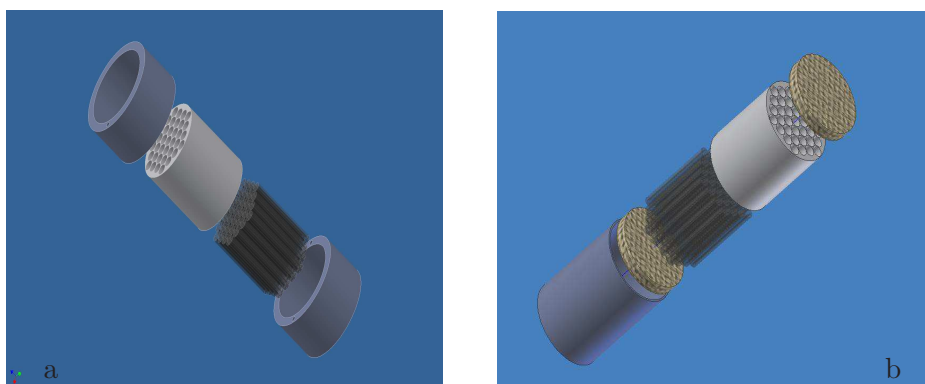


Figure 5.4: Exploded views of samples QC (a) and MSC (b). Note the Monel disks below and above the MSC sample.

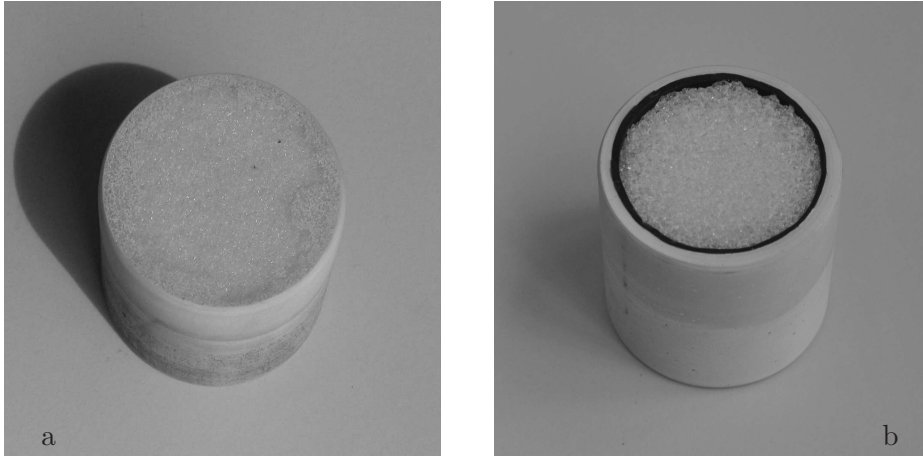


Figure 5.5: (a) Glass beads core 1 (GC1). (b) Glass beads core 2 (GC2).

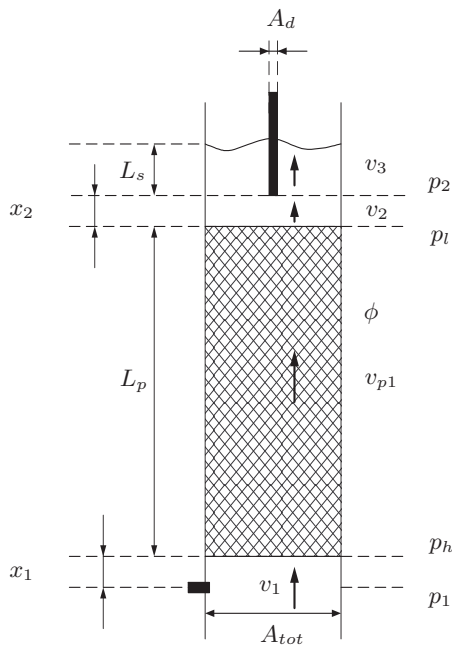


Figure 5.6: Schematic of the set-up. The sample has porosity ϕ and length L_p . Pressure sensors are placed at distances x_1 and x_2 from the sample lower and upper ends. The upper sensor has a cross-sectional area A_d . L_s is the length of the pressure probe in water.

(2002)]. The momentum equation for the fluid below the sample is written as

$$\frac{p_1 - p_h}{x_1} = -i\omega\rho_f v_1, \quad (5.1)$$

and momentum conservation above the sample yields that

$$\frac{p_l - p_2}{x_2} = -i\omega\rho_f v_2. \quad (5.2)$$

The fluid velocity v_3 can be related to the recorded pressure p_2

$$\frac{p_2 - 0}{L_s} = -i\omega\rho_f v_3, \quad (5.3)$$

Continuity of fluid flux yields that

$$\phi v_{p1} = v_1, \quad (5.4)$$

$$v_2 = v_1, \quad (5.5)$$

$$\gamma v_3 = v_2, \quad (5.6)$$

where $\gamma = (A_{tot} - A_d)/A_{tot}$ is the area ratio that compensates for the presence of the probe. Combination of (5.1), (5.2) and (5.5) leads to

$$p_h = p_1 + \frac{x_1}{x_2}(p_2 - p_l), \quad (5.7)$$

for the pressure directly under the sample. We combine (5.2), (5.3), and (5.6) to obtain the pressure amplitude p_l

$$p_l = p_2 \left(1 + \frac{\gamma x_2}{L_s} \right), \quad (5.8)$$

Substitution of (5.8) in (5.7) leads to the pressure amplitude right under the sample

$$p_h = p_1 - \frac{\gamma x_1}{L_s} p_2. \quad (5.9)$$

The dynamic permeability $\hat{k}(\omega)$ is defined by

$$\phi v_{p1} = \frac{\hat{k}(\omega)}{\eta} \frac{p_h - p_l}{L_p}. \quad (5.10)$$

Combining (5.10) with (5.3) - (5.6) and (5.8) and (5.9), we find that

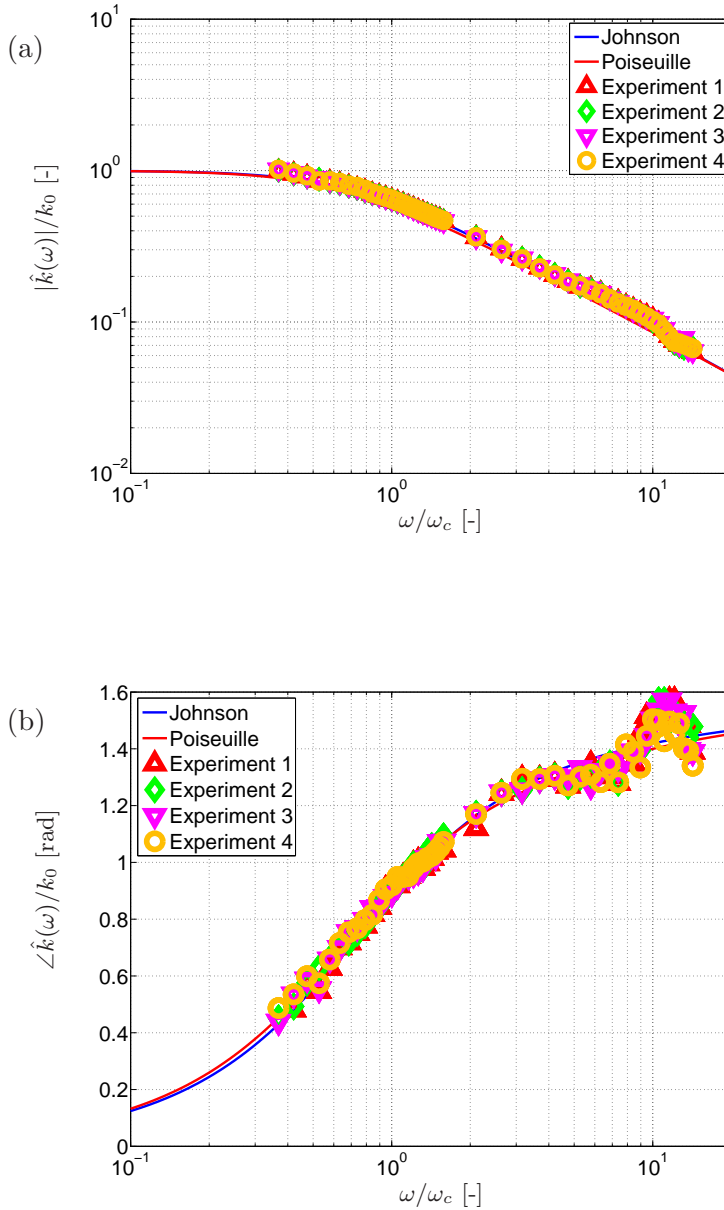


Figure 5.7: (a) Absolute and (b) phase values of the dynamic permeability for the QC sample. Johnson and Poiseuille versus measurements. Experiments 1-4 denote repeated experiments at different times.

$$\hat{k}(\omega) = \frac{iL_p}{L_s} \frac{\eta\gamma}{\rho_f\omega} \left[\frac{p_1}{p_2} - \left(1 + \frac{\gamma}{L_s}(x_1 + x_2) \right) \right]^{-1}, \quad (5.11)$$

where L_p is the sample length.

Figures 5.7a and 5.7b show the measurements of both the absolute and phase values of the dynamic permeability. The experimental data show good agreement with the theory described in Chapter 3. Figures 5.7a and 5.7b show some discrepancy between theory and measurement in the high frequency range (a maximum offset of 19%, for the magnitude and a maximum offset of 7% for the phase). Below the high frequency range as well Johnson's as Poiseuille's theory are applicable. This caused by the relative small differences between the both theories and the uncertainties in the measurements. These are due to low signal-to-noise ratio and set-up resonances above the $\omega/\omega_c = 4$.

5.4 Dynamic coupling coefficient measurements

Introducing $\hat{C}(\omega)$ as the cross coupling-coefficient [Molina et al. (1999), Neishtadt et al. (2006), Reppert et al. (2001)]. The aim is to come up with an expression for the cross coupling-coefficient using the recorded voltages and pressures above and below the sample. The extended Ohm's law (4.20) for an open-circuit configuration (no short-circuit, i.e., $\hat{J} = 0$) becomes

$$\hat{C}(\omega) = \frac{\hat{L}(\omega)}{\hat{\sigma}(\omega)} = -\frac{\nabla\hat{\Phi}}{\nabla\hat{p}} = -\frac{\Phi_1 - \Phi_2}{p_h - p_l}. \quad (5.12)$$

Substituting (5.8) and (5.9) and setting $\Phi_1 = 0$ (grounded connector), we have that

$$\hat{C}(\omega) = \Phi_2 \left[p_2 \left(1 + \frac{\gamma}{L_s}(x_1 + x_2) \right) - p_1 \right]^{-1}. \quad (5.13)$$

The potential difference measurements are performed using Ag/AgCl electrodes. The experiments are performed using a 0.13 ± 0.02 mmol/l sodium chloride solution.

Figures 5.8a and 5.8b show the dynamic coupling coefficient of the sample QC. The experimental data show good agreement (a maximum offset of 25%, for the magnitude and a maximum offset of 23% for the phase) with Pride's and Packard's theory. Most measurements (except for the higher frequencies with offset) are located between Pride's and Packard's theory. So both theoretical models can be used during following analysis. As in the dynamic

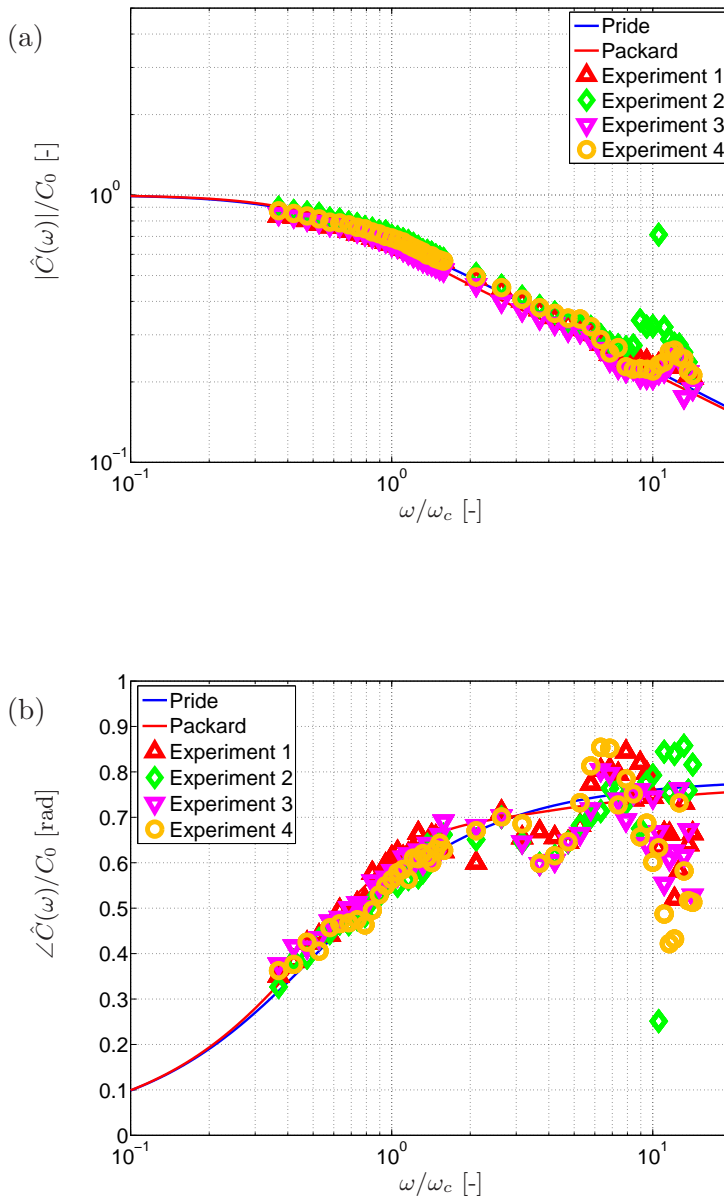


Figure 5.8: (a) Absolute and (b) phase values of the dynamic coupling for the QC sample. Pride and Packard versus measurements. Experiments 1-4 denote repeated experiments at different times.

permeability experiments, set-up resonances can be noticed in the high frequency region. The experiments were repeated four times (over a period of 4 to 5 days, without taking the set-up apart).

5.4.1 Concentration effects

Next, we investigate the influence of electrolyte concentrations. According to Thompson et al. (2007), lower concentrations (higher resistivity) favor signal strength. In Table 5.2 the specifications of the used NaCl concentrations are given. The dependence on concentration can be explained as follows. Both the width and the excess-charge content of the diffuse-double layers decrease with increasing salinity while the conductivity increases. Thus as the concentration grows the amount of charge separation decreases. So with increasing concentration, the magnitude becomes smaller, and the phase is unaffected [Pride and Haartsen (1996)]. These trends are clearly visible in the experimental results indeed (Figures 5.9a and 5.9b).

Table 5.2: Electrolyte specifications.

pH [-]	4.9 ± 0.3	5.0 ± 0.4	5.3 ± 0.3	5.6 ± 0.2
T [$^{\circ}C$]	23.0 ± 2	23.0 ± 2	22.7 ± 2	23.4 ± 2
c_q [mmol/l]	0.08 ± 0.03	0.13 ± 0.02	0.4 ± 0.02	0.8 ± 0.03
L_0 [$m^2s^{-1}V^{-1}$]	$1.5 \cdot 10^{-9}$	$1.5 \cdot 10^{-9}$	$1.2 \cdot 10^{-9}$	$1.0 \cdot 10^{-9}$

5.4.2 Other electrolytes

Table 5.3: Specification of the influence of several different electrolytes.

Salt	NaCl	KCl	KI	NaI
pH [-]	5.0 ± 0.4	5.2 ± 0.5	4.8 ± 0.2	5.0 ± 0.2
T [$^{\circ}C$]	23.0 ± 2	23.2 ± 2	22.9 ± 2	22.6 ± 3
c_q [mmol/l]	0.13 ± 0.02	0.16 ± 0.02	0.15 ± 0.03	0.15 ± 0.02
L_0 [$m^2s^{-1}V^{-1}$]	$1.5 \cdot 10^{-9}$	$1.5 \cdot 10^{-9}$	$1.3 \cdot 10^{-9}$	$1.4 \cdot 10^{-9}$

Next, we performed measurements with different electrolytes. An overview of the specification is given in Table 5.3. In the figures 5.10a and 5.10b the measured results are shown. There is good agreement between the NaCl

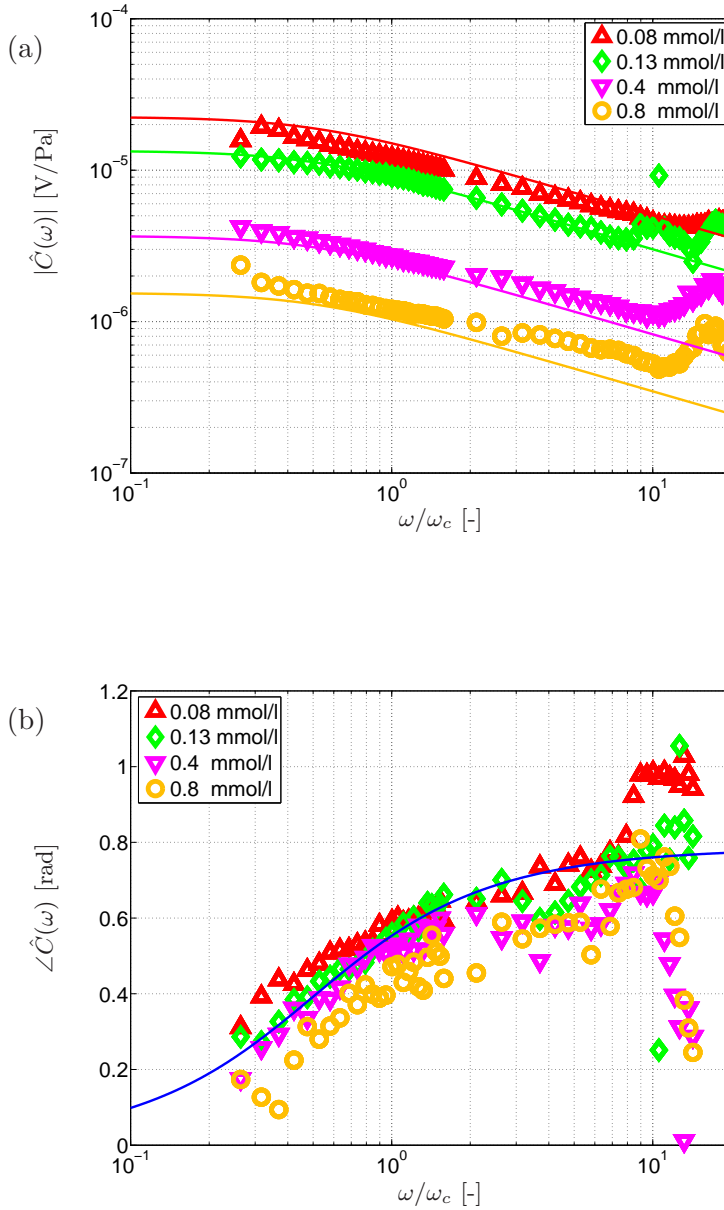


Figure 5.9: (a) Absolute and (b) phase values of the dynamic coupling for different NaCl concentrations for QC sample. Measurements for different concentrations, versus Pride theory. The solid curves (with like colours) represent theoretical results.

measurement and theory. For the KCl, KI, NaI there is a qualitative agreement, but quantitative there are magnitude differences, probably because of strong influences of the ζ -potentials (empirical), see figure 2.2. There are relative large discrepancies between different measured zeta potential measurements. Instead of the empirical relationship given by Pride and Morgan (2.2), a slightly adjusted version has been used for the NaCl measurements (2.3). So for KCl another slightly adjusted version of the zeta potential will be required. The phase values are rather scattered, but still there is a clear trend.

5.5 Electrode disks

Next we conducted experiments for the MSC samples using NaCl with $c_q = 0.11$ mmol/l. The specifications of the MSC sample are given in Table 5.1. An accurate correlation between theory (Johnson model and Pride model) and measurements can be seen for the absolute values Figure 5.11a up to 5.12b, the offsets in the lower frequency range are caused by limitations of the used equipment, while in the high frequency area this difference mainly is caused by resonance of the set-up (in comparison to the capillary system without plates, due to the additional Monel disks, the system is more sensitive for low eigenfrequencies). The measured phase signal of the coupling coefficient is not in agreement with the theoretical model due to the relative low permeability of the applied sample structure, especially the two Monel plates disturb the flow. Another drawback of this set-up is that it has the possibility to function as a capacitor [Reppert et al. (2001)].

5.6 Sintered glass beads

We also tested two samples made of sintered glass beads (GC1 and GC2). We notice that our measurements are clearly in the low-frequency range ($\omega < \omega_c$), as there is no rollover behaviour visible. We also notice that there are some anomalies visible resembling oscillatory behaviour (see Figure 5.13).

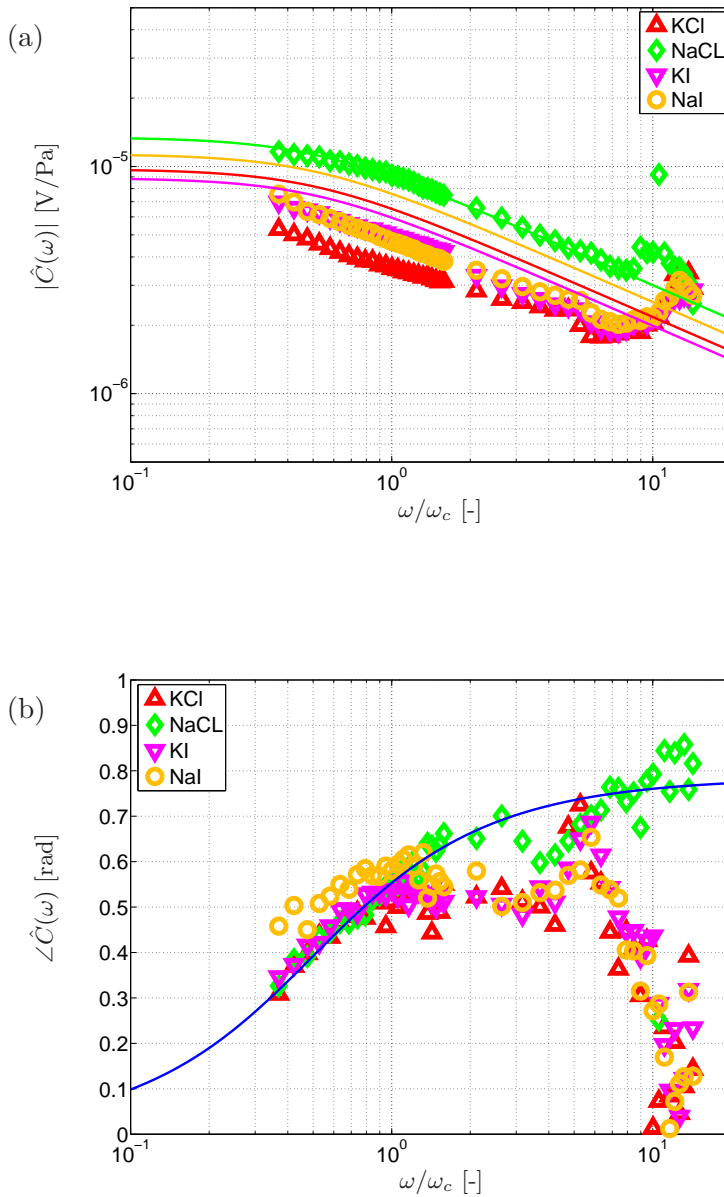


Figure 5.10: (a) Absolute and (b) phase values of dynamic coupling for the QC sample for different types of salt. Measurements for different sorts of salts, versus Pride theory. The solid curves (with like colours) represent theoretical results.

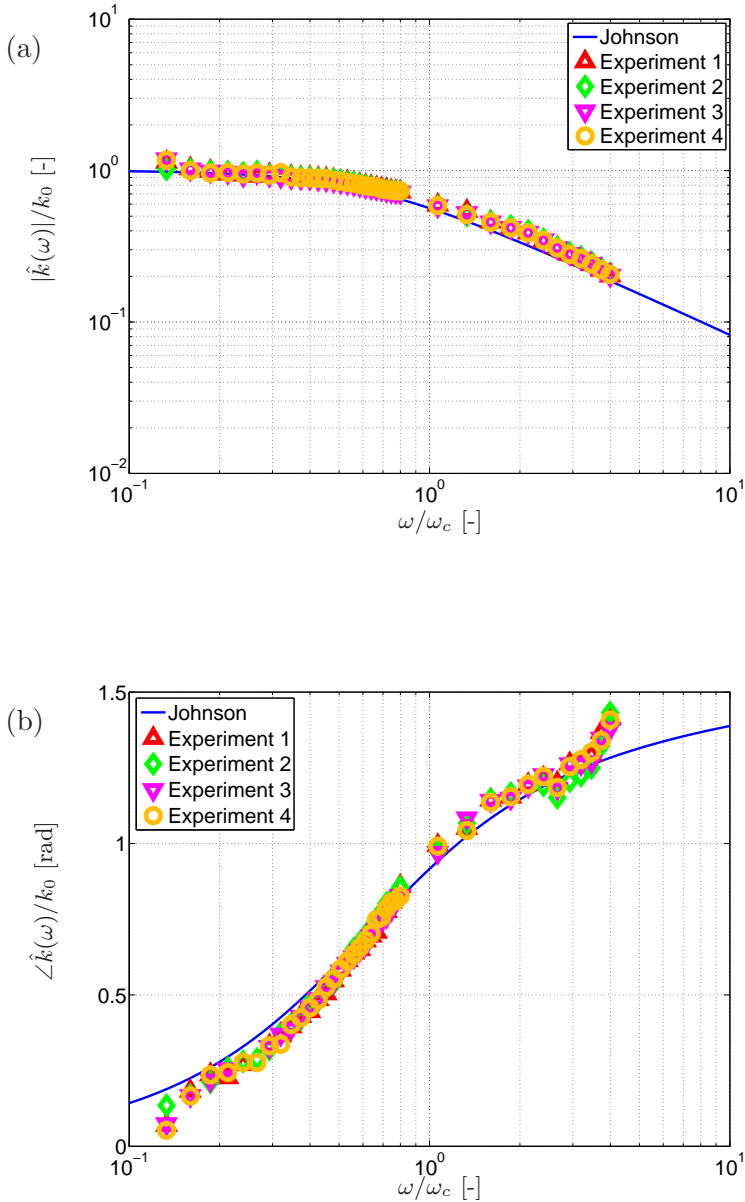


Figure 5.11: (a) Absolute and (b) phase values of the dynamic permeability for the MSC sample. Theory of Johnson, versus measurements, for shape factor $m = 1.75$. Experiments 1-4 denote repeated experiments at different times.

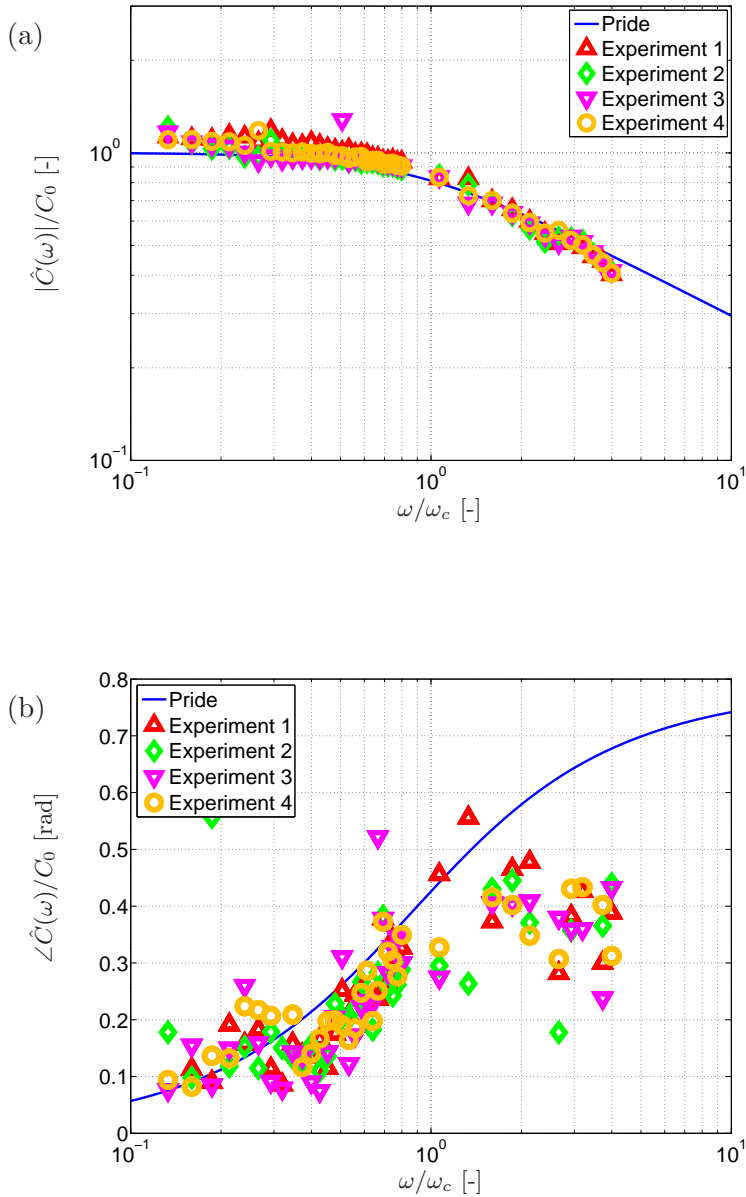


Figure 5.12: (a) Absolute and (b) phase values of the dynamic coupling coefficient for the MSC sample. Theory of Pride, versus measurements, for shape factor $m = 1.75$. Experiments 1-4 denote repeated experiments at different times.

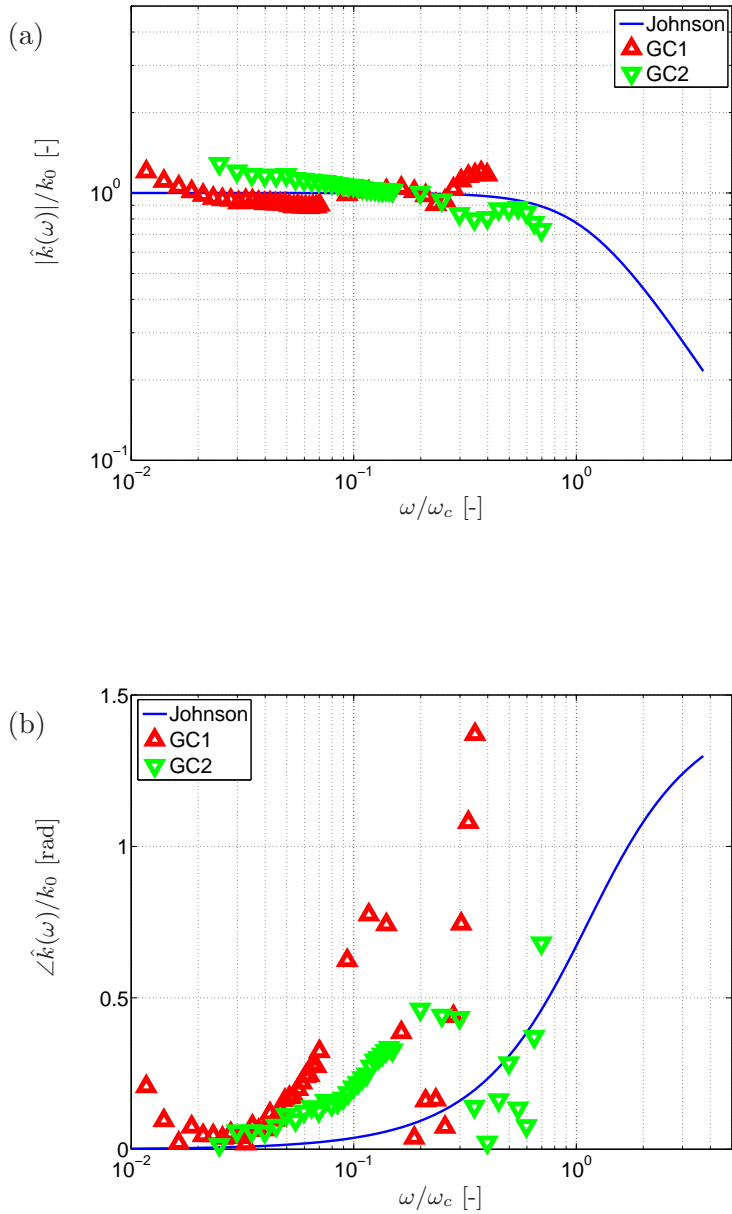


Figure 5.13: (a) Absolute and (b) phase values of the dynamic permeability for the GC1 sample. Errors are indicated by the magnitude of the data symbols.

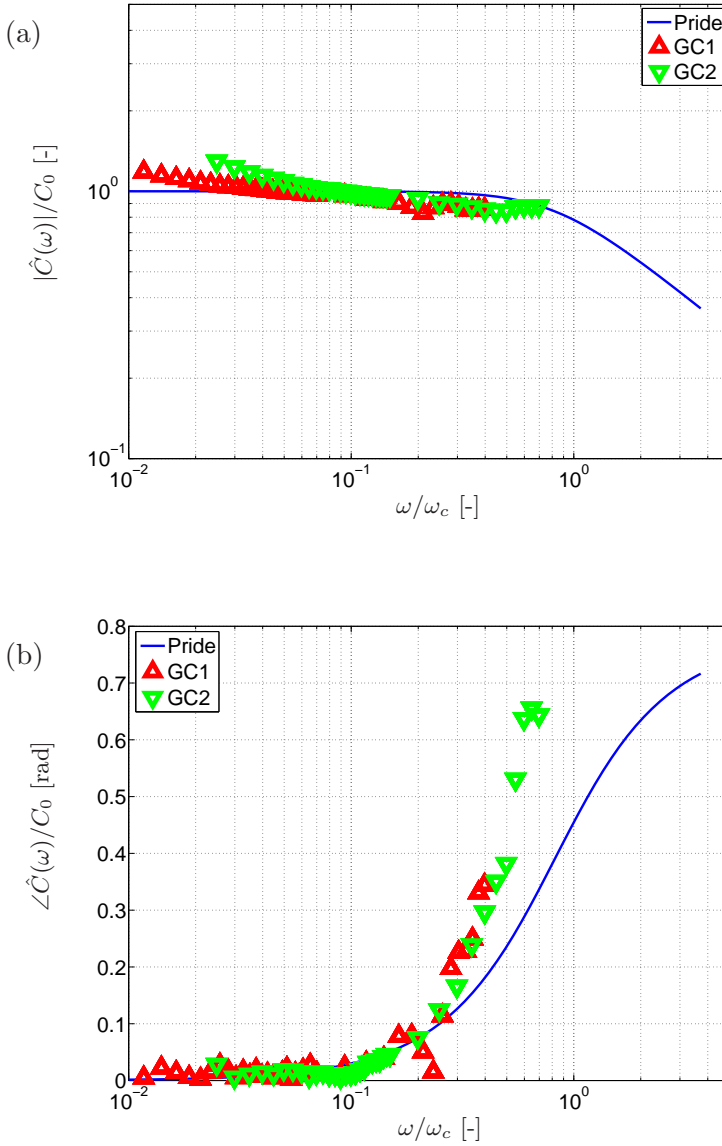


Figure 5.14: (a) Absolute and (b) phase values of the dynamic coupling coefficient for the GC1 sample. Errors are indicated by the magnitude of the data symbols.

This is probably due to the fact that the permeability of the sample is relative low, so that our assumption of rigid skeleton is no longer satisfied. This can seriously compromise the comparison between experiment and theory. Similar behaviour is also visible in the phase plot. In the electric

measurements, we notice that the oscillations have disappeared. However, there is a clear decreasing trend of the measurement values for increasing frequency, which is not predicted by theory. There are also differences if the experiments are repeated. Apparently for these materials it is more difficult to obtain a stable situation (constant pH and σ). Note that we have corrected for inaccurate p_l measurements [see (5.13)] during EK measurements, by taking its theoretical value instead of the measured one that was compromised by resonances (see Figure 5.14). The measurements of GC2 are slightly better due to the higher permeability, but suffer from the same problems as with GC1.

Chapter 6

Conclusions

In this chapter we will summarize the results of the experimental and theoretical studies of the foregoing chapters. These studies were aimed to establish the relation between (oscillatory) hydraulic flow in porous media and electric potential gradients. This coupling relation forms the basis of electrokinetic wave conversion, where acoustic waves are converted into electromagnetic waves, and vice versa.

Electrokinetic coupling in narrow channels can be evaluated analytically for parallel-plate channel configurations by solving the Poisson-Boltzmann Equation (PBE). An hydraulic flow perturbs the electric double layer (convection current), giving rise to a streaming potential and an electric counter flow that exactly balances the hydraulic ion transport. The electric counterflow induces an electro-osmotic apparent additional viscosity effect that is found to strongly decrease for wider channels.

The same coupling phenomena can obviously be found for cylindrical capillaries. Here, no exact solution for the secular equation exist so that we reside to the linearized Poisson-Boltzmann equations (LPBE). By comparing PBE and LPBE for parallel-plate channels, we show that the LPBE solution closely resembles the PBE solution for low to moderate surface potentials (zeta-potentials).

Next we study dynamic coupling phenomena in the framework of the linearized conservation laws. Theoretical descriptions by Pride and Packard for the streaming potentials are compared. It is found that they differ only slightly in the intermediate frequency range. A similar analysis for dynamic electro-osmotic shows that the coupling coefficient obeys Onsager's principle of reciprocity. This analysis is performed for both capillary and parallel-plate channels. The electrokinetic coupling can now be included in the existing Biot theory for wave propagation in porous media. It was found earlier that apart

from the original two compressional waves and one shear wave, an additional transversal EM wave mode was found that becomes diffusive for low frequencies and propagates with the speed of light (in matter), for high frequencies. We performed a detailed analysis of the effect of electrokinetic coupling on the velocity and attenuation of the three original Biot waves. Thereby it was found that the original Biot waves are affected only up to a small extent. The importance of the electrokinetic coupling therefore does not lie in the disturbance of the waves, but in the generation of a new transversal mode that can propagate outside the support of the Biot waves. For this new mode, a characteristic frequency can be defined in analogy with the characteristic frequency of the other three modes. Whereas the original characteristic frequency describes the transition from low-frequency viscosity-dominated flow towards high-frequency inertia-dominated flow, the electromagnetic characteristic frequency describes the transition from low-frequency conductivity-based behaviour towards the permittivity-based regime at high frequencies. We performed an extensive range of measurements in the so-called Dynamic Darcy Cell (DDC). It allows a direct measurement of the hydraulic pressure gradient and the streaming potentials, as a function of frequency. As the ratio of both gradients determine the coupling coefficients uniquely, we can experimentally validate the theoretical predictions by Pride and Packard. We use samples consisting of a bundle of capillaries lined-up in the flow direction. This significantly increases the solid-fluid contact area with respect to earlier measurements reported in literature so that the streaming potentials can easily be recorded by wire electrodes or porous electrode platens. The capillaries were made out of quartz glass. The frequency range of the DDC is chosen such that the wavelength is always larger than the sample size so that compressibility effects can be ignored. Capillary widths were chosen large enough to comply with the linearized Poisson-Boltzmann regime. The setup is also able to measure the dynamic permeability, which describes the relationship between the applied pressure gradient and the resulting fluid velocity. Our measurements confirm existing dynamic permeability theory. Moreover, also the electrokinetic coupling factor appeared to be in agreement with the theoretical framework by Pride and Packard. For higher frequencies resonances of the setup occurred causing the measurements to become unreliable.

The repeatability was investigated over a 4 days period. No significant changes were found for a concentration of 0.13 mM NaCl. We also investigated concentration effects in the range 0.08-0.8 mM NaCl. For lower NaCl concentrations the coupling increases significantly which is mainly due to increased fluid resistivity. These findings were in agreement with theoretical

predictions. It is interesting to note that the low-frequency coupling extrapolated from our dynamic measurements is in good agreement with the computed value from steady-state independent laboratory measurements. Also the influence of ionic species is investigated at concentrations between 0.13-0.16 mM. Apart from NaCl, we used KCl, NaI, and KI. Significant deviations from theory occurred for KCl and NaI. This is probably due to the fact that the empirical relation for the zeta-potential (2.3) does not accurately describe differences of ionic species.

We also tested the dynamic permeability and the electrokinetic coupling for capillaries made out of borosilicate glass. While the permeability measurements and the electrokinetic coupling amplitude values were in close agreement with theory, the electrokinetic coupling phase values were not. This is probably due to the fact that for this experiment we used porous platen electrodes sandwiching the sample. These platens themselves act as an electric capacitor, affecting the phase measurements.

Finally, we tested the electrokinetic coupling for more realistic porous materials made from sintered glass. No platens were used, and wire electrodes were installed in the sidewall of the liner, as was also the case for the quartz capillaries. Also for these materials a very good agreement between experiment and theory was obtained. We note that the dynamic permeability could not be measured accurately, for this material. Due to the low steady-state permeability, the material can no longer be considered completely rigid under hydraulic loading.

Bibliography

- Atkins, P. and J. de Paula (2002). *Physical chemistry*. Oxford University Press.
- Bader, S. (2005, October). *Osmosis in groundwater: Chemical and electrical extension to Darcy's law*. Ph.D Thesis, Delft University of Technology.
- Barragán, V., C. Ruiz-Bauzá, and J. Imaña (2006). Streaming potential across cation-exchange membranes in methanol - water electrolyte solutions. *Journal of Colloid and Interface Science*, **293**, 473–481.
- Basak, P. (1973). Non-Darcy flow and its implications to seepage problems. *Journal of the irrigation and drainage division*, **103**, 459–473.
- Biot, M. (1941). General theory of three-dimensional consolidation. *Journal of Applied Physics*, **12**, 155–164.
- Biot, M. (1955). Theory of elasticity and consolidation for a porous anisotropic solid. *Journal of Applied Physics*, **26**, 182–185.
- Biot, M. (1956a). Theory of propagation of elastic waves in a fluid-saturated porous solid. I-low frequency range. *Journal of the Acoustical Society of America*, **28**, 168–178.
- Biot, M. (1956b). Theory of propagation of elastic waves in a fluid-saturated porous solid. II-higher frequency range. *Journal of the Acoustical Society of America*, **28**, 179–191.
- Biot, M. and D. Willis (1957). The elastic coefficients of the theory of consolidation. *Journal of Applied Physics*, **24**, 594–601.
- Blau, L. and L. Statham (1936, September). *Method and apparatus for seismic prospecting*. U.S. Patent No. 2, 054-067.
- Broding, R. A., S. D. Buchanan, and D. P. Hearn (1963). Field experiments on the electroseismic effect. *Geophysics*, **58**, 898–903.

- Brown, R. (1980). Connection between formation factor for electrical resistivity and fluid-solid coupling factor in Biot's equations for acoustic waves in fluid-filled porous media. *Geophysics*, **45** (8), 1269–1275.
- Brunet, E. and A. Ajdari (2006). Thin double layer approximation to describe streaming current fields in complex geometries: analytical framework and applications to microfluidics. *Physical review E*, **73** (8), 1–15.
- Burgreen, D. and F. Nakache (1964). Electrokinetic flow in ultrafine capillary slits. *Journal of Physical Chemistry*, **68** (5), 1084–1091.
- Chapman, D. (1913). A contribution to the theory of electrocapillarity. *Philosophical Magazine*, **25**, 475–481.
- Charlaix, E., A. Kushnick, and J. Stokes (1988). Experimental study of dynamic permeability in porous media. *Physical Review Letters*, **61** (14), 1595–1598.
- Chun, M.-S., T. Lee, and N. Choi (2005). Microfluidic analysis of electrokinetic streaming potential induced by microflows of monovalent electrolyte solution. *Journal of Micromechanics and Microengineering*, **15**, 710–719.
- Cortis, A. (2002, May). *Dynamic acoustic parameters of porous media, a theoretical, numerical and experimental investigation*. Ph.D Thesis, Delft University of Technology.
- Deresiewicz, H. (1960). The effect of boundaries on wave propagation in a liquid-filled porous solid: I. Reflection of plane waves at a free plane boundary (non-dissipative case). *Bulletin of the Seismological Society of America*, **50**, 599–607.
- Derjaguin, B. and L. Landau (1941). Theory of the stability of strongly charged lyophobic soils and of the adhesion of strongly charged particles in solution of electrolytes. *Progress in Surface Science*, **50**, 633–662.
- Dionex (2003, February). Conductivity detection, conductance laws and electrolyte equilibria. Technical note.
- Drescher, A. and G. De Josselin de Jong (1972). Photoelastic verification of a mechanical model for the flow of a granular material. *Journal of Mechanics Physics of Solids*, **20**, 337–340.
- El-Sahed, M. and A. Salem (2004). On the generalized Navier-Stokes equations. *Applied Mathematics and Computation*, **156**, 287–293.

- Fand, R., B. Kim, A. Lam, and R. Phan (1987). Resistance to the flow of fluids through simple and complex porous media whose matrices are composed of randomly packed spheres. *Journal of Fluids Engineering*, **109**, 268–274.
- Frenkel, J. (1944). On the theory of seismic and seismoelectric phenomena in moist soil. *Journal of Physics, USSR*, **8**, 230–241.
- Gassmann, F. (1951). Über die Elastizität poröser Medien. *Vierteljahrsschrift der Naturforschenden Gesellschaft Zürich*, **96**, 1–23.
- Gouy, G. (1910). Sur la constitution de la électricité à la surface d'un électrolyte. *Journal de Physique*, **9**, 457–468.
- Haartsen, M. and S. Pride (1996). Electro seismic waves from point sources in layered media. *Journal of Geophysical Research*, **102**, 24745–24784.
- Haines, S. (2004, December). *Seismoelectric imaging of shallow targets*. Ph.D Thesis, Stanford University.
- Heister, K. (2005, May). *Flow in micro porous silicon carbide*. Ph.D Thesis, University Utrecht.
- Helmholtz, H. (1879). Studien über elektrische Grenzschichten. *Annalen der Physik und Chemie*, **7**, 337–387.
- Hunter, R. (1981). *Zeta Potential in Colloid Science*. Academic Press.
- Jocker, J. (2005, January). *Ultrasonic wave propagation in heterogeneous elastic and poroelastic media*. Ph.D Thesis, Delft University of Technology.
- Johnson, D., J. Koplik, and R. Dashen (1987). Theory of dynamic permeability and tortuosity in fluid saturated porous media. *Journal of Fluid Mechanics*, **176**, 379–402.
- Johnson, P. (1998). A Comparison of Streaming and Microelectrophoresis Methods for Obtaining the ζ Potential of Granular Porous Media Surfaces. *Journal of Colloid and Interface Science, Note*, 264–267.
- Kelder, O. (1998, February). *Frequency-dependent wave propagation in water saturated porous media*. Ph.D Thesis, Delft University of Technology.
- Kroeger, B. (2007, February). Modellierung und Sensitivitätsanalysen für Seismoelektrik mit Finiten Elementen. Technischen Universität Berlin. Ph.D Thesis.

- Langmuir, L. (1938). The role of attractive and repulsive forces in the formation of tactoids thixotropic gels, protein crystals and coacervates. *Journal of Chemical Physics*, **6**, 893.
- Levine, S., J. Marriott, and K. Robinson (1974). Theory of electrokinetic flow in a narrow parallel-plate channel. *Journal of the chemical society*, **71**, 1–11.
- Li, S., D. Pengra, and P. Wong (1995). Onsager's reciprocal relation and the hydraulic permeability of porous media. *Physical Review E*, **51** (6), 5748–5751.
- Long, L. and W. Rivers (1975). Field measurement of the electroseismic response. *Geophysics*, **40** (2), 233–245.
- Lyklema, J. (2003). Electrokinetics after Smoluchowski. *Colloid and Surfaces A*, **222**, 5–14.
- Maineult, A., Y. Bernabé, and P. Ackerer (2004). Electrical response of flow, diffusion and advection in a laboratory sand box. *Vadose Zone Journal*, **3**, 1180–1192.
- Martner, S. and N. Sparks (1959). The electroseismic effect. *Geophysics*, **14** (2), 297–308.
- Masliyah, J. and S. Bhattacharjee (2006). *Electrokinetic and colloid transport phenomena*. John Wiley & Sons.
- Mavko, G. and J. Mukerji, T. Dvorkin (2003). *The Rock Physics Handbook: Tools for Seismic Analysis in Porous Media*. Cambridge University Press.
- Mitchell, J. (1991). Conduction phenomena: from theory to geotechnical practice. *Geotechnique*, **41** (3), 299–340.
- Molina, C., L. Victoria, A. Arenas, and J. Ibáñez (1999). Streaming potential and surface charge density of microporous membranes with pore diameter in the range of thickness. *Journal of Membrane Science*, **163**, 239–255.
- Moreno, R. and O. Trevisan (1999). Modelagem de fenômenos acoplados em meios porosos. COBEM 99. 15th Brazilian Congress of Mechanical Engineering.
- Neev, J. and F. Yeats (1989). Electrokinetic effects in fluid-saturated poroelastic media. *Physical Review B*, **40**, 9135–9141.

- Neishtadt, N., L. Eppelbaum, and A. Levitski (2006). Application of piezoelectric and seismoelectrokinetic phenomena in exploration geophysics: Review of Russian and Israeli experiences. *Geophysics*, **71** (2), B41–B53.
- Oddy, M. (2005, February). *Electrokinetic transport phenomena: Mobility measurement and electrokinetic instability*. Ph.D Thesis, Stanford University.
- Onsager, L. (1931a). Reciprocal relations in irreversible processes I. *Physical Review*, **37**, 405–426.
- Onsager, L. (1931b). Reciprocal relations in irreversible processes II. *Physical Review*, **38**, 2265–2279.
- Packard, R. (1953). Streaming potentials across glass capillaries for sinusoidal pressure. *Journal of Chemical Physics*, **21**, 303–307.
- Pasquale, L., A. Winiski, C. Oliva, G. Vaio, and S. McLaughlin (1986). An experimental test of new theoretical models for the electrokinetic properties of biological membranes. *Journal of General Physiology*, **88**, 697–718.
- Pride, S. (1994). Governing equations for the coupled electromagnetics and acoustics of porous media. *Physical Review B*, **50**, 15678–15696.
- Pride, S. and S. Garambois (2005). Electrostatic wave theory of Frenkel and more recent developments. *Journal of Engineering Mechanics*, **131** (9), 898–907.
- Pride, S. and M. Haartsen (1996). Electrostatic wave properties. *Journal of the Acoustical Society of America*, **100** (3), 1301–1315.
- Pride, S. and F. Morgan (1991). Electrokinetic dissipation induced by seismic waves. *Geophysics*, **56** (7), 914–925.
- Pride, S., F. Morgan, and A. Gangi (1993). Drag forces of porous-medium acoustics. *Physical Review B*, **47** (9), 4964–4978.
- Prigogine, I. (1961). *Thermodynamics of Irreversible Processes*. New York.
- Quincke, G. (1859). Über eine neue Art elektrischer Ströme. *Annalen der Physik und Chemie*, **107** (5), 1–48.
- Reppert, P. (2000, June). *Electrokinetics in the Earth*. Ph.D Thesis, Massachusetts Institute of Technology.

- Reppert, P. and F. Morgan (2002). Frequency-Dependent Electroosmosis. *Journal of Colloid and Interface Science*, **234**, 372–383.
- Reppert, P., F. Morgan, D. Lesmes, and L. Jouniaux (2001). Frequency-Dependent Streaming Potentials. *Journal of Colloid and Interface Science*, **234**, 194–203.
- Reuss, F. (1809). Sur un nouvel effet de l'électricité galvanique. *Mémoires de la Société Imperiale de Naturalistes de Moscou*, **2**, 327–336.
- Rice, C. and R. Whitehead (1965). Electrokinetic flow in a narrow cylindrical capillary. *Journal of Physical Chemistry*, **69** (11), 4017–4024.
- Ruffet, C., Y. Gueguen, and M. Darot (1991). Complex conductivity measurements and fractal nature of porosity. *Geophysics*, **56**, 758–768.
- Schakel, M. and D. Smeulders (2010). Seismoelectric reflection and transmission at a fluid/porous medium interface. *Journal of the Acoustical Society of America*, **127**, 13–21.
- Sheng, P. and M. Zhou (1988). Dynamic permeability in porous media. *Physical review letters*, **61** (14), 1591–1594.
- Smeulders, D. (1992, June). *On wave propagation in saturated and partially saturated porous media*. Ph.D Thesis, University of Technology Eindhoven.
- Smeulders, D. (2005). Experimental evidence for slow compressional waves. *Journal of Engineering Mechanics*, **131** (29), 908–917.
- Smoluchowski, M. von (1903). Contribution à la théorie de l'endosmose électrique et de quelques phénomènes corrélatifs. *Bulletin international de l'Académie des Sciences de Cracovie*, **8**, 182–199.
- Sommerfeld, A. (1964). *Electrodynamics: Lectures on Theoretical Physics*. Academic Press.
- Stern, O. (1924). The theory of the electrolytic double-layer. *Electrochemistry*, **30**, 508.
- Sunderland, J. (1987). Electrokinetic dewatering and thickening: I. Introduction and historical review of electrokinetic applications. *Journal of Applied Electrochemistry*, **17**, 889–898.
- Tardu, S. (2004). The electric double layer effect on the microchannel flow stability and heat transfer. *Superlattices and Microstructures*, **35**, 513–529.

- Telford, W., L. Geldart, and R. Sheriff (1998). *Applied Geophysics*. Cambridge University Press.
- Terzaghi, K. (1925). *Erdbaumechanik auf bodenphysikalischer Grundlage*. Deuticke.
- Thompson, A., S. Hornbostel, J. Burns, R. Murray, J. Wride, M. P., G. Sumner, J. Haale, M. Bixby, W. Ross, B. White, M. Zhou, and P. Peczak (2006). Field tests of electroseismic hydrocarbon detection. *Geophysics*, **72** (1), N1–N9.
- Thompson, A., J. Sumner, and S. Hornbostel (2007). Electromagnetic-to-seismic conversion: A new direct hydrocarbon indicator. *Leading Edge*, **26** (4), 428–435.
- Thompson, R. (1936). The seismic electric effect. *Geophysics*, **1** (2), 327–335.
- Verruijt, A. (1982). The theory of consolidation. In: *Proc. NATO Advanced study institute on Mechanics of Fluids in Porous Media*, Nijhoff, 349–368.
- Verwey, E. and J. Overbeek (1948). Theory of the stability of lyophobic colloids. *Elsevier*.
- White, B. (2005). Asymptotic theory of electroseismic prospecting. *SIAM Journal on Applied Mathematics*, **65**, 1443–1462.
- Wisse, C. (1999, May). *On frequency dependence of acoustic waves in porous cylinders*. Ph.D Thesis, Delft University of Technology.
- Womersley, J. (2002). *The mathematical analysis of the arterial circulation in a state of oscillatory motion*. Technical Report, WADC-TR 56614.

Appendix A

Biot-Gassmann constants

This appendix reviews the relevant poroelastic parameters, which are required in the governing equations for sound propagation in elastic porous media. First, a brief summary of continuum mechanics is presented. We consider stress strain relationships in porous media, where use is made of the so-called ‘Gedanken’ experiment [Biot and Willis (1957)]. The ‘Gedanken’ experiment relates the parameters of Biot theory to the compressibility of the solid and fluid constituents. This appendix shows that these poroelastic (also known as Biot-Gassmann) parameters can be obtained by application of the continuity and constitutive laws as derived by Verruijt (1982). Finally a short description is given of the most commonly used alternative formulations of the Biot-Gassmann parameters as used in standard literature.

A.1 Continuum mechanics

A saturated porous medium consists of grains and pores, the grains are composed of a solid material and the pores contain a fluid. It is customary to formulate the behaviour of the particle assembly mathematically on a continuum level by averaging the intergranular contact forces and the velocity gradients of the grains in respectively the stress tensor and the strain tensor. This approach is only applicable when for the averaging of the physical quantities a sufficient amount of grains are taken into account. Drescher and De Josselin de Jong (1972) validated this approximation using experimental data. The relationship between the strain tensor and the stress tensor can be described with a constitutive model. The constitutive model combined with the conservation laws fully describe the kinematics of the continuum. The kinematics of this continuum is generally described in two ways. The material or Lagrangian description is employed if the material coordinates

at the reference state are used as independent variables. The spatial or Eulerian description involves the spatial coordinates at the current state as independent variables. In a two phase continuum both the fluid and the solid (grains) are treated as a continuum. Biot used an elegant Lagrangian model to derive the stress strain relations from a potential energy deformation.

A.1.1 Stress-strain relationships in porous media

After loading, a saturated porous medium can show delayed settlements, i.e. the settlements will continue after application of the load. The pore fluid cannot escape the pores as fast as the load is applied. Generally this condition is met for fine grained soils with a low permeability, e.g. peat or clayey soils, or in situations with relatively fast loading, earth-quakes, in higher permeable soils like sand. This process is known as consolidation. Already in 1925, Terzaghi was the first to notice that this process could be described using a theoretical model using the already known stress-strain relations, for which he considered a one dimensional problem, a column under a constant load. Maurice Biot expanded this theory for 3-D isotropic media [Biot (1941)] and anisotropic media [Biot (1955)].

The isotropic stress-strain relationships are derived using an extended version of the classical theory of elasticity. In this theory the derivation of a small cubic element is considered, consisting of a fluid or gas saturated poroelastic medium. However, in order to satisfy the premises of continuum mechanics, the element needs to be large compared to the grain size. It must be large enough so it can be considered homogeneous, but small enough for the macroscopic phenomena to be observed. Stresses at a point in a body are stated in an orthogonal set of axes. The equations of equilibrium are established by considering the stresses acting upon the six faces of an elementary cube. Similar to an elastic solid (or a fluid), in a porous medium stresses are defined as being tangential (shear) and normal (direct) forces per unit area of material. The total stress tensor in the bulk material is

$$\begin{bmatrix} \tau_{xx} + \xi & \tau_{xy} & \tau_{xz} \\ \tau_{yx} & \tau_{yy} + \xi & \tau_{yz} \\ \tau_{zx} & \tau_{zy} & \tau_{zz} + \xi \end{bmatrix}, \quad (\text{A.1})$$

in which $\tau_{ij} = \tau_{ji}$ (symmetry property), and ξ is the total normal force per unit bulk area, applied by the fluid on the face of the cube (also known as hydrostatic pressure of the fluid)

$$\xi = -\phi p. \quad (\text{A.2})$$

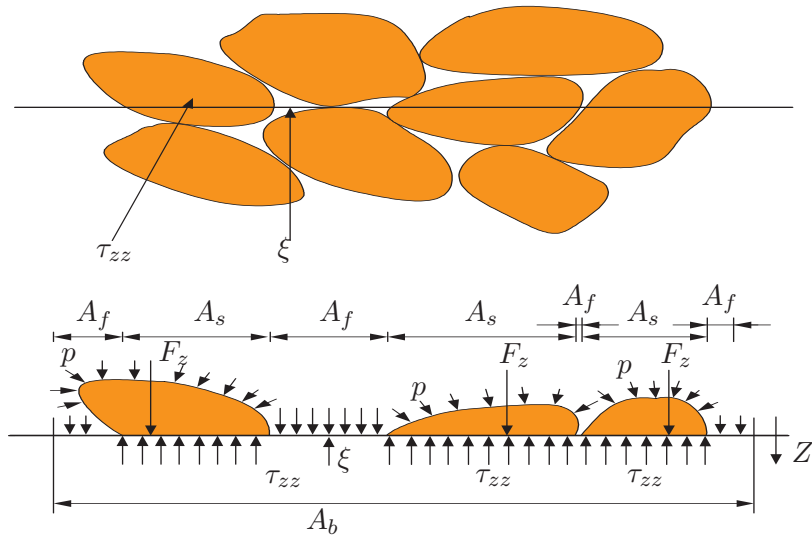


Figure A.1: One-dimensional cross-section of stress tensor in porous material, consisting out of intergranular stress ($\sum F_z/A_b = \sigma_{zz}$) and hydrostatic pressure (p).

The elastic skeleton has a statistical distribution of interconnected pores. The porosity ϕ is defined by

$$\phi = \frac{A_f}{A_b}, \quad (\text{A.3})$$

where A_f is the area of the fluid contained within the pores, and A_b is the area of the bulk material. The main component τ_{ij} is the total stress tensor, which describes the tension forces per unit bulk area applied to the portion of the cube face occupied by the solid.

$$\tau_{ij} = -\sigma_{ij} - (1 - \phi)p\delta_{ij}, \quad (\text{A.4})$$

here σ_{ij} is the additional intergranular stress, and δ_{ij} is the Kronecker symbol, indicating that pore fluid cannot exert nor sustain any shear force.

We will now proceed by considering two commonly used tests, in which the volume effects caused by pore pressure and intergranular stresses are studied separately. The first test is the ‘unjacketed test’, in which a porous sample is fully submerged in a water tank (pressure change dp_e), the fluid pressure is continuous over the interface. The intergranular stress is zero, just as the porosity change. This makes us capable of determining the volume change of the matrix grains dV_s and the change of the bulk volume dV_b see Table A.1.

For the second test, the porous sample is jacketed and fully submerged in a water tank. The inner side of the jacket can communicate with the atmosphere through a tube to ensure constant internal fluid pressure. The pressure change in the water tank now equals the change of the intergranular stress. As there are no pore pressure changes, the ‘jacketed test’ is used to study the volumetric effects caused by intergranular stresses. Also in this case we are capable of determining the bulk volume change and volume change of the particles. Where K_s is the bulk modulus of the solid, which for homoge-

Table A.1: Characteristic relationships in the ‘Gedanken’ experiment for jacketed and unjacketed porous sample.

	$d\phi$	dV_s	dV_b	dp	$d\sigma$
Unjacketed	0	$-\frac{V_s}{K_s} dp_e$	$-\frac{V_b}{K_s} dp_e$	dp_e	0
Jacketed	$-\left[\frac{1-\phi}{K_{fr}} - \frac{1}{K_s}\right] dp_e$	$-\frac{V_s}{K_s(1-\phi)} dp_e$	$-\frac{V_b}{K_{fr}} dp_e$	0	dp_e

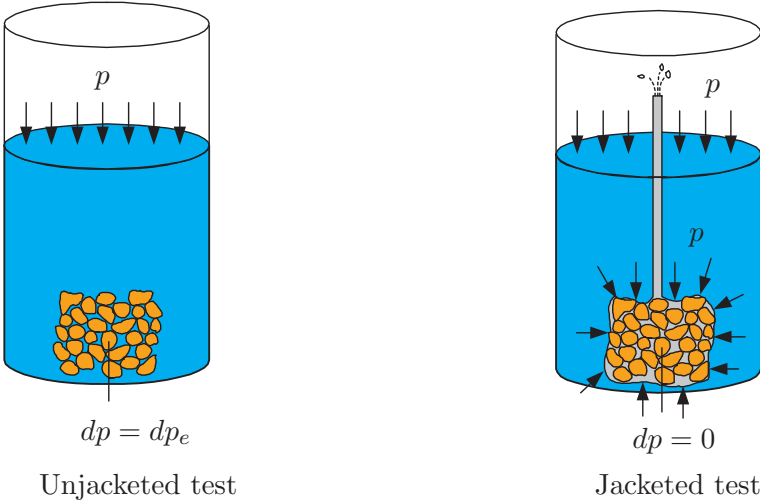


Figure A.2: Unjacketed and jacketed test from the ‘Gedanken’ experiment.

neous media can also be interpreted as the bulk modulus of the single grains. The bulk modulus can be determined by measuring the displacements of the boundary surfaces of the sample. The other bulk modulus, K_{fr} , is the frame (or matrix) bulk modulus.

The bulk volume change can be obtained by superposition of the bulk volume change of the jacketed and unjacketed test in the so called ‘Gedanken’ experiment. This is the summation of change of intergranular stress and pore

pressure (see Table A.1).

$$dV_b = -\frac{V_b}{K_{fr}}d\sigma - \frac{V_b}{K_s}dp, \quad (\text{A.5})$$

using the direct volumetric strain relationship $e = dV_b/V_b$, (A.5) becomes

$$-\frac{\partial\sigma}{\partial t} = K_{fr}\frac{\partial e}{\partial t} + \frac{K_{fr}}{K_s}\frac{\partial p}{\partial t}. \quad (\text{A.6})$$

When the material is sheared, the total shear stress is fully dissipated by the grain contacts, this means that the strain is governed by the intergranular or effective stress in the material. The rock shear modulus G can be incorporated following Hook's law for an isotropic solid, into (A.6) (see Verruijt (1982)),

$$-\sigma_{ij} = (K_{fr} - \frac{2}{3}G)e\delta_{ij} + 2Ge_{ij} + \frac{K_{fr}}{K_s}p\delta_{ij}, \quad (\text{A.7})$$

where e_{ij} is the strain component of the solid

$$e_{ij} = \frac{1}{2} \left(\frac{\partial u_{sj}}{\partial x_i} + \frac{\partial u_{si}}{\partial x_j} \right), \quad (\text{A.8})$$

$$\epsilon_{ij} = \frac{1}{2} \left(\frac{\partial u_{fj}}{\partial x_i} + \frac{\partial u_{fi}}{\partial x_j} \right), \quad (\text{A.9})$$

and ϵ_{ij} the strain component of the fluid. These are linear elastic deformations of an elementary cube, which are completely reversible.

Continuity and constitutive equations

One of the major principles in the theory of consolidation is that the mass of the two phases, solid and fluid must be

$$\frac{\partial(\phi\rho_f)}{\partial t} + \nabla \cdot (\phi\rho_f\mathbf{u}_f) = 0, \quad (\text{A.10})$$

$$\frac{\partial((1-\phi)\rho_s)}{\partial t} + \nabla \cdot ((1-\phi)\rho_s\mathbf{u}_s) = 0, \quad (\text{A.11})$$

where ρ_f , ρ_s are the fluid and solid density and \mathbf{u}_f and \mathbf{u}_s average fluid and solid displacement.

The continuity equation needs to be completed, using the constitutive relations. They are obtained by describing the change of the particle volume as

function of the change in pore pressure change and the change of intergranular stress. This is a summation of the jacketed and unjacketed volume change in the ‘Gedanken’ experiment

$$\frac{1}{\rho_s} \frac{\partial \rho_s}{\partial t} = \frac{1}{K_s} \frac{\partial p}{\partial t} + \frac{1}{(1-\phi)} \frac{1}{K_s} \frac{\partial \sigma}{\partial t}, \quad (\text{A.12})$$

$$\frac{1}{\rho_f} \frac{\partial \rho_f}{\partial t} = \frac{1}{K_f} \frac{\partial p}{\partial t}, \quad (\text{A.13})$$

with K_f the fluid bulk modulus, $\mathbf{v}_s = \frac{\partial \mathbf{u}_s}{\partial t}$ and $\mathbf{v}_f = \frac{\partial \mathbf{u}_f}{\partial t}$ are the averaged solid and fluid velocities respectively. Substitution of the constitutive equations (A.12) and (A.13) into the conservation laws (A.10) and (A.11) results into

$$\frac{(1-\phi)}{K_s} \frac{\partial p}{\partial t} + \frac{1}{K_s} \frac{\partial \sigma}{\partial t} - \frac{\partial \phi}{\partial t} + (1-\phi) \nabla \cdot \mathbf{v}_s = 0, \quad (\text{A.14})$$

$$\frac{\phi}{K_f} \frac{\partial p}{\partial t} + \frac{\partial \phi}{\partial t} + \phi \nabla \cdot \mathbf{v}_f = 0. \quad (\text{A.15})$$

Combination of the solid, (A.14) with the fluid (A.15), results in the storage equation

$$\left(\frac{(1-\phi)}{K_s} + \frac{\phi}{K_f} \right) \frac{\partial p}{\partial t} + \frac{1}{K_s} \frac{\partial \sigma}{\partial t} + (1-\phi) \nabla \cdot \mathbf{v}_s + \phi \nabla \cdot \mathbf{v}_f = 0. \quad (\text{A.16})$$

To obtain an expression for the pressure, from which σ is removed we need to incorporate the stress-strain (A.6), in combination with the identity $\partial e / \partial t = \nabla \cdot \mathbf{v}_s$

$$\left(\frac{(1-\phi)}{K_s} + \frac{\phi}{K_f} - \frac{K_{fr}}{K_s^2} \right) \frac{\partial p}{\partial t} + \left(1 - \phi - \frac{K_{fr}}{K_s} \right) \nabla \cdot \mathbf{v}_s + \phi \nabla \cdot \mathbf{v}_f = 0. \quad (\text{A.17})$$

Before proceeding we define the effective porosity,

$$\phi_{eff} = \phi + \frac{K_f}{K_s} \left(1 - \phi - \frac{K_{fr}}{K_s} \right), \quad (\text{A.18})$$

combined with the storage (A.17) results in

$$-\phi \frac{\partial p}{\partial t} = \phi \frac{K_f}{\phi_{eff}} \left(1 - \phi - \frac{K_{fr}}{K_s} \right) \nabla \cdot \mathbf{v}_s + \phi^2 \frac{K_f}{\phi_{eff}} \nabla \cdot \mathbf{v}_f. \quad (\text{A.19})$$

This equation is often simplified into

$$-\phi \frac{\partial p}{\partial t} = Q \nabla \cdot \mathbf{v}_s + R \nabla \cdot \mathbf{v}_f, \quad (\text{A.20})$$

where Q and R are two of the three Biot-Gassmann constants

$$Q = \phi \frac{K_f}{\phi_{eff}} \left(1 - \phi - \frac{K_{fr}}{K_s} \right), \quad (\text{A.21})$$

$$R = \phi^2 \frac{K_f}{\phi_{eff}}. \quad (\text{A.22})$$

A similar approach to the pressure can be followed for the stress-strain relationship as derived in (A.7). Taking the time derivative of (A.7) and removing the pressure change as function of time by substitution of (A.17), we obtain

$$\begin{aligned} -\frac{\partial \sigma_{ij}}{\partial t} &= \left(K_{fr} - \frac{2}{3}G - \frac{K_{fr}}{K_s} \frac{K_f}{\phi_{eff}} \left(1 - \phi - \frac{K_{fr}}{K_s} \right) \right) \nabla \cdot \mathbf{v}_s \delta_{ij} + \\ &+ 2G \frac{\partial e_{ij}}{\partial t} - \phi \frac{K_{fr}}{K_s} \frac{K_f}{\phi_{eff}} \nabla \cdot \mathbf{v}_f \delta_{ij}. \end{aligned} \quad (\text{A.23})$$

Introducing the total stress tensor as defined in (A.4), we obtain by subtracting $(1 - \phi) \frac{\partial p}{\partial t} \delta_{ij}$ from (A.23)

$$\begin{aligned} -\frac{\partial \sigma_{ij}}{\partial t} - (1 - \phi) \frac{\partial p}{\partial t} \delta_{ij} &= \left[K_{fr} - \frac{K_{fr}}{K_s} \frac{K_f}{\phi_{eff}} \left(1 - \phi - \frac{K_{fr}}{K_s} \right) - \frac{2}{3}G + \right. \\ &+ \left. (1 - \phi) \frac{K_f}{\phi_{eff}} \left(1 - \phi - \frac{K_{fr}}{K_s} \right) \right] \nabla \cdot \mathbf{v}_s \delta_{ij} + \\ &+ 2G \delta_{ij} \frac{\partial e_{ij}}{\partial t} + \left(\frac{\phi}{\phi_{eff}} K_f \left(1 - \phi - \frac{K_{fr}}{K_s} \right) \right) \nabla \cdot \mathbf{v}_f \delta_{ij}, \end{aligned} \quad (\text{A.24})$$

or in a more compact form

$$\frac{\partial \tau_{ij}}{\partial t} = A \nabla \cdot \mathbf{v}_s \delta_{ij} + 2G \delta_{ij} \frac{\partial e_{ij}}{\partial t} + Q \nabla \cdot \mathbf{v}_f \delta_{ij}, \quad (\text{A.25})$$

where A stands for

$$A = \left(\phi \frac{K_{fr}}{\phi_{eff}} + (1 - \phi) \frac{K_f}{\phi_{eff}} \left(1 - \phi - \frac{K_{fr}}{K_s} \right) - \frac{2}{3}G \right). \quad (\text{A.26})$$

The parameters A , Q and R are generalized elastic parameters also known as the Biot-Gassmann parameters, which are related to measurable properties of the poroelastic medium Biot (1955); Biot and Willis (1957); Smeulders (1992).

Appendix B

Parameter determination

B.1 Basic mechanical parameters

B.1.1 Porosity

The porosity of the applied porous samples can be measured using a variety of techniques. A common technique is the buoyancy method. First the dry weight of the porous sample is determined and then the weight of the sample under fully saturated conditions is measured. The measured average porosity and particle density is determined from Jocker (2005), Smeulders (1992)

$$\phi = \frac{G_0 - G_1 + g\rho_f V_b}{g\rho_f V_b}, \quad (\text{B.1})$$

$$\rho_s = \frac{G_0 \rho_f}{G_0 - G_1}, \quad (\text{B.2})$$

in which V_b is the bulk volume of the sample, g the gravitational acceleration, G_0 and G_1 the dry weight and the fully saturated weight of the porous sample, respectively. The experimentally determined values can be found in Table 5.1.

B.1.2 Permeability

Stationary permeability can be determined in a variety of ways. Use can be made of a constant or falling head test or a constant flow-rate test, both have been used. A closer look will be taken at the constant flow-rate test, see Figure B.1 and B.2. For low velocities Darcy's law holds

$$\frac{\partial p}{\partial x} = -\frac{\phi \eta Q_0}{k_0 A_0}, \quad (\text{B.3})$$

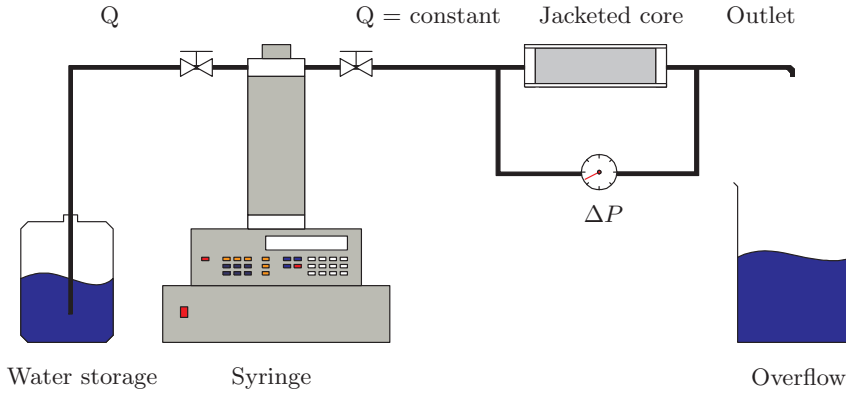


Figure B.1: Set-up constant flow-rate test.

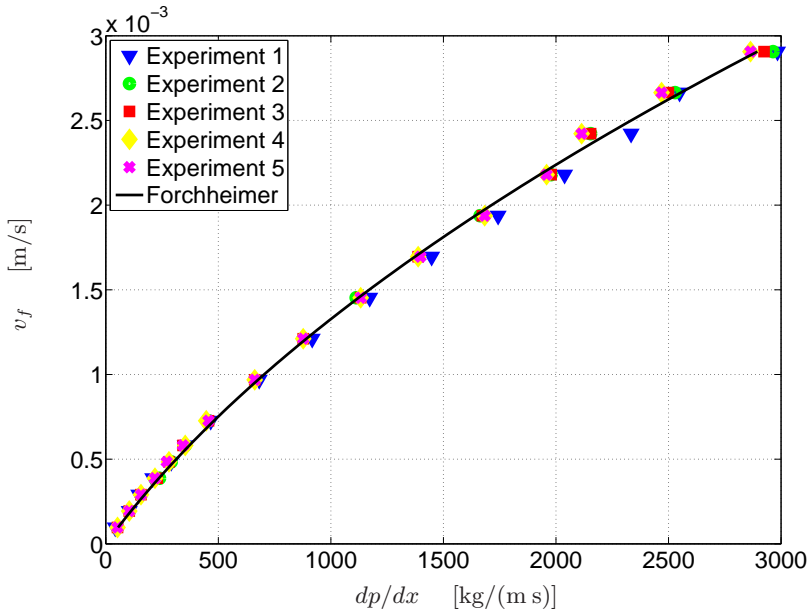


Figure B.2: Flow rate versus pressure, using constant flow rate (BSC core see Table 5.1). Experiments 1-5 denote repeated experiments at different times.

where Q_0 is the average flow rate, and A_0 is the total cross sectional area of the porous sample. For higher velocities, inertial forces are not negligible (higher Reynolds numbers). Forchheimer derived the following empirical equation for a nonlinear relationship between flow rate and pressure gradient [Basak (1973), Fand et al. (1987), Mavko and Mukerji (2003)]

$$\frac{\partial p}{\partial x} = -\frac{\phi\eta}{k_0} \frac{Q_0}{A_0} + b_f \rho_f \left(\frac{Q_0}{A_0} \right)^2, \quad (\text{B.4})$$

where b_f is Forchheimer's coefficient. During the experiments use has been made of the Dynamic Darcy Cell (see Chapter 5), in which also the static permeability can be measured.

B.1.3 Tortuosity

The tortuosity can be determined using an electric conductivity experiment (for non-ferro porous media). Brown (1980) was the first to demonstrate that there is an analogy between the acceleration of an inviscid incompressible fluid within a rigid porous medium versus the electric current density within an electrolyte filled with a porous insulator

$$\chi = \frac{\alpha_\infty}{\phi} = \frac{\sigma_s}{\sigma_f}. \quad (\text{B.5})$$

where χ the formation factor consists of the tortuosity α_∞ , σ_s the conductivity of the fluid within a porous insulator and σ_f the intrinsic fluid conductivity. An experimental set-up is described in Jocker (2005), Kelder (1998), Smeulders (1992).

B.2 Conductivity determination

Electric currents can propagate in rocks and minerals in three ways. The first way is electric conduction, a current flow in materials, which contain free electrons such as metals. The second way is dielectric conduction, where the current flow takes place in a poor conductor, which has very few carriers or none at all. The current produced in dielectric material is known as as the displacement current. The third way is through an electrolyte, where the current is carried by ions at fluid flow velocity [Telford et al. (1998)]. In this section we will take a closer look the third method of current propagation. The electric bulk-fluid conductivity σ_f is written assuming a thin, uniform,

double layer. The bulk-fluid conductivity can then be computed according to

$$\sigma_f = \sum_{l=1}^L (e_0 z_l)^2 b_l N_l^\infty, \quad (\text{B.6})$$

with b_l the mobility of the fluid. The mobility can be computed using the Stokes' relation

$$b_l = \frac{1}{6\pi\eta a}, \quad (\text{B.7})$$

where a is the effective ion radius. Stokes' relation gives us a theoretical value for the frictional coefficient of a spherical particle in a solvent. The particle radius is not simply the physical radius of the molecule, but is rather the effective radius of the ion in the solution. It is the effective radius solution taking into account all the H₂O molecules it carries in its hydration sphere. The size of the ions is crucial, small ions give rise to stronger electric fields than big ions. So ion of small radius may have a large hydrodynamic radius because it drags many solvent molecules through the solution as it migrates. A limitation is that the formula is strictly speaking only accurate for a single spherical particle [Atkins and de Paula (2002)]. The bulk-ionic concentration is a function of the number of Avogadro N_a

$$N_l^\infty = \left(c_q \frac{\text{mol}}{l} \right) \left(N_a \frac{1}{\text{mol}} \right) \left(1000 \frac{l}{m^3} \right) = c_q N_a \cdot 10^3, \quad (\text{B.8})$$

and the concentration c_q . Combination of these results gives the conductivity at room temperature

$$\sigma_{f_{298}} = \sum_{l=1}^L \frac{(e z_l)^2 c_q N_a \cdot 10^3}{6\pi\eta a}. \quad (\text{B.9})$$

Conductivity also depends on the temperature

$$\sigma_f = \sigma_{f_{298}} e^{0.02(T-298)}, \quad (\text{B.10})$$

with T temperature Dionex (2003).

The total electric conductance of a solution depends upon the type, temperature and concentration of all ions present [Ruffet et al. (1991)]. It is not a specific function for any ionic species. The electric current is carried by both anions and cations in a solution. The above described theoretical model has been validated by laboratory measurements.

Table B.1: Electric conductivity of water types [Masliyah and Bhattacharjee (2006)].

Ultra pure H_2O		Good quality distilled H_2O		Good quality tap water		0.05 % $NaCl$		Sea water		30 % H_2SO_4
↓		↓		↓		↓		↓		↓
1	10	100	1	10	100	1	3	10	100	
$\mu S/m$	$\mu S/m$	$\mu S/m$	mS/m	mS/m	mS/m	S/m	S/m	S/m	S/m	

The conductivity of water ranges over several orders of magnitudes (Table B.1). We performed measurements of different solutions. The experiments are performed using the **WTW LF 340** conductivity meter. It is capable of measuring the conductivity and temperature at the same time. Table B.1 shows an estimate of electric conductivity of a variety of fluid solutions. During the measurements in this work, use has been made of good quality distilled water with conductivities just below 0.1 mS/m . The conductivity measurements are repeated five times over for two different sorts of salt in distilled water, sodium chloride $NaCl$ and potassium chloride KCl respectively. Both salts dissolve in water



The molecular mass and molarity have the following values. For $NaCl$ we have that $22.990u + 35.453u = 58.443u = 58.443\text{ g/mol}$ and for KCl that $39.102u + 35.453u = 74.555u = 74.555\text{ g/mol}$, with u the atomic mass-unit. The conductivity has been measured for a variety of concentrations [$1 \cdot 10^{-4}\text{ mol/l} - 1 \cdot 10^{-1}\text{ mol/l}$], at different temperatures [$1^\circ C - 50^\circ C$] for both salts. A comparison between theory and experiment for the conductance as function of the temperature and concentration is shown in Figure B.3 to B.6 for sodium chloride and in Figure B.7 to B.10 for potassium chloride. It can be seen that there is a good match between theory (B.10) and measurement. For sodium chloride, from $1 \cdot 10^{-1}\text{ mol/l}$ and onwards a deviation between measurement and theory occurs, for potassium chloride it occurs at much

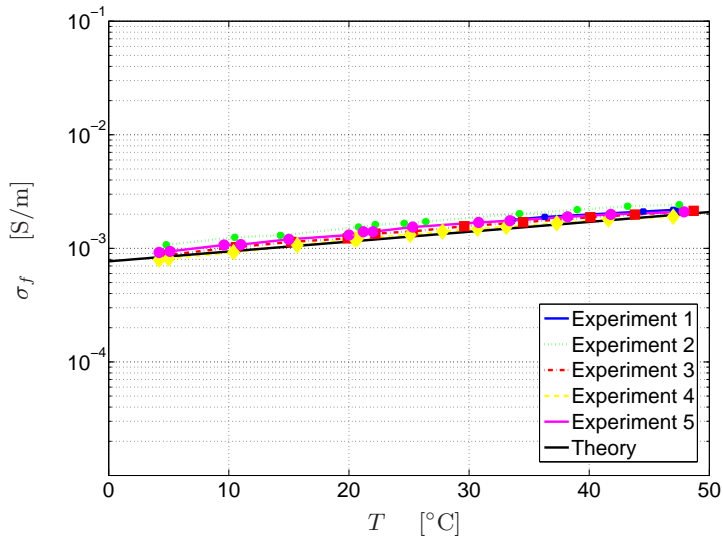


Figure B.3: Conductivity of NaCl as function the temperature, $1 \cdot 10^{-4}$ mol/l. Experiments 1-5 denote repeated experiments at different times.

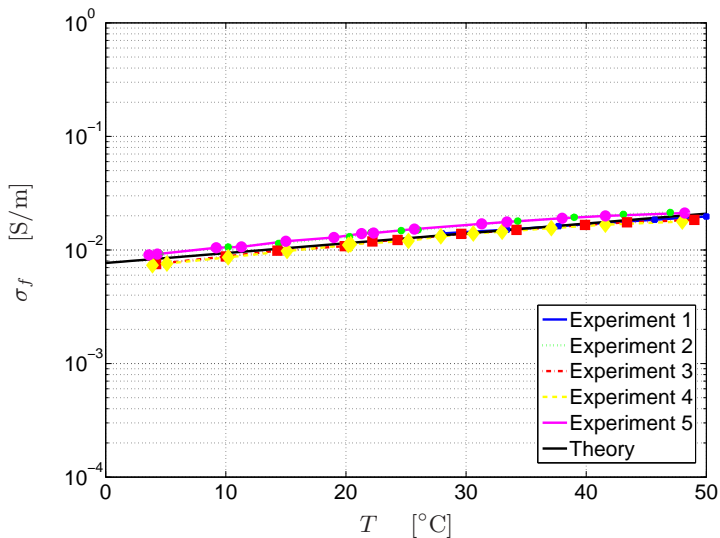


Figure B.4: Conductivity of NaCl as function the temperature, $1 \cdot 10^{-3}$ mol/l. Experiments 1-5 denote repeated experiments at different times.

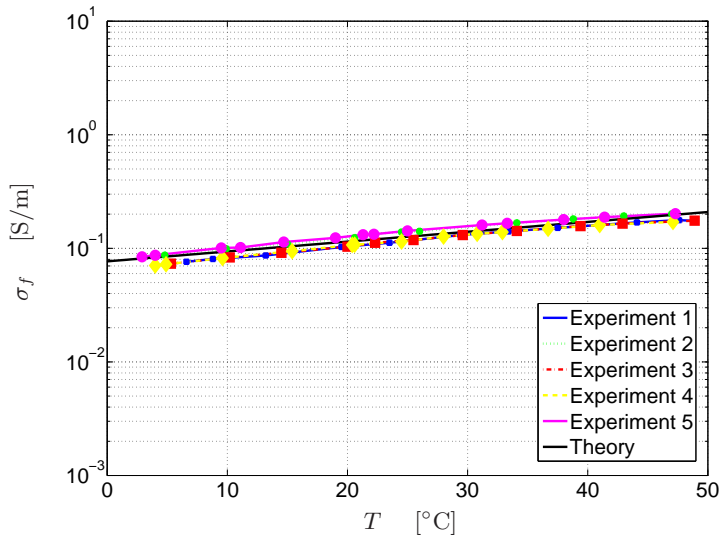


Figure B.5: Conductivity of NaCl as function the temperature, $1 \cdot 10^{-2}$ mol/l. Experiments 1-5 denote repeated experiments at different times.

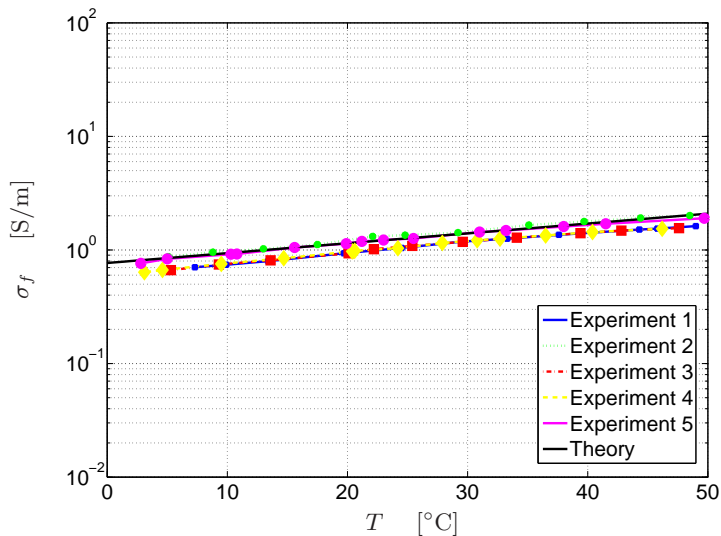


Figure B.6: Conductivity of NaCl as function the temperature, $1 \cdot 10^{-1}$ mol/l. Experiments 1-5 denote repeated experiments at different times.

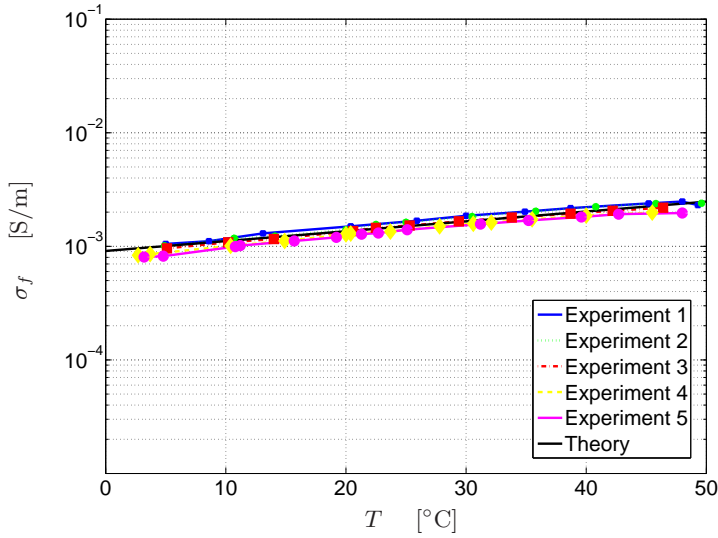


Figure B.7: Conductivity of KCl as function the temperature, $1 \cdot 10^{-4}$ mol/l. Experiments 1-5 denote repeated experiments at different times.

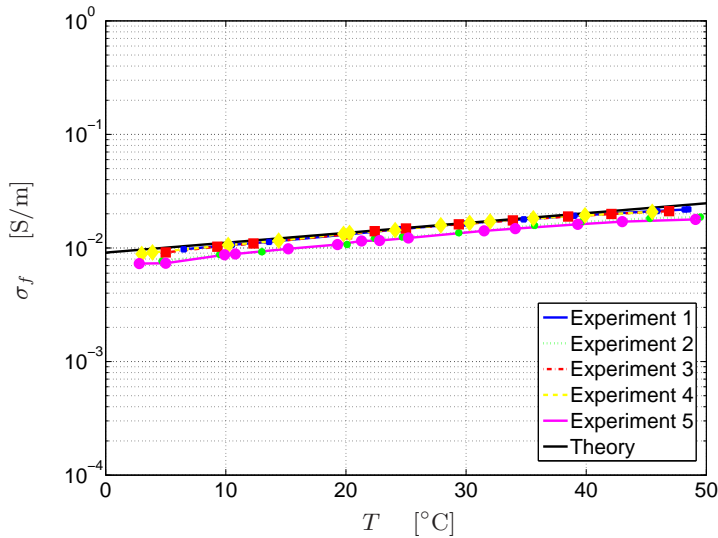


Figure B.8: Conductivity of KCl as function the temperature, $1 \cdot 10^{-3}$ mol/l. Experiments 1-5 denote repeated experiments at different times.

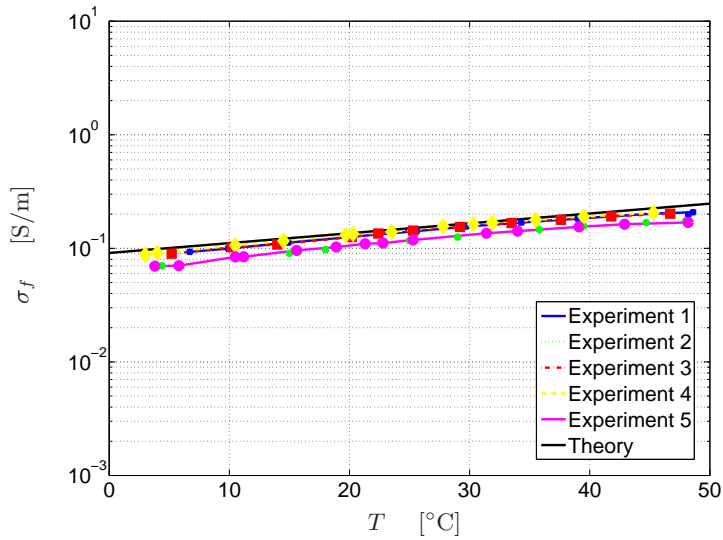


Figure B.9: Conductivity of KCl as function the temperature, $1 \cdot 10^{-2}$ mol/l. Experiments 1-5 denote repeated experiments at different times.

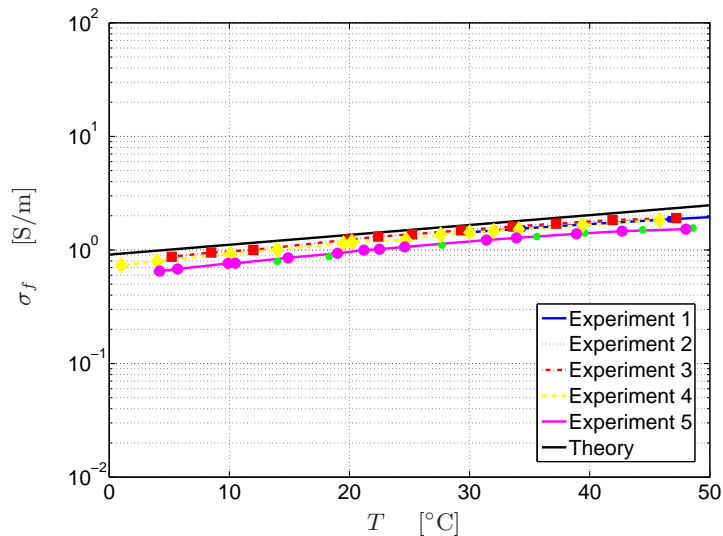


Figure B.10: Conductivity of KCl as function the temperature, $1 \cdot 10^{-1}$ mol/l. Experiments 1-5 denote repeated experiments at different times.

lower concentrations. The applied theoretical model is not applicable in this range.

B.2.1 Dynamic conductivity coefficient

The dynamic conductivity is derived by Pride (1994) from the extended version of Ohm's law (4.20). Ohm's law is composed of the conduction current \mathbf{J}_c and the streaming current \mathbf{J}_s

$$\mathbf{J} = (\mathbf{J}_c + \mathbf{J}_s) = \hat{L}(\omega)(-\nabla\hat{p} + \omega^2\rho_f\hat{\mathbf{u}}_s) + \hat{\sigma}(\omega)\hat{\mathbf{E}}, \quad (\text{B.11})$$

The average conduction current for isotropic media is

$$\mathbf{J}_c = \frac{\phi}{\alpha_\infty} \left(\sigma_f + \frac{2C_{em}}{\Lambda} \right) \hat{\mathbf{E}}, \quad (\text{B.12})$$

with C_{em} the excess conductance associated to the electromigration of double layer ions. An exact expression for C_{em} can only be obtained by a numerical integration of the Poisson-Boltzmann equation in case of a multicomponent electrolyte with no restriction on ζ . An accurate analytical estimate can be obtained using Debye's approximation (2.20)

$$C_{em} \approx 2d \sum_{l=1}^L (ez_l)^2 b_l N_l \left[e^{\left(-\frac{ez_l\zeta}{2k_B T}\right)} - 1 \right]. \quad (\text{B.13})$$

The other contribution stems from the streaming current, which can be separated into an electric induced current (\mathbf{J}_{se}) and a mechanically induced current (\mathbf{J}_{sm}); $\mathbf{J}_s = \mathbf{J}_{se} + \mathbf{J}_{sm}$. The electric induced current has the form

$$\mathbf{J}_{se} = \phi \frac{2\hat{C}_{os}(\omega)}{\alpha_\infty\Lambda} \hat{\mathbf{E}}, \quad (\text{B.14})$$

with \hat{C}_{os} the conductance due to electric induced streaming (convection) of the excess double layer ions, also known as the electro-osmotic conductance. Similar to the excess charge conductance an approximation can be obtained, where we will use Debye's approximate flow field

$$\hat{C}_{os}(\omega) = \frac{(\epsilon_0\epsilon_{rf})^2\zeta^2}{2d\eta} P_0 \left(1 + \frac{2}{P_0} d \sqrt{\frac{i\omega\rho_f}{\eta}} \right)^{-1}, \quad (\text{B.15})$$

with P the dimensionless parameter defined as

$$P_0 = \frac{8k_B T d^2}{(\epsilon_0\epsilon_{rf})\zeta^2} \sum_{l=1}^L N_l \left[e^{\left(-\frac{ez_l\zeta}{2k_B T}\right)} - 1 \right]. \quad (\text{B.16})$$

The mechanically induced current has the form

$$\mathbf{J}_{sm} = \hat{L}(\omega)(-\nabla\hat{p} + \omega^2\rho_f\hat{\mathbf{u}}_s). \quad (\text{B.17})$$

Substitution of (B.17), (B.14) and (B.12) in the extended version of Ohm's

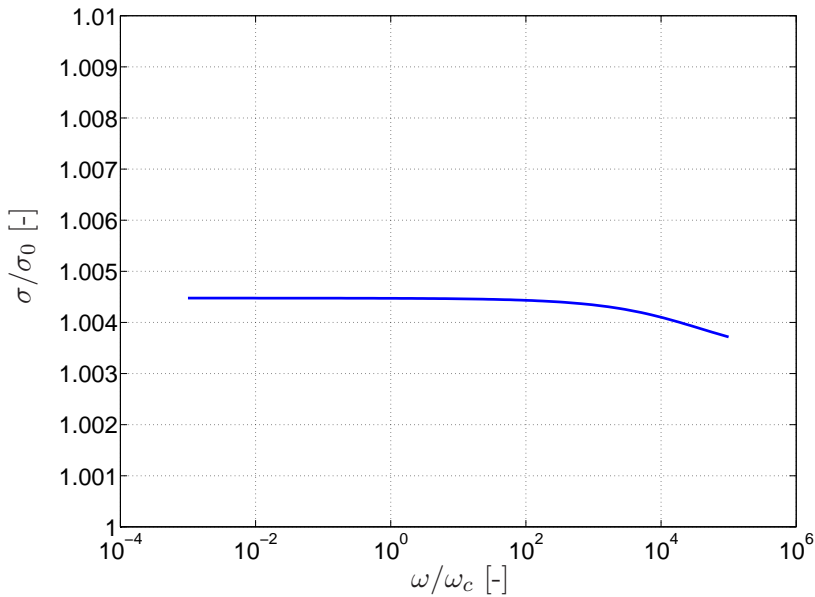


Figure B.11: Dynamic conductivity of potassium chloride, for $c_q = 1 \cdot 10^{-3}$ mol/l, see table 3.2.

law (B.11) gives the dynamic conductivity for a porous medium of arbitrary pore structure

$$\hat{\sigma}(\omega) = \frac{\phi}{\alpha_\infty}\sigma_f \left[1 + \frac{2}{\sigma_f\Lambda}(C_{em} + C_{os}(\omega)) \right]. \quad (\text{B.18})$$

There is only a weak dependence on the frequency. This dependence is caused by the electro-osmotic conductance due to the electrically driven viscous-flow to inertial-flow transition. Similar to the dynamic EK coupling coefficient (3.37), the dynamic conductivity coefficient is simplified because for the frequencies of interest, the viscous skin depth for most materials is larger than the Debye length, which leads to negligible relaxation

$$\hat{\sigma}(\omega) \Rightarrow \sigma_0 = \frac{\phi}{\alpha_\infty}\sigma_f, \quad (\text{B.19})$$

with σ_0 the total fluid's electric conductivity in a porous medium [Pride and Garambois (2005)].

Appendix C

Elliptic integral solution

C.1 Elliptic integral of the first kind

We start with the relation (2.32)

$$\frac{d\tilde{\Phi}}{d\tilde{z}} = \sqrt{2 \cosh(\tilde{\Phi}) - 2 \cosh(\tilde{\Phi}_0)}. \quad (\text{C.1})$$

Substitution of (2.33) and (2.34) yields that

$$d\tilde{z} = \frac{d\tilde{\Phi}}{\sqrt{e^{\tilde{\Phi}} + e^{-\tilde{\Phi}} - (e^{\tilde{\Phi}_0} + e^{-\tilde{\Phi}_0})}} = \frac{d\tilde{\Phi}}{\sqrt{\frac{1}{r \sin^2(\theta)} + r \sin^2(\theta) - \left(\frac{1}{r} + r\right)}}. \quad (\text{C.2})$$

Using (2.34), we find that

$$d\tilde{z} = -2r^{\frac{1}{2}} \frac{d\theta}{\sqrt{1 - r^2 \sin^2(\theta)}}. \quad (\text{C.3})$$

We integrate from zero to \tilde{z}

$$\int_0^{\tilde{z}} d\tilde{z}' = 2\sqrt{r} \left(\int_0^{\frac{\pi}{2}} \frac{d\theta'}{\sqrt{1 - r^2 \sin^2(\theta')}} - \int_0^{\theta} \frac{d\theta'}{\sqrt{1 - r^2 \sin^2(\theta')}} \right). \quad (\text{C.4})$$

This becomes

$$\tilde{z} = 2\sqrt{r} \left(F\left(\frac{1}{2}\pi, r\right) - F(\theta, r) \right), \quad (\text{C.5})$$

with $F(\frac{1}{2}\pi, r)$ the complete elliptic integral of the first kind

$$F\left(\frac{1}{2}\pi, r\right) = \int_0^{\frac{\pi}{2}} \frac{d\theta'}{\sqrt{1 - r^2 \sin^2(\theta')}}}, \quad (\text{C.6})$$

and $F(\theta, \mathbf{r})$ the incomplete elliptic integral of the first kind

$$F(\theta, \mathbf{r}) = \int_0^\theta \frac{d\theta'}{\sqrt{1 - \mathbf{r}^2 \sin^2(\theta')}}. \quad (\text{C.7})$$

C.2 Elliptic integral of the second kind

We consider (2.57):

$$-\frac{M_q}{\sigma H} \int \rho_E \left(1 - \frac{\Phi}{\zeta}\right) dz = \frac{M_q \varepsilon}{\sigma \tilde{H}} \int_0^H \frac{\partial^2 \tilde{\Phi}}{\partial \tilde{z}^2} \left(1 - \frac{\Phi}{\zeta}\right) d\tilde{z}. \quad (\text{C.8})$$

Substituting the reduced variables $\tilde{z} = \kappa z$ and $\tilde{\Phi} = \Phi/\Phi_B$ we find that

$$\frac{M_q \varepsilon}{\sigma \tilde{H}} \int_0^H \frac{\partial^2 \tilde{\Phi}}{\partial \tilde{z}^2} \left(1 - \frac{\Phi}{\zeta}\right) dz = \frac{M_q \varepsilon \kappa^2 \Phi_B}{\sigma \tilde{H}} \int_0^{\tilde{H}} \frac{\partial^2 \tilde{\Phi}}{\partial \tilde{z}^2} \left(1 - \frac{\tilde{\Phi}}{\tilde{\Phi}_s}\right) d\tilde{z}. \quad (\text{C.9})$$

Partial integration of (2.57) yields that

$$\int_0^{\tilde{H}} \frac{\partial^2 \tilde{\Phi}}{\partial \tilde{z}^2} \left(1 - \frac{\tilde{\Phi}}{\tilde{\Phi}_s}\right) d\tilde{z} = \frac{1}{\tilde{\Phi}_s} \int_0^{\tilde{\Phi}_s} \frac{\partial \tilde{\Phi}}{\partial \tilde{z}} d\tilde{\Phi}. \quad (\text{C.10})$$

From (2.33) and (C.3), we have that

$$\frac{\partial \tilde{\Phi}}{\partial \tilde{z}} = \frac{1}{\sqrt{\mathbf{r}}} \cot(\theta) \Delta \theta. \quad (\text{C.11})$$

with $\Delta(\theta) = \sqrt{1 - \mathbf{r}^2 \sin^2(\theta)}$. This means that the integral (C.10) now becomes

$$\frac{1}{\tilde{\Phi}_s} \int_0^{\tilde{\Phi}_s} \frac{\partial \tilde{\Phi}}{\partial \tilde{z}} d\tilde{\Phi} = \frac{2}{\tilde{\Phi}_s \sqrt{\mathbf{r}}} \int_{\theta_w}^{\frac{\pi}{2}} \cot^2(\theta) \Delta \theta d\theta. \quad (\text{C.12})$$

Further partial integration yields

$$\int_{\theta_w}^{\frac{\pi}{2}} \cot^2(\theta) \Delta \theta d\theta = - \int_{\theta_w}^{\frac{\pi}{2}} \Delta \theta d \cot(\theta) - E. \quad (\text{C.13})$$

with $E_m = \int_{\theta_w}^{\frac{\pi}{2}} \Delta \theta d\theta$. Solving the first integral on the right-hand side in (C.13) results in

$$- \int_{\theta_w}^{\frac{\pi}{2}} \Delta \theta d \cot(\theta) - E = \Delta \theta_w \cot(\theta_w) - (\mathbf{r}^2 - 1) F_m - 2E_m. \quad (\text{C.14})$$

where F_m is defined by

$$F_m = \int_{\theta_w}^{\frac{\pi}{2}} \frac{d\theta}{\Delta\theta} = F\left(\frac{1}{2}\pi, \mathbf{r}\right) - F(\theta, \mathbf{r}). \quad (\text{C.15})$$

In the same way we define

$$E_m = \int_{\theta_w}^{\frac{\pi}{2}} \Delta\theta d\theta = \int_0^{\frac{\pi}{2}} \Delta\theta d\theta - \int_0^{\theta_w} \Delta\theta d\theta = E\left(\frac{\pi}{2}, \mathbf{r}\right) - E(\theta_w, \mathbf{r}). \quad (\text{C.16})$$

with $E(\theta_w, \mathbf{r})$ the incomplete elliptic integral of the second kind and $E(\frac{\pi}{2}, \mathbf{r})$ the complete elliptic integral of the second kind.

Acknowledgments

I would like to express my gratitude to all people who helped me during these years in Delft. During this time I met a lot of people whom I may count amongst my personal friends. In advance, I apologize to everyone who is inappropriately not mentioned in this list of acknowledgments.

First of all, I would like to thank David Smeulders, my promotor, without whom this project would not have been possible. David's useful advice in many aspects of this PhD, his positive attitude towards my PhD project and his detailed analysis of the physics, made this thesis to the form it is right now. I really appreciate that he found time for this project despite his very busy schedule. I am also thankful to my co-promotor Evert Slob for his advice, which showed me the right direction and made me work as efficiently as possible. And last but not least I thank all the members of the promotion-committee for helping me improve this text: C.P.A. Wapenaar, H. Steeb, J. Bruining, C.P.J.W. van Kruijsdijk and R. Sprik.

In the past few years that I worked at this department, I came in contact with many staff members, who supported me in a variety of ways. In particular I need to mention Hans Bruining for his useful advice regarding the experiments in general and electrokinetic phenomena in particular. For all the passionate discussions about physics, chemistry and many other subjects, which were fruitful and fun to do and his encouragements at times the research didn't go forward as planned. I thank Susanne Rudolph, Timo Heimovaara and Karl-Heinz Wolf for the many talks we had. Also the seismology courses, in which I had to assist Guy Drijkoningen come to mind. This work was not only highly interesting and it broadened my horizon from petrophysics towards geophysics, but it was also a lot of fun and something completely different during the early years of the PhD project. Finally I really need to mention Ranajit Ghose who gave me invaluable advice and with whom I worked together on his research about shear wave dispersion.

I am very grateful to my M.Sc supervisor Jan-Willem van Staveren, who inspired me to do a PhD in general and perform thorough research. I would

like to mention my teacher mechanical engineering Ernst Kouwe who sparked my interest in many Newtonian physics problems. This work benefits from my professor structural engineering. Arbocz's accuracy, his strictness, his inspiring pep-talks and the never ending quest for higher quality. Also I would like to mention my professor simulation and control engineering Bob Mulder. Last but not least I am thankful for the lessons I had from my math teacher at high school J. Vermeer. Without his way of teaching and his incredible patience to explain many mathematical problems, I probably never would have dared to choose a technical direction.

The experimental part of this thesis required the professional assistance and support of the technicians at the Geotechnology Laboratory. In particular I would like to mention Karel Heller without whom the experiments would have consumed much more time and would most likely have been performed less efficiently. An important lesson I learned, is that its better to use a fully developed set-up than an improvised set-up.

During my PhD I had the enriching opportunity to work with students who contributed to this work: Sjoerd de Ridder, Ruben Thomassen and Jose Hammer. Due to their background in geosciences, I could obtain much quicker insight in the geoscientific area embedding my subject. From the geoengeering group I especially want to thank Jelke Dijkstra and Wout Broere for the many liters of coffee that we converted into ideas and for helping me out with a wide variety of computer problems and all the other subjects we discussed in the lab and at the office. From the ISAPP group I would like to thank Mariya for all the discussions we had during lunch time and her colleagues Gosia and Wiktorja.

I had the enriching opportunity to work within a large group of colleagues and fellow PhD's. In particular I need to mention Karel van Dalen for all the Maple advice, Bouko, Menne and Patrick as my closest colleagues within the petrophysics group and all the other students from the geophysics, petroleum, geo-engineering and geology group; Bert-Rik, Bobby, Carlos, Chris, Danijela, Daria, Dessislava, Deyan, Dennis, Ellen, Elisa, Elmer, Etienne, Eva, Geert, Gerben, Gerrit, Hamid, Hein, Jerney, Jeroen, Jolanda, Joost, Jürg, Koen, Mario, Marit, Maria, Martijn, Marwan, Mattia, Mohsen, Nihed, Orion, Saikat, Talal, Thomas, Tristan, Veronica, Willem-Jan, Yufei. I want to thank you for the friendly working atmosphere, the distractions you organised and the fun we had during the DOGS drinks, EAGE conferences, 'Sinterklaas evening', the sailing trip, skiing and all the other things we did together.

I want to thank my colleagues from the faculty of aerospace, especially Nijso Beishuizen, Sjoerd Dietz, Herman Damveld, Thomas Lombearts, Wouter van der Wal and Anne-Marije Wijnans. They during their own research,

encountered similar problems as I did and shared this information, which helped speed-up my own project.

Last but not least I want to thank all the people I met during the conferences and workshops I visited. Especially Amra, Burke, Rosemary, Steven and Tobias. I thank them also for broadening my horizon to other scientific areas and deepening my insight in electrokinetic phenomena.

It is without any reservation that I can say my study probably would have been very hard, maybe even impossible without my parents. Thanks for all the support, encouragements and understanding.

Ferdinand Christiaan Schoemaker

Delft, 2011.

Curriculum Vitae

Christiaan Schoemaker (Amsterdam, 15 March 1978), graduated from Athenium in 1996. He studied Aerospace Engineering at Delft University of Technology, the Netherlands, from 1996-2003. From November 2000 to March 2001 he performed an internship at the Dutch Aerospace Laboratory (NLR), as an aeroelastic research engineer at the fluid dynamics department. Thereafter he specialized in mathematical modelling and identification, at the control and simulation division. His MSc thesis was on mathematical modelling of the non-linear equations of motion of a flexible aircraft.

At the end of 2004 he commenced his PhD research at the faculty of Civil Engineering and Geosciences, of Delft University of Technology, resulting in this PhD thesis report. At the end of the PhD project he contributed to the Dutch national research programme on CO₂ capture, transport and storage (CATO-2) on a feasibility study for permanent seismic and EM monitoring. Currently he is a research scientist at the Delft University of Technology.